Memorial
University of Newfoundland

Ocean Engineering Research Centre
Faculty of Engineering and Applied Science

FLOW OF CRUSHED ICE: PHYSICAL AND MECHANICAL PROPERTIES AND BEHAVIOUR

VOLUME 2: ANALYSIS OF DATA

Prepared for:

Canadian Coast Guard
British Petroleum plc
Esso Resources Ltd.
Gulf Canada Resouces Ltd.
Minerals Management Service
Mobil Research and Development Corporation
National Research Council of Canada
Petro Canada

Prepared by:

David Finn — *Ocean Engineering Research Centre*
Ian Jordaan — *Faculty of Engineering and Applied Science*
Sanjay Singh — *Memorial University of Newfoundland*
St.John's, Newfoundland

and

Paul Spencer — *GEOTECHnical resources ltd.*
Calgary, Alberta

St. John's, Newfoundland December 1989

Acknowledgements

The authors wish to thank the following people for participating in discussions which contributed to the preparation of this report:

Ian Bayly	(TDC)
Phil Clark	(Petro Canada Resources)
Jim Clarke	(British Petroleum)
Ken Croasdale	(Esso Resouces Canada)
Bob Frederking	(NRC)
Harry Iyer	(Gulf Canada Resources)
Ibrahim Konuk	(COGLA)
Dan Masterson	(Sandwell Swan Wooster)
John McCallum	(Coast Guard Northern)
Michel Metge	(Canatac)
Anton Prodanovic	(Mobil Research and Development)
Charles Smith	(Minerals Management Service)
Rick Weiss	(Exxon Production Research)

Thanks are also extended to Mohammed Sayed (NRC) for his helpful comments, and for providing video tape of NRC's recent crushed ice extrusion tests.

Executive Summary

The present project was initiated as a result of the observation, in the field as well as the laboratory, that ice in compression crushes in a narrow layer adjacent to the structure, and that it extrudes as a powder. Associated with this process, significant ice-induced vibrations have been observed. This phenomenon is of great importance in design. In order to understand and analyze this process, it was considered essential to conduct experiments on the extrusion of crushed ice. This was the subject of the present project, and this report contains an analysis of the data presented previously in Volume 1.

In brief, a series of tests consisting of the extrusion of a pre-crushed mass between two rectangular (0.762m x 0.508m) platens were performed. The long edges of the extrusion space were blocked to force extrusion in two directions only, and the upper platen was instrumented to record variations in pressure along the extrusion channel. Test speed ranged from 2.5 mm/s to 160 mm/s and initial layer thickness was usually 100 mm. Five crushing tests were also performed on cylindrical billets of solid ice, with speeds ranging from 2 mm/s to 125 mm/s, plus one test in the same apparatus using a pre-crushed ice sample.

Generally, extrusion of crushed ice has been modelled using two different theoretical approaches. The Mohr-Coulomb theory has previously been developed for granular materials. Characteristically, the flow would be along wedge-shaped planes and the pressure distribution would be "pointed" with a peak at the center of the platen. This approach was found to provide a good model for the extrusion of crushed ice at lower pressures (less than about 7 MPa). Typical values of parameters in the model are cohesion, c, from 0.03 Mpa to 0.001 MPa; internal friction angle, ϕ, 31° to 39°; and wall friction angle, δ, 1.5° to 3.0°. The other theoretical approach is based on the assumption that the crushed (or damaged) ice in the layer adjacent to the structure flows as a viscous fluid. The associated pressure distribution is parabolic in character without the characteristic "point". It should also be noted that other theoretical approaches such as those based on elastic or plastic material behaviour will also give a similar flat pressure distribution,

provided that failure at the interface between the platen and the material is not governed by a Mohr-Coulomb relationship. This condition would be satisfied, for example, when failure was within the material, not at the interface.

An unexpected result was obtained in the tests in the development of fluctuations of load corresponding to a repeating failure process. This commenced at a central pressure of about 5 MPa to 10 MPa, depending on test speed. Associated with this process was a flattening of the pressure distribution and visual observation after the test showed a central zone where the ice had fused together. This was similar to such zones observed in field tests.

Fits of the general trends of the data, ignoring the fluctuations in load, using a viscous model yielded values of viscosity near 1.0 MPa-s at 2.5 mm/s to 0.0009 MPa-s at 160 mm/s. Since the fluctuations in load appear to correspond to the situation in the field to be modelled, it might be argued the individual rises in load should be modelled. It was found that the slopes (in MPa/mm) of the individual rises increased with rate, implying difficulty of extrusion increases with increasing speed. This effect may dictate the use of viscoelastic theory in the development of a model for crushed ice which sinters and then fails. Typical slopes in the tests were of the order of 5 MPa/mm to 10 MPa/mm at the center of the platen.

Contents

List of Figures

1 Introduction

For ice-structure interaction at low relative velocities creep mechanisms will dominate, dissipating the interaction energy through the movement of grain boundaries and dislocations within the ice crystal. At higher velocities discrete ice pieces may be broken from the parent ice mass in a number of ways, depending on the interaction geometry, velocity, and ice properties. When compressive stresses induce crushing failure, the broken ice pieces are often of the order of grain size or smaller. Observations of crushing events indicate that a crushed ice layer of varying degrees of thickness is always present between the structure and the intact ice. As the structure advances the ice particles are squeezed out from the contact area and the layer thins, until further crushing of the parent ice sheet regenerates the layer (see Figure 1). Upon initial contact, both ice and structure deflect and the forces experienced increase. At some critical point a section of the intact sheet immediately in front of the indentor will crush, causing the load on the structure to begin dropping. The elastic rebound of the structure and the ice induces rapid extrusion until the advance of the intact sheet begins to re-deflect the structure. Crushed ice remaining between the parent ice and the structure continues to be extruded during this reloading.

The cyclic nature of the crushing/extrusion process may be of significant consequence to a structure operating in an ice-filled environment. The forces exerted by the intact ice on the structure are always transmitted through a thin crushed ice layer. A large portion of the ice-structure interaction energy is consumed by the extrusion process, and it is essential to the accurate modelling of the entire interaction that the behaviour of this crushed layer be understood. Design for dynamic effects requires a knowledge of the rate of loading, the peak load and the frequency of the force-time cycle idealized in Figure 2.

The overall objective of this project is to obtain an explicit mathematical description of the flow properties of crushed ice. Proposed models for this flow include Mohr-Coulomb theory and viscous fluid (Newtonian or Bingham material) theory. If the material behaves as a granular Mohr-Coulomb material, the forces involved in the interaction will be rate independent. Rate

dependency is characteristic of viscous fluid behaviour, although a Bingham model also incorporates a rate-independent term. The initial phase of the project consisted of a series of crushed ice extrusion tests performed under conditions as near as possible to those experienced in the field. Crushing and extrusion pressures in the field often exceed 40-50 MPa. Interaction velocities ranged from 2.5 mm/s to 160 mm/s and mean extrusion pressures of up to 11.7 MPa were acheived, although many were lower. Consequently, those tests which developed the greatest mean pressures were of most interest. Peak local pressures up to 45 MPa (the limit of the pressure transducer in most cases) were recorded.

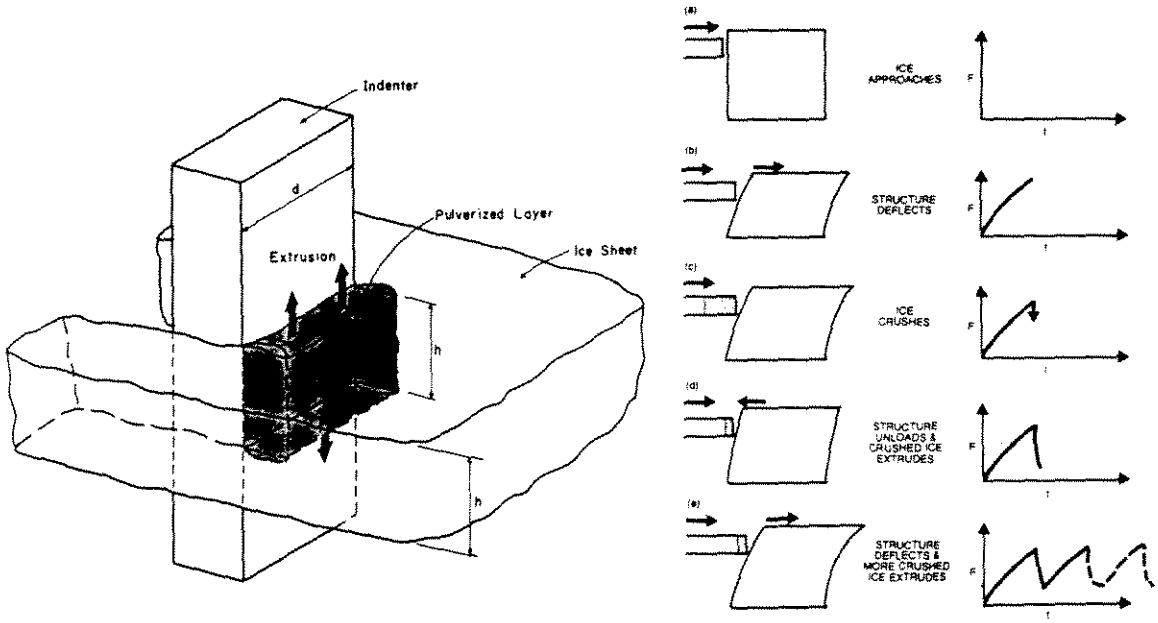

Figure 1: *Typical ice indentation scenario and idealized force-time series (Left: Jordaan and McKenna, 1988 Right: Jeffries and Wright, 1988)*

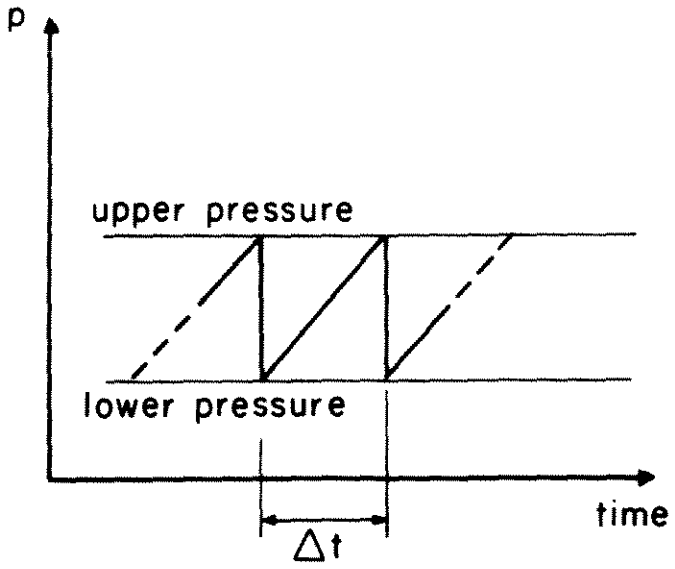

Figure 2: *Force-time data required to design for dynamic effects*

2 Frictional Processes in Ice

The flow of the crushed ice will be addressed in the next section: the analysis methods to be proposed are essentially based on continuum theories, in which the behaviour of individual particles is not considered. Rather, the process is "smeared out" or averaged, and corresponding properties such as cohesion, cofficient of friction, and viscosity need to be deduced from the experimental results. These properties are important when describing the constitutive behaviour of crushed ice with such models as Mohr-Coulomb and viscous flow theories.

It is useful at the onset to consider the frictional behaviour between two ice particles so as to develop some general ideas regarding the process on interaction between the ice particles moving relative to each other. Typical average exit velocities in the extrusion tests (at 125 mm/sec) were of the order of 1.5 m/sec. For the assumption of a viscous flow profile with laminar layer thickness of mean particle size as shown in Figure 3, the maximum particle-to-particle velocity could be as high as 0.3 m/sec. It is clear from the above that the problem under consideration concerns kinetic friction between ice particles. In general friction will depend on three factors (Tabor, 1981): the true area of contact, the nature of the interfacial bond formed and the way in which the material around the contacting region is sheared and ruptured during sliding. At very slow rates of sliding, adhesive forces can be quite large, producing a contact region which behaves as an intact part of the material. In this case the failure may occur almost at the shear

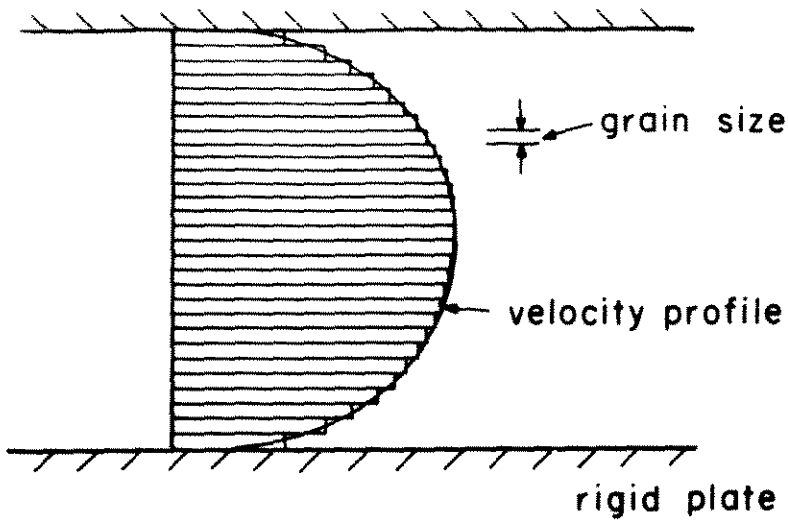

Figure 3: *Velocity distribution for Newtonian flow*

strength of the material. At high interaction speeds melting may occur at the interface, and sliding will take place simply by shearing the water film. In this case the material further away from the contact surface hardly plays any role.

The large normal pressures found in a crushed ice layer will modify this behaviour by squeezing out the water film and creating direct contact between the two surfaces. This is a mixed state of lubrication where shearing of the water film as well as the shearing mechanisms, especially crushing, generated by the direct contact may prevail. When considering the present problem, the existence of high local pressures is significant: it is therefore important to consider local melting due to pressure and heat generated from friction.

2.1 Friction and Frictional Melting

In most sliding situations the contact is made not over the whole of the apparent area of contact, but over a few isolated junctions. Since this true area of contact is small, it receives a substantial amount of thermal energy and its temperature may be much higher than the neighbouring regions.

An analysis of ice friction was carried out by Evans et al (1976). An equation describing the friction of skates sliding on an ice drum was derived. The total heat produced per unit displacement at each contact was taken as the sum of the heat conducted through the skates, the heat diffused in the ice and the heat required to cause melting at the surface. Oksanen (1983) concentrated more on the melt water film caused by friction and derived an equation based on the work of Evans et al. A plain couette flow of a fluid with

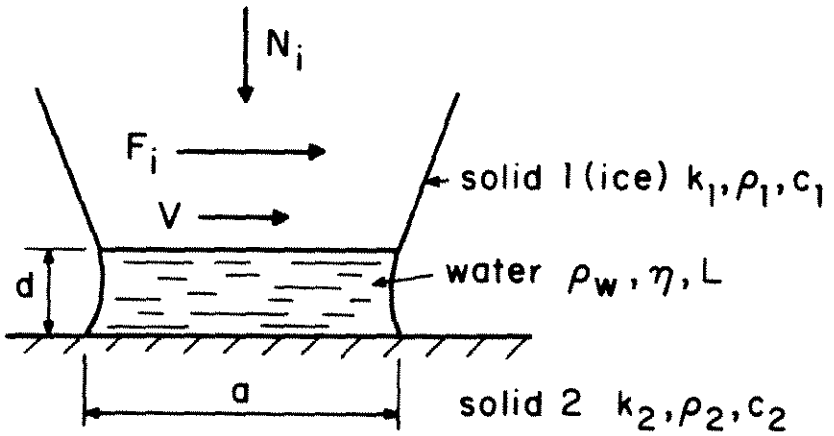

Figure 4: *Contact Model*

Newtonian viscosity η was assumed as a model for the lubricated interface. A contact model is presented in Figure 4. The friction F_i is

$$F_i = \eta \frac{v}{d} a = \mu N_i \tag{1}$$

where a is the contact area, v sliding speed, d the water film thickness and N_i the normal force. Film thickness was estimated on the basis of the energy available for melting ice at the interface. If n such contacts in an area is

subjected to the nornal load N, the coefficient of friction can be obtained as (Oksanen, 1983)

$$\mu = n^{-3/4} H^{-3/4} N^{-1/4} [\frac{1}{2}\sqrt{\frac{1}{2v}}(\Delta T_1\sqrt{k_1\rho_1 c_1} + \Delta T_2\sqrt{k_2\rho_2 c_2}) + \sqrt{\frac{1}{8v}(\Delta T_1\sqrt{k_1\rho_1 c_1} + \Delta T_2\sqrt{k_2\rho_2 c_2})^2 + \eta v L\rho_w}] \quad (2)$$

where H is the hardness of the softer material, ΔT the temperture difference between the contact surface and the ambient temperature, k the thermal conductivity, ρ the mass density, c the heat capacity of materials in contact. The subscripts refer to the material number (1=ice, 2=surface material). Further, ρ_w is the density of the water film and L the latent heat of melting of ice (see Figure 4).

When the temperature difference ΔT is large, i.e. at low temperatures, thermal conduction dominates over melting and the coefficient of friction is proportional to $1/\sqrt{v}$, while at temperatures close to 0°C it is proportional to $\sqrt{v}$. Oksanen's experimental results for ice friction on ice and the last equation is presented in Figure 4. This figure shows that the temperature and other factors may play a strong role in the rate dependent frictional behaviour of the material as a whole. Thus despite a viscous relation for the interface region, macroscopic behaviour is not exclusively rate dependent.

It should be noted that Oksanen's study was conducted at a very low normal contact stress of 0.001 MPa, which is several orders less than this study. As the material properties will change at large pressures, the frictional phenomenon could be entirely different from that predicted by Oksanen (Singh, 1989).

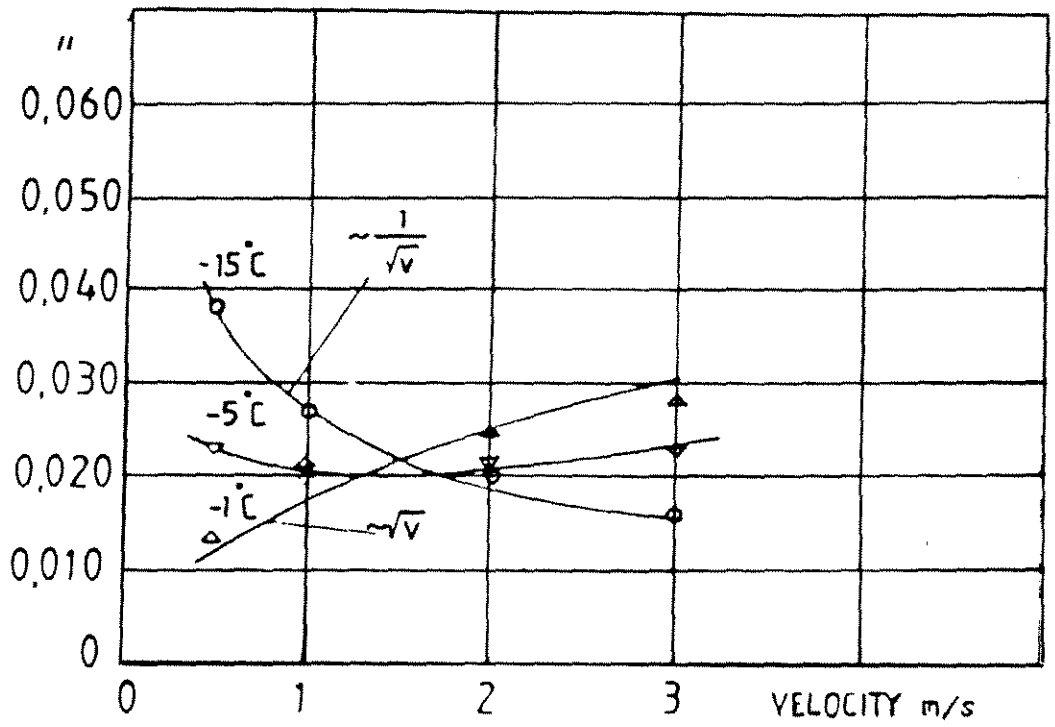

Figure 5: *Ice friction on ice as a function of velocity at different temperatures (Oksanen, 1983).*

2.2 Pressure Melting

An increase in contact pressure causes a depression of the melting point. When both ice and water phases are present, the Clausius-Clapeyron equation provides the temperature-pressure gradient $dT/dp = -0.074^{o}$ C/MPa at 0°C. At temperatures above or below 0°C this gradient decreases. A comprehensive study of pressure melting theories and exprimental observations is presented by Nordell (1989).

In the present test series the maximum pressure observed at a load cell of area 2cm^2 was about 45 MPa. A typical grain size after a test was of the order of 1mm. As the actual contact area could be a few orders less than the apparent contact area, inter-particle pressure will be the same order higher than the measured pressure. If an actual mean contact pressure is assumed to be 300 MPa, the melting point will be lowered by as much as 20°C, large enough to cause melting of ice at the test temperature of -10°C.

There was evidence of sintering at the high pressure central region of the platen, suggesting melting took place. The above mechanism is plausible in this regard. The extent of melting will affect the behaviour of overall constitutive modelling of the material.

3 Theoretical Approaches

3.1 Mohr-Coulomb Theory

Crushed ice is a granular material. As the constitutive relations for other granular geomaterials are well represented by the Mohr-Coulomb failure criterion, it has been proposed as a model for the crushed ice material (Hallam and Pickering, 1988; Flow of Crushed Ice-Volume 1, 1989). The Mohr-Coulomb criterion is shown in Figure 6. Generally it is interpreted as a yield criterion and combined with plasticity theory. This theory was originally conceived as a failure rule based only on statics, and as such is not a flow rule. Kinematics have been added in later formulations (Spencer, 1964).

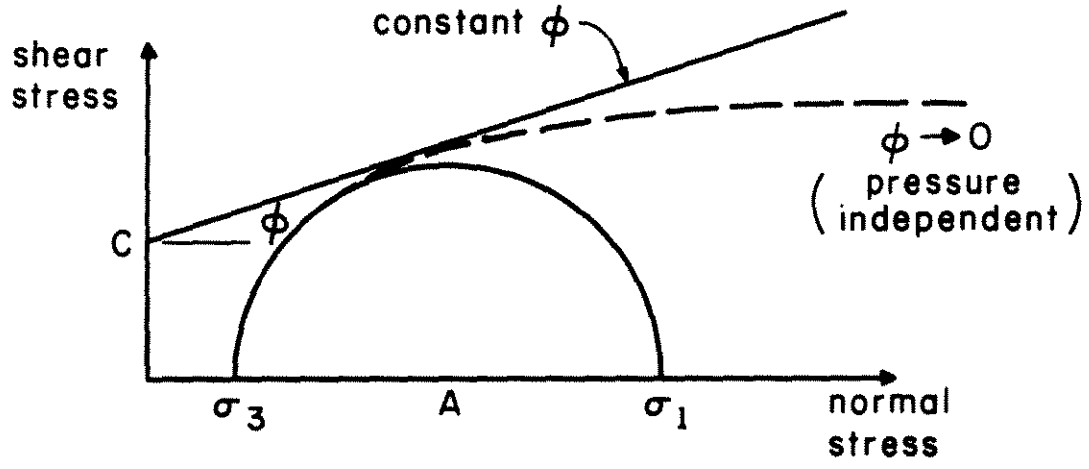

Figure 6: *Coulomb's criterion in a Mohr circle diagram*

Consider an element of material of size dx by h as shown in Figure 7, acted on by stresses τ, pressure p, σ_3 and $\sigma_3 + d\sigma_3$. The stress τ is a result of the friction between the element and the structure surface,

$$\tau = \mu p \tag{3}$$

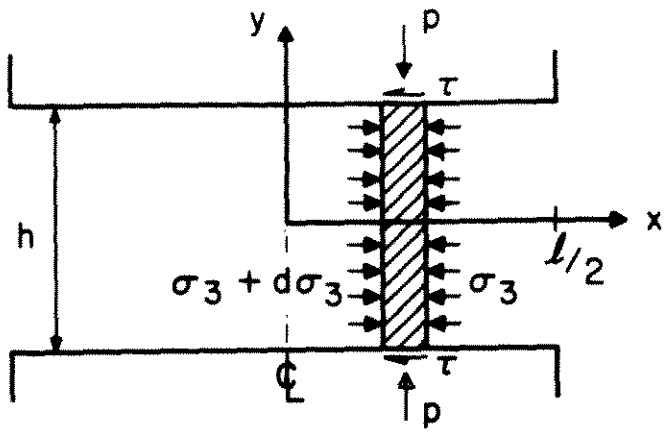

Figure 7: *Element of crushed ice material: Mohr-Coulomb*

Balancing forces in the x-direction and substituting μp for τ , one obtains

$$hd\sigma_3 = 2\mu p dx \tag{4}$$

The Mohr-Coulomb failure criterion in terms of the maximum principle stress p and the minimum principle stress σ_3 is

$$p = C + k\sigma_3 \tag{5}$$

where

$$C = 2c\frac{cos\phi}{1 - sin\phi}$$

$$k = \frac{(1 + sin\phi)}{(1 - sin\phi)}$$

p is the pressure on the structure at x, and ϕ the internal friction angle. The *cohesion, C*, represents the strength of the bond between particles which must be overcome before flow begins. The *internal friction angle*, ϕ represents the resistance to sliding once motion has been initiated. The coefficient k is analagous to the "passive earth pressure coefficient" commonly used in soil mechanics. Differentiation with respect to x yields

$$\frac{dp}{dx} = \frac{dC}{dx} + k\frac{d\sigma_3}{dx} \tag{6}$$

Cancelling the dx's, substituting into Equation 4 and rearranging gives

$$\frac{1}{p}dp = \frac{2\mu k}{h}dx \tag{7}$$

Integration of both sides yields

$$lnp = \frac{2\mu k}{h}x + C_1 \tag{8}$$

From Equation 5 it can be found that at $x=l/2$, $\sigma_3=0$ and $p=C$. Substituting this into Equation 8 gives

$$lnC = \frac{2\mu k}{h}\frac{l}{2} + C_1 \tag{9}$$

Subtracting Equation 9 from Equation 8 provides the solution

$$\frac{p}{C} = exp\left[\frac{2\mu k}{h}\left(x - \frac{l}{2}\right)\right] \tag{10}$$

where $\mu=tan\delta$ the external friction coefficient between ice and structure and δ the external friction angle, h the layer thickness, and C is the cohesive strength of the crushed ice. The pressure predicted by Equation 10 is zero for a cohesionless material, which is practically impossible, indicating that a small cohesion must be included. Another limitation of this analysis is that it assumes the direction of principal stresses is the same as that for the no friction condition. Thus it is applicable only for small friction where the rotation of principal stresses is not very large. Further this analysis provides an approximate quasistatic solution. Consequently, its applicability is restricted only to limit analysis. For the problem under consideration the flow kinematics which define the development of the flow could also be important. Equation 10 predicts pressure on the structure increasing exponentially to a sharp peak at the center giving a "friction hill" effect to the extrusion channel. The normalized pressure distribution across the plate, in the x-direction is shown in Figure 8 for a few typical cases.

If the frictional forces are absent along the interface of the plate and the material, the direction of the principal stresses and slip lines are as shown in Figure 9a. As shown the slip lines approach the surface at 45° and the normal pressure is uniform everywhere. On the other hand friction at the interface

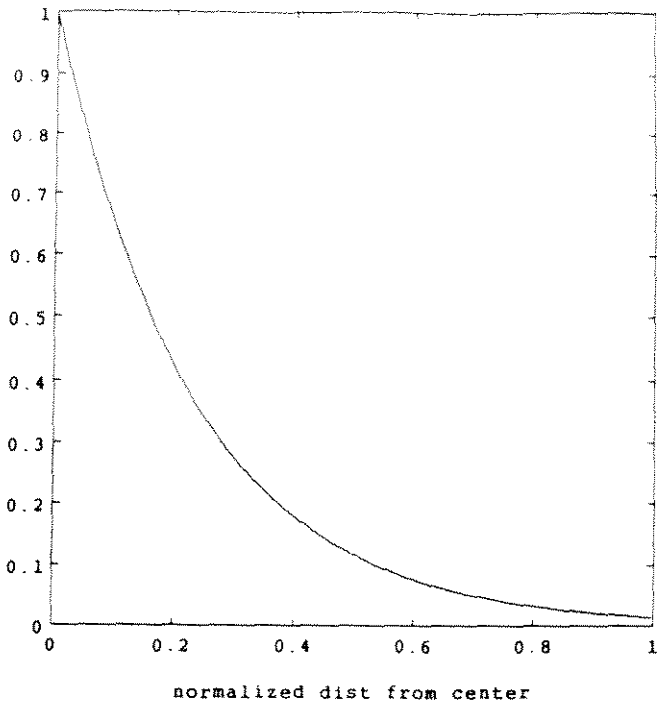

Figure 8: *Pressure distribution predicted by a Mohr-Coulomb Flow Theory*

distorts the slip-line field (Figure 9b) and rotation of principal stresses occurs. The limiting case occurs when the surface friction is larger than the shear strength of the material and slip occurs within the material itself rather than at the surface, with slip lines running parallel to the surface. No matter how large the normal stress σ becomes, the frictional stress τ cannot exceed the shear strength of the material τ_{max} itself. Thus Coulomb's equation $\tau = \mu\sigma$ is valid only until $\tau < \tau_{max}$. When σ exceeds τ_{max}/μ, the frictional stress is contant at the value τ_{max} (Cottrell, 1964). This process will cause re-distribution of stress.

An important feature of the Mohr-Coulomb yield criterion is its pressure-dependence, i.e. larger and larger shearing stress is required to initiate failure as the pressure is increased (pressure can be interpreted as the centre A of the Mohr circle of Figure 6 for the plain strain case). Inspection of equation 4 shows that the "friction-hill" of Figure 8 is associated with this pressure dependence. Any change in the pressure dependence will have an effect on the sharpness of the "friction-hill"; for the pressure independent case the central spike will be transfomed into a flat pressure distribution.

Figure 10 shows the Mohr-Coulomb failure criterion in stress space; it is essentially a hexagonal pyramid. Sketched on Figure 6 is a transition

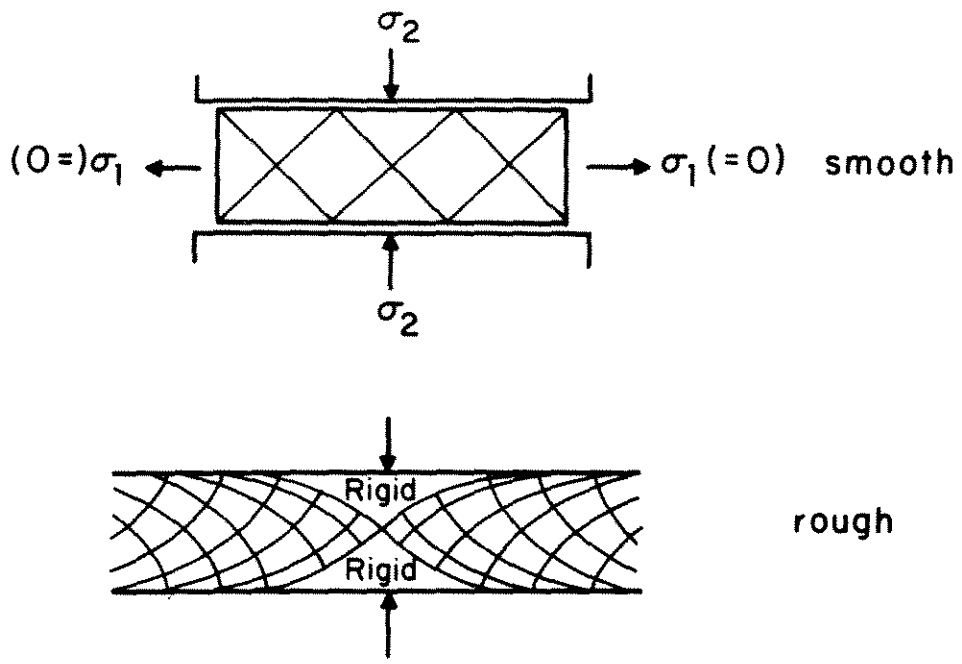

Figure 9: *Slip lines between smooth and rough plates (Cottrell, 1964).*

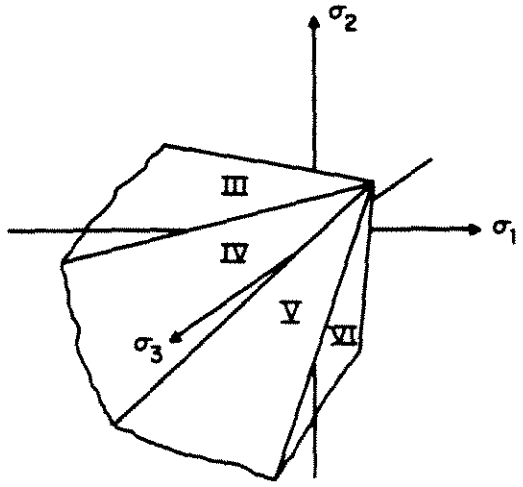

Figure 10: *Failure surface for Mohr-Coulomb criterion (Paul, 1968).*

to a pressure-independent criterion, i.e. ϕ decreasing with pressure. The Mohr-Coulomb failure surface becomes a hexagonal prism under these circumstances, i.e. the vertex of Figure 10 is infinitely far from the origin. This is in fact Tresca's yield criterion corresponding to maximum shear stress, irrespective of the hydrostatic pressure. Figure 11 shows two failure lines in the deviatoric plane for two values of ϕ. Cottrell (1964) shows that, even in

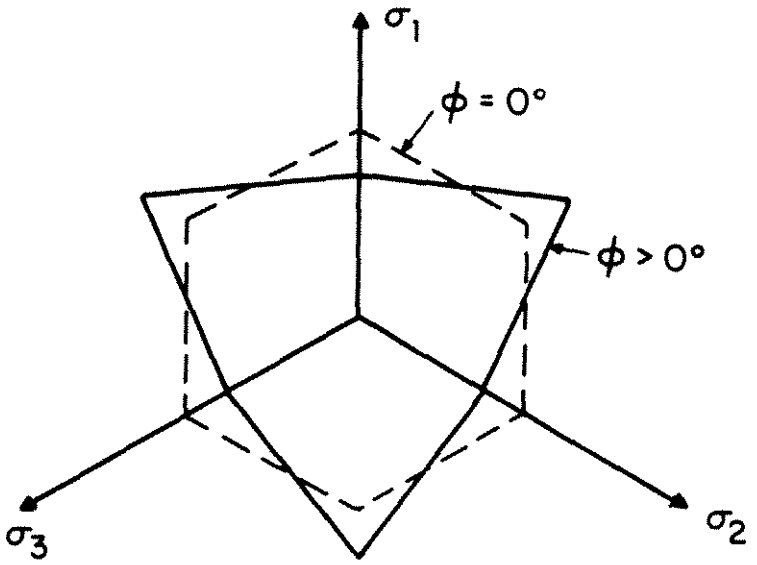

Figure 11: *Mohr-Coulomb failure criterion in the deviatoric plane*

the case of a pressure-independent plastic material, a "friction hill" develops if a frictional failure criterion governs at the contact surface between the platen and the material of interest.

3.2 Viscous Fluid Theory

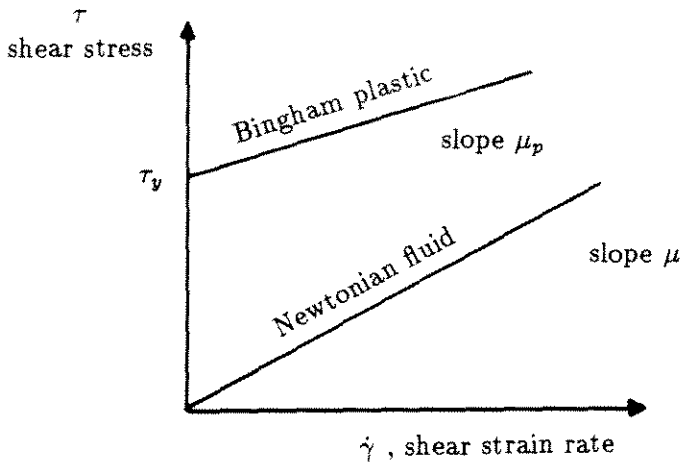

Figure 12: *Shear stress as a function of strain rate for Newtonian and Bingham materials*

It has been proposed that the crushed ice layer be modelled as a viscous material. The work of Kurdyumov and Kheisin (1976) indicates that the crushed material may possess plastic as well as viscous properties, warranting the use of a viscoplastic model. A perfect Newtonian fluid and a Bingham plastic have been considered for this analysis. For a viscous model, the pressure exerted on the structure is dependent on the rate of interaction. Consider a unit depth element of an incompressible, homogeneous Newtonian fluid dx by $2y$ moving in the x-direction due to a pressure gradient $-dp/dx$. Its motion is resisted by a shear stress τ along each face dx. Balancing forces in the x-direction

$$2\tau(dx) = dp(2y) \tag{11}$$

Introducing the Newtonian fluid model for shear stress in a fluid

$$\tau = -\mu\frac{dv}{dy} \tag{12}$$

substituting the r.h.s. for τ in Equation 11, and rearranging gives

$$\frac{dv}{dy} = -\frac{1}{\mu}\frac{dp}{dx}y \tag{13}$$

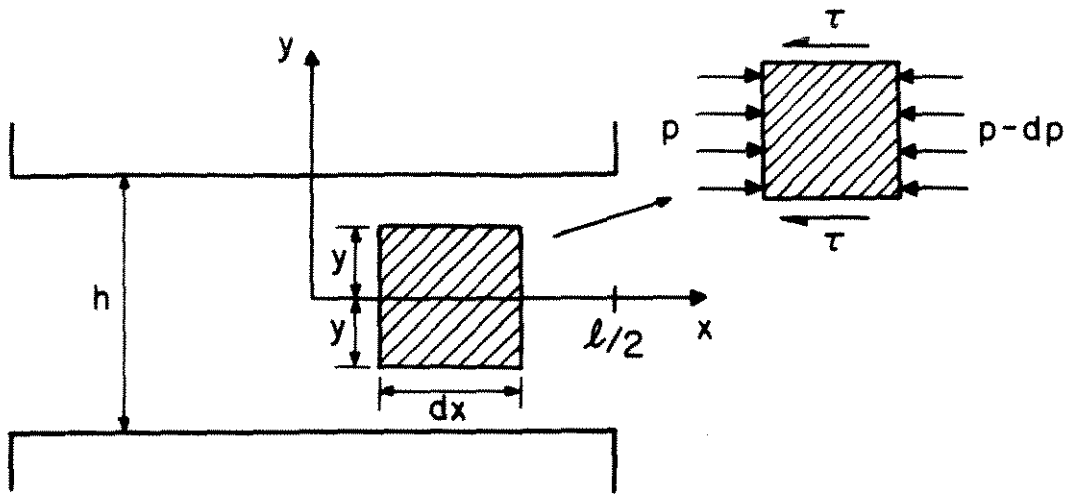

Figure 13: *Forces acting on an element of Newtonian fluid*

Integrating both sides, one obtains

$$v_{max} - v = -\frac{1}{\mu}\frac{dp}{dx}\frac{y^2}{2} \tag{14}$$

where v_{max} occurs at half the layer thickness, i.e. where y=0. Applying the boundary condition v=0 at the top and bottom platens, i.e. at $y = h/2$, it can be found that

$$v_{max} = -\frac{1}{\mu}\frac{dp}{dx}\left[\frac{h^2}{8}\right] \tag{15}$$

From this

$$v = -\frac{1}{\mu}\frac{dp}{dx}\left[\frac{h^2}{8} - \frac{y^2}{2}\right] \tag{16}$$

Assuming a parabolic velocity profile through the thickness of the layer, it can finally be found that

$$p = \frac{6u\mu}{h^3}\left[\frac{l^2}{4} - x^2\right] \tag{17}$$

where p is the pressure on the structure at x, μ the viscosity of the crushed ice layer, u the structure speed, h the layer thickness, and l is the total length of the extrusion channel. A complete derivation of this solution was presented by Jordaan and Timco (1988).

The Newtonian fluid model predicts a pressure distribution which flattens out as it approaches the center of the extrusion channel, rather than peaking

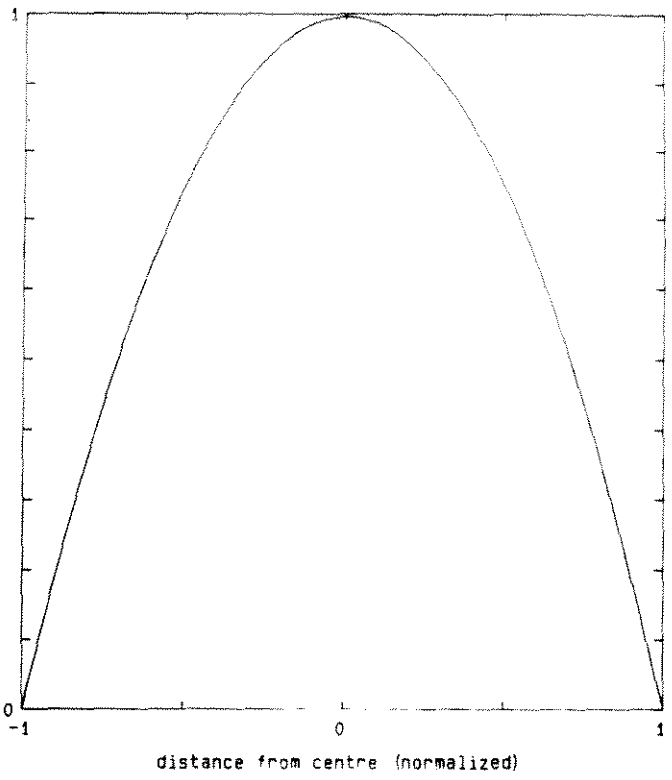

Figure 14: *Pressure distribution predicted by Newtonian model*

as described by the Mohr-Coulomb approach. The velocity profile of the extruding material will assume a parabolic shape.

A second viscous model which has been considered is that of a Bingham material. The total resistance to motion is composed of a Newtonian rate-dependent term and a rate-independent term τ_y:

$$\tau = -\tau_y - \mu \frac{dv}{dy} \tag{18}$$

This shear stress τ_y is a material property equivalent to the cohesion term of the Mohr-Coulomb model which must be overcome before flow will commence. This introduces an extra term in the equation describing flow, such that

$$p = \frac{6u\mu}{h^3}\left[\frac{l^2}{4} - x^2\right] + \frac{6\tau_y}{h}\left[\frac{l}{2} - x\right] \tag{19}$$

where τ_y is the fluid shear strength.

A typical Bingham pressure distribution is shown in Figure 15. The plastic component of pressure is linear for a fully frictional boundary, i.e. when there is no fluid motion along the platen surfaces. This equation becomes

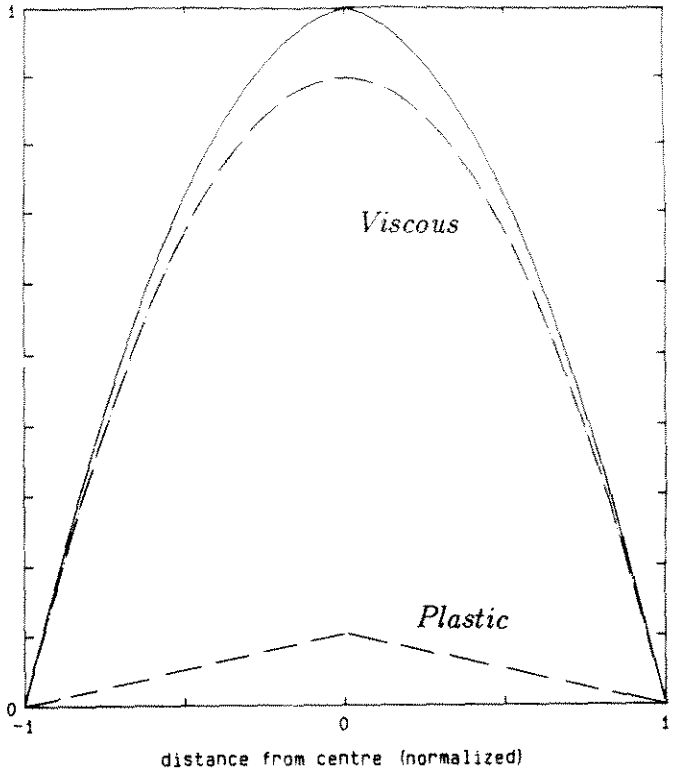

Figure 15: *Pressure distribution of viscous and plastic components of Bingham fluid*

dominated by the viscous term as the crushed layer thickness h becomes smaller.

3.3 Concluding Remarks

From the above discussion it can be concluded that

(1) Mohr-Coulomb materials develop a characteristic pointed pressure distribution with a "spike" at the center of the platen.

(2) This spike disappears when the constitutive equation becomes pressure-independent (elastic, plastic or viscous).

(3) Even in the case of pressure-independent yield criteria, a friction hill develops if failure along the platen-material interface is governed by a frictional relationship of the Mohr-Coulomb type. Conversely, this no longer applies if failure is within the material, not at the surface.

4 Analysis of Extrusion Tests

4.1 General Trends

The primary goals of this experimental series were to gain a better understanding of the processes involved in the extrusion of crushed ice, to determine the general properties of the crushed ice material governing its behaviour (such as bulk density, bulk viscosity, internal friction angle, external friction angle, and cohesion), and the development of flow rules accurately describing this behaviour. Mohr-Coulomb models and viscous fluid models have both been suggested as appropriate theories to describe crushed ice material. The initial step of data analysis was to determine how well these models compared with the acquired data.

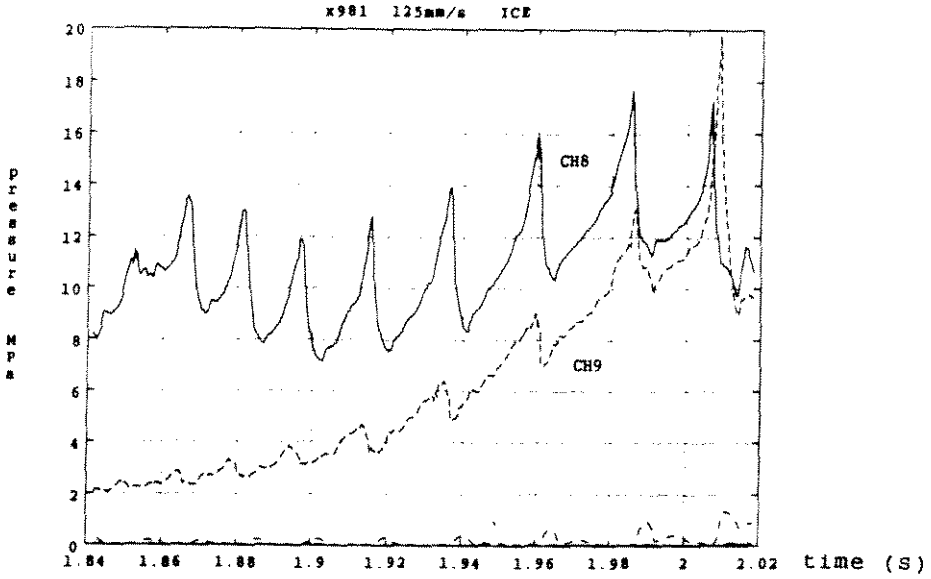

Figure 16: *Segment of time-series data with characteristic "sawtooth" pattern*

Initial examination of the pressure-time series revealed a regular "sawtooth" pattern developing near the end of most tests. Only the 2.5 mm/s extrusion tests failed to always develop this pattern. At some point the layer reaches a critical thickness at which pressure rapidly increases and the cyclic behaviour commences, particularly in the center half of the extrusion channel where the highest pressures develop. This critical thickness varied

from test to test but was always between 25 and 35 mm. The mean central platen pressure accompanying the emergence of the sawtooth pattern was found to be 11 MPa for high speed tests (125 mm/s) and 5 MPa for medium speed tests (25 mm/s). Test X996 (160 mm/s) did not develop the sawtooth pattern. The stage of extrusion prior to the emergence of this pattern will be referred to as "low pressure extrusion", and the stage during which the sawtooth pattern is evident "high pressure extrusion".

Some tests were performed with a thin layer of ice covering the lower platen surface. Similar results were obtained for 25 mm/s tests with and without the ice covering: the sawtooth pattern emerged at similar pressures and layer thicknesses. For the 125 mm/s tests, the ice-covered platen always resulted in the development of higher pressures with the emergence of the sawtooth pattern. For the bare steel platen covering, however, the pattern sometimes emerged at greater layer thicknesses, and pressures did not always increase significantly afterwards.

Observations at the National Research Council of Canada revealed the formation of regular wedge-shaped failure planes during extrusion (M. Sayed, NRCC, personal communication, 1989). These observations were made of tests at lower pressures than the present study. Study of flow visualization tests X967-X962 (Volume 1) did not show any clear pattern although wedges were seen in isolated cases. The highest centre pressures for these tests was 4.5 MPa for test X963, and the highest pressures for all other flow visualization tests were between 0.1 and 0.9 MPa, well below the value at which high-pressure extrusion characteristics such as the sawtooth pattern are dominant. The thinnest layer developed was 44 mm, corresponding as well to the low pressure stage of extrusion.

After the completion of each test, a solid, fused ice mass remained in the extrusion channel, indicating that water which re-froze once platen motion stopped was created during extrusion. The solid mass frequently extended $\pm$ 250 mm along the x-axis from the center of the platen, occasionally extending almost the entire length of the extrusion channel.

4.2 Pressure Distributions

The shape of the pressure distribution from the channel center to the exit of the extrusion channel is different for the Mohr-Coulomb and viscous fluid models. The Mohr-Coulomb model predicts an exponentially increasing pressure moving from the exit to a sharp peak at the platen center. Viscous theory predicts a pressure distribution which behaves in the opposite manner, flattening out as it approaches the center.

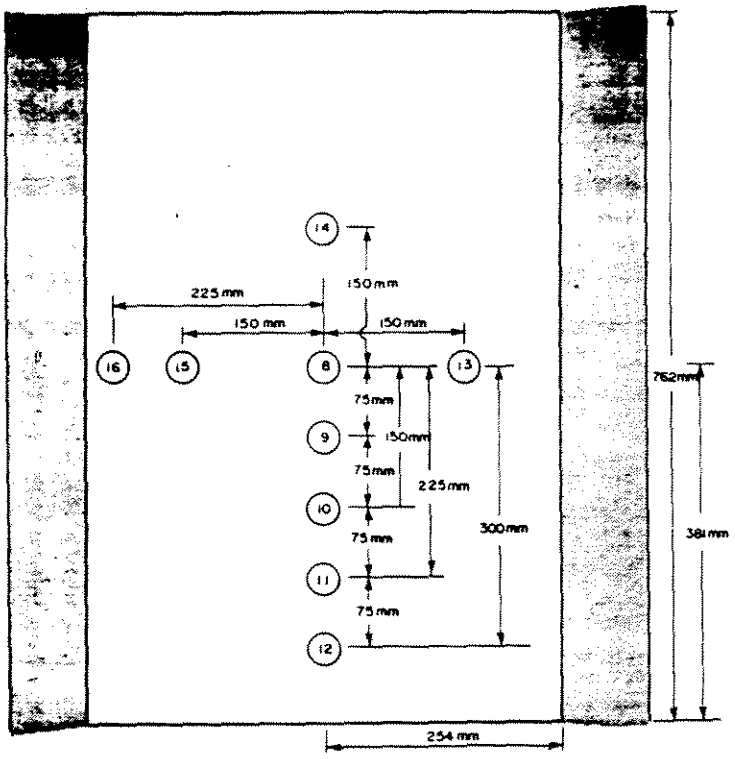

Figure 17: *Pressure transducer arrangement on test platen (Volume 1)*

A series of five pressure transducers were mounted at 75mm intervals from the platen center to a point near the extrusion channel exit. Load cell 8, load cell 13, load cell 15, and load cell 16 recorded the platen's centerline pressure history, and load cell 12 the platen's pressure history near the extrusion channel exit. Load cells 9 through 11 were positioned in between, as shown in Figure 17. The pressure recorded by load cell 16 was usually higher than

the three other centerline pressures, due to edge effects. The centre platen pressure was taken as the average of load cells 8, 13 and 15. By plotting this central pressure value and pressures from load cells 9 to 12 at the same point in time, an instantaneous pressure distribution can be found.

The shape of these distributions was found to change throughout the test. During the initial stage of extrusion described above, i.e. the low-pressure stage, the load was generally carried by a narrow central "zone of influence" of the platen, and the pressure distribution was ostensibly Mohr-Coulombic in nature, with a spike forming at the platen centre. Flow in this stage is probably granular in nature with little crushing or melting occurring. At the point of emergence of the distinctive "sawtooth" pattern the pressures recorded by transducers 8, 9 and 10 begin to rise dramatically, and the pressure distribution usually flattens out to a parabolic shape. The "zone of influence" generally widens, but is normally within a few millimeteres of the half-width of the platen. The high pressures and behaviour observed during this latter stage of extrusion make it of most interest to this study.

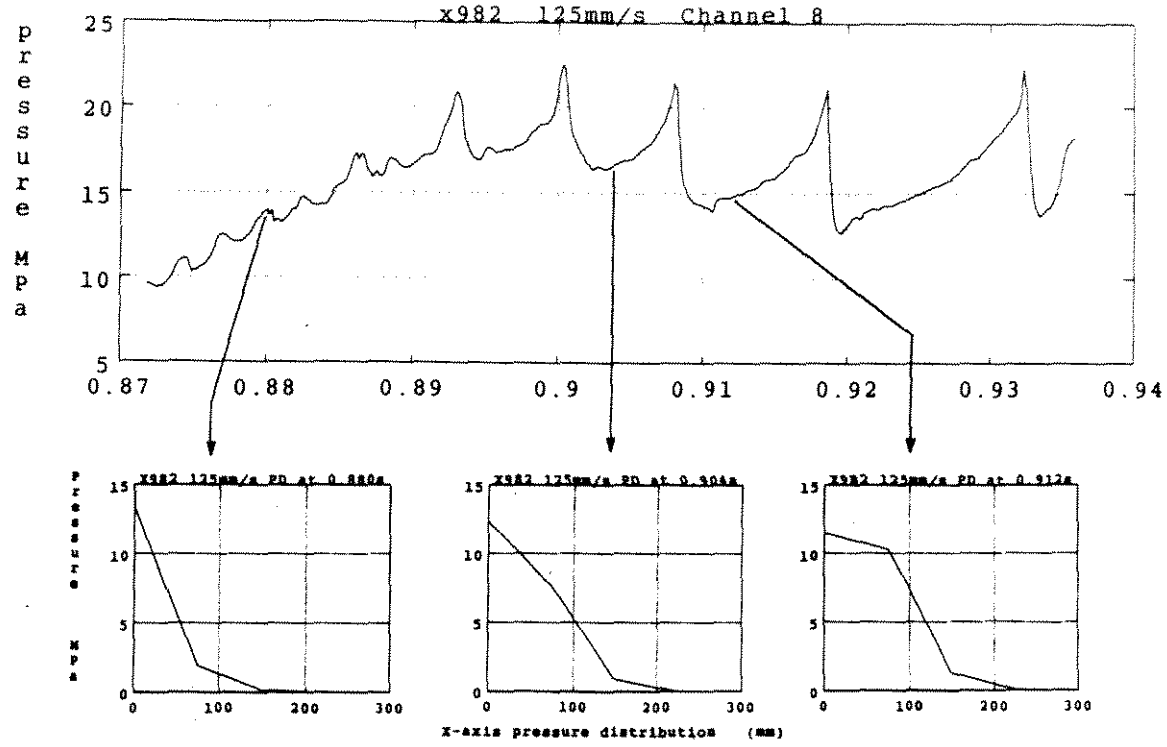

Figure 18: *Pressure distribution transforming from "friction hill" spike in low pressure stage of extrusion (left) to flatter parabolic shape in high-pressure stage of extrusion (right) during 125 mm/s test*

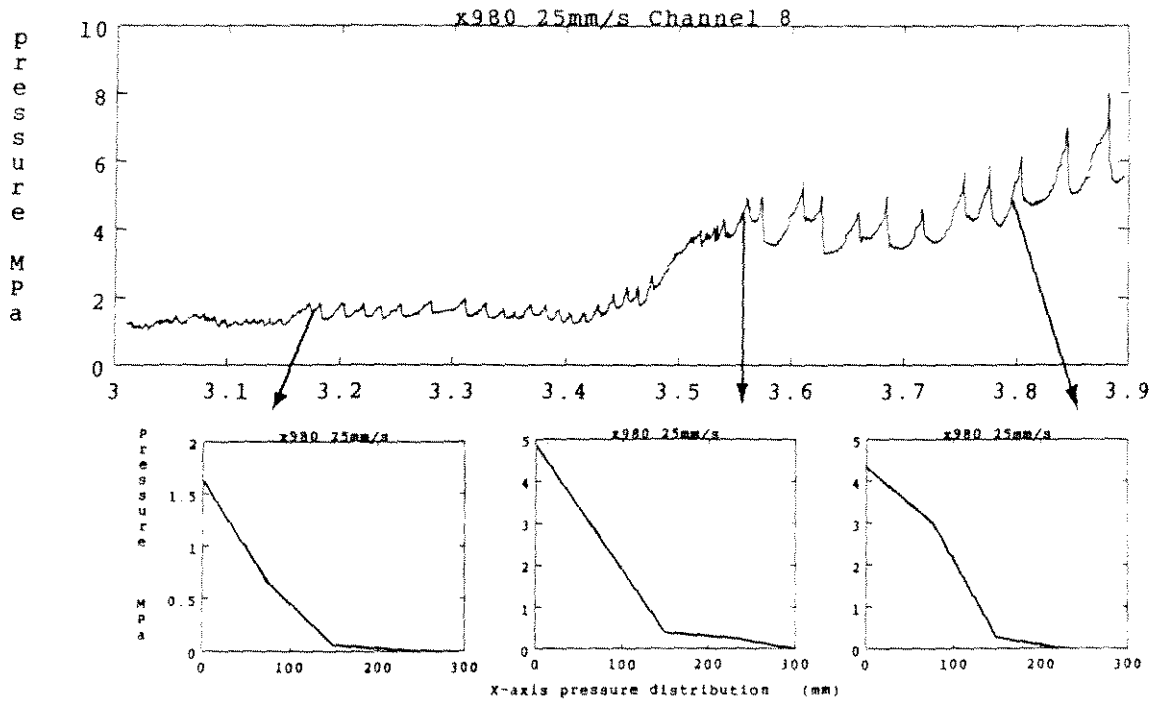

Figure 19: *Pressure distribution transforming from "friction hill" spike in low pressure stage of extrusion (left) to flatter parabolic shape in high-pressure stage of extrusion (right) during 25 mm/s test*

4.3 Pressure-Density Relationship and Mass Flow

As the two platens move closer together the crushed ice between is forced outwards through the extrusion channel or compacted into a denser crushed material.

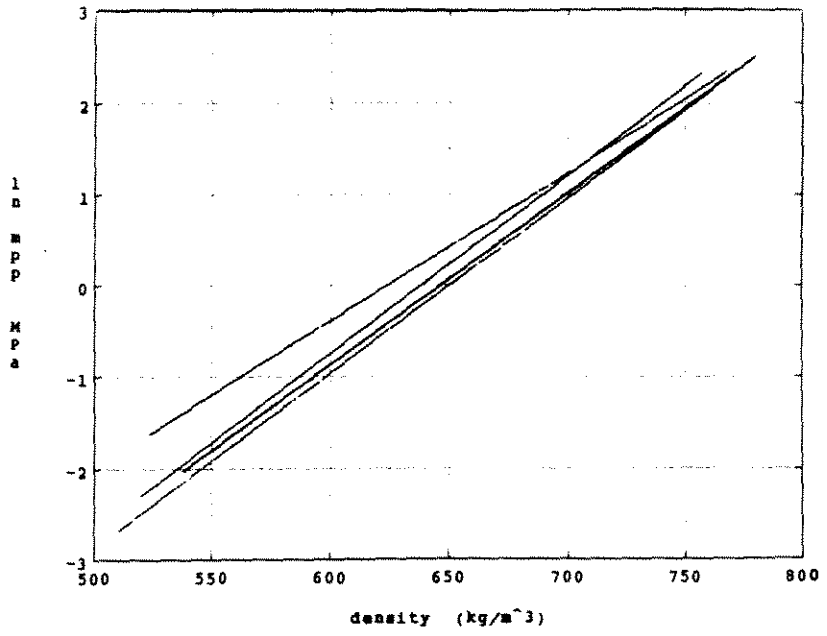

Figure 20: *Linear fit of ln(Mean Plate Pressure) as a function of density for compaction tests X977-974*

The four compaction tests, X977, X976, X975 and X974, were used to develop a pressure-density relationship for the crushed ice (Volume 1, 1989). These tests were performed with the ends of the extrusion channel blocked to prevent flow of ice from the test chamber. The tests were done at speeds of 125 mm/s, 25 mm/s and 5 mm/s to determine the effect, if any, of rate on compaction pressure. A plot of the natural log of Mean Plate Pressure as a function of density for the four tests is shown in Figure 20. The density of the crushed ice at each layer thickness was calculated for each test by

assuming constant mass within the extrusion chamber and using the final density and platen displacement data. A general function was developed to predict densities at known pressures:

$$\rho = \frac{ln(MPP) + 12.334}{0.0191} \tag{20}$$

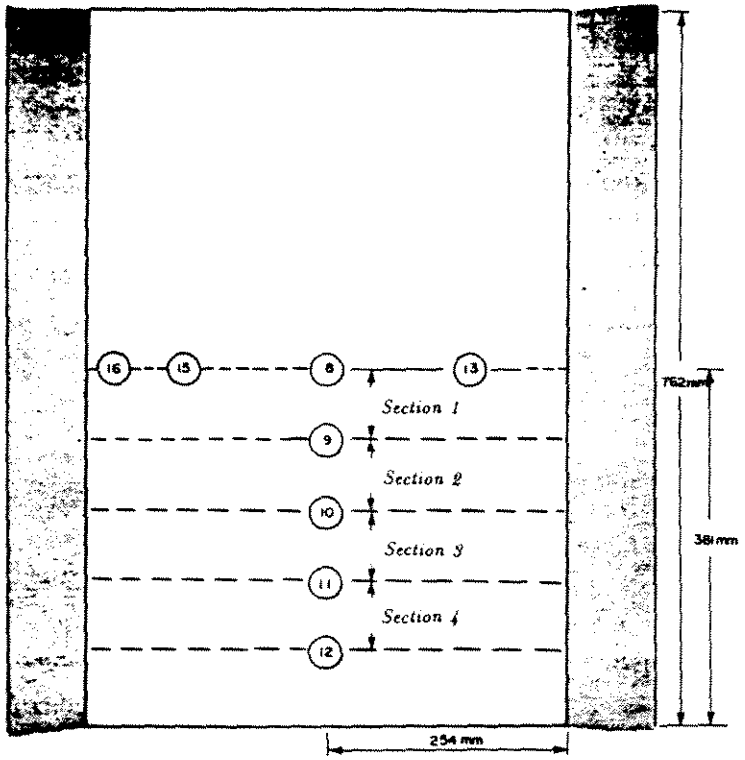

Figure 21: *Test platen divided into sections (Volume 1)*

Using this equation the density of the crushed ice at any pressure can be calculated for any time during a test. Equation 20 was used for loading and unloading, i.e. dilatation occurs on unloading. The extent of dilatation of the crushed material was assumed to be governed by Equation 20 as well, an initial working assumption which should be subject to further investigation.

The platen can be divided into four sections: section 1 between load cells 8 and 9, section 2 between load cells 9 and 10, section 3 between load cells 10 and 11, and section 4 between load cells 11 and 12 (see Figure 21). By

using the mean instantaneous pressure for a section and Equation 20 the mass of ice present in a particular section at that time can be determined. This method was used to calculate changes in ice mass throughout the test.

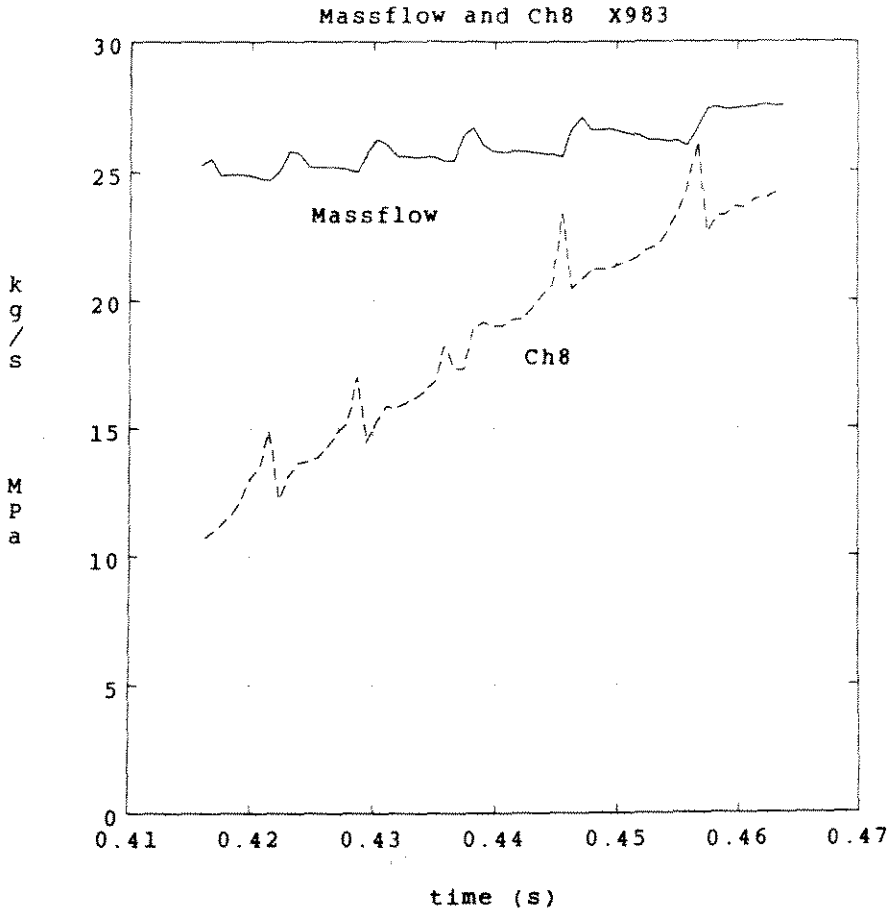

Figure 22: *Mass flow and pressure for test X983 (125 mm/s)*

Mass flow occured in a cyclic manner. Pressure drops in the central sections were followed by a brief increase in mass flow, as shown in Figure 22. This correlates with the theory of sintering and re-crushing of the granular material during extrusion. The re-crushing at a pressure peak precipitates a short burst of extrusion, as discussed previously.

The greatest increases in density were found in the central region. Mass flow from the two central sections tended to be steadier than that from the two outer sections. The extent of fluctuation in the total mass flow rate from peaks to steady flow was approximately 10 %.

4.4 Rate Dependence

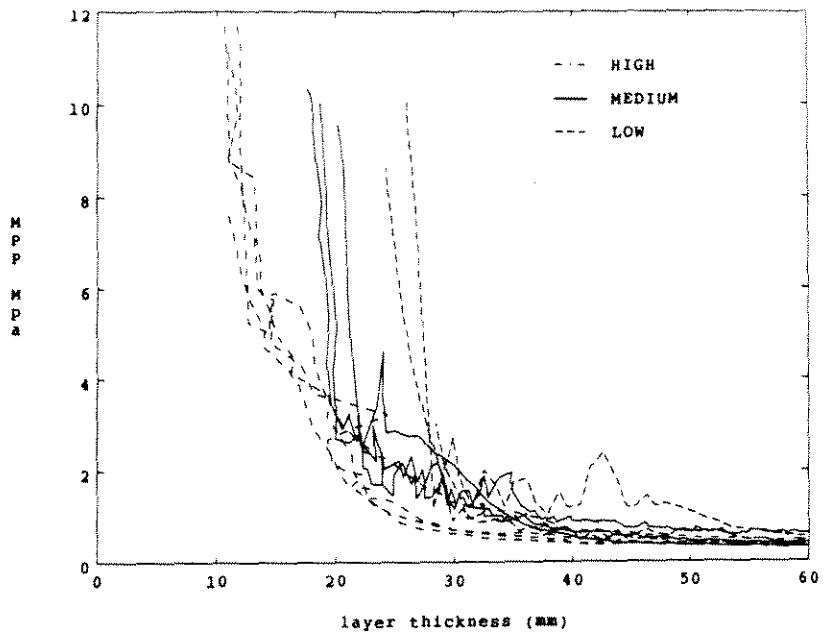

Figure 23: *Mean plate pressure vs. layer thickness for tests of high (125 mm/s), medium (25 mm/s) and low (2.5 and 5 mm/s) speeds*

A plot of the mean plate pressure as a function of layer thickness is presented in Figure 23. As the platen velocity increased a final lower thickness was acheived. The sudden increase in MPP occurs at a layer thickness between 25 and 30 mm for all tests with mean plate pressures higher than 3-4 MPa.

Spectral analysis was performed on all tests which exhibited cyclic behaviour. The analysis was performed on Channel 8 (centre) pressure over the latter region of extrusion, when the pressures were highest and the regular sawtooth pattern developed (see Figure 24). The frequency varied greatly from speed to speed. The mean frequency for high speed tests (125, 160 and 60 mm/s was 118 Hz. The mean frequency for medium speed tests (25 mm/s) was 17 Hz, and for low speed tests (2.5 and 5 mm/s) was 2 Hz. A plot of

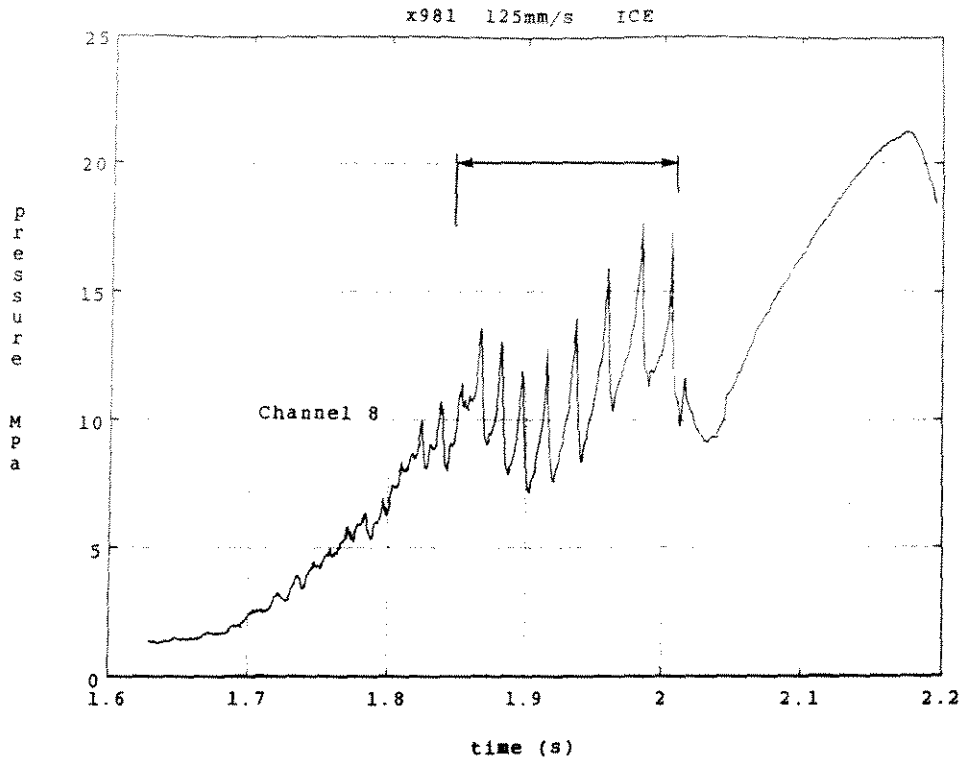

Figure 24: *Typical portion of pressure data used for spectral analysis*

the frequencies vs. mean exit velocities for the period of cyclic behaviour is shown in Figure 25.

The individual fluctuations in pressure during the high-pressure stage of extrusion were examined for rate dependence. The slope of each sawtooth usually increases until the peak is reached, indicating that within each cycle it steadily becomes more difficult for the platen to squeeze out the crushed ice. The slope of these individual sawteeth was approximated with a straight line, and calculated in terms of rise in MPa with change in layer thickness (MPa/mm) (see Figure 26). A plot of the mean slope for the 25 mm/s tests and the 125 mm/s tests reveals a rate-dependence for the individual fluctuations (see Figure 27).

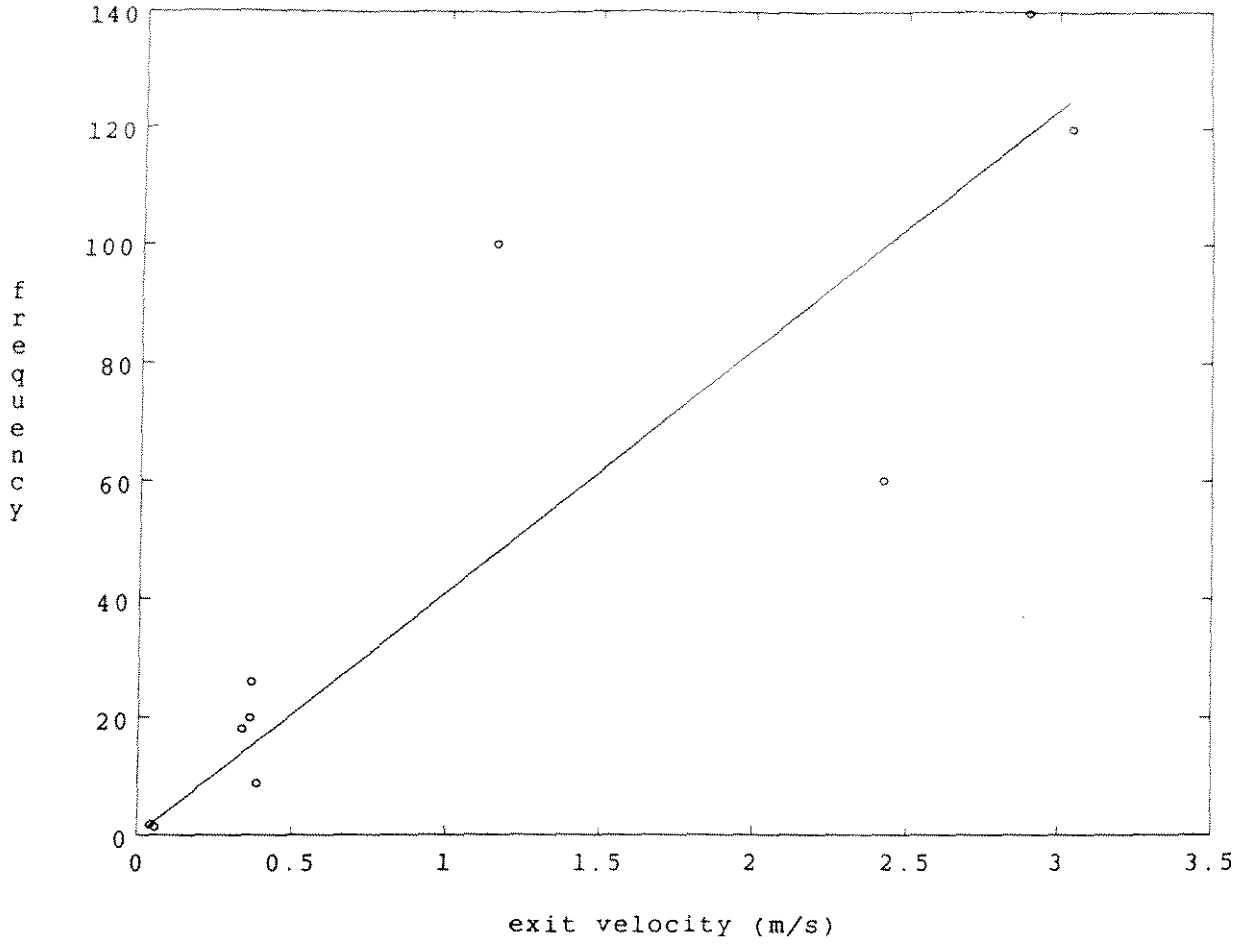

Figure 25: *Frequency of centre pressure oscillations vs. exit velocity*

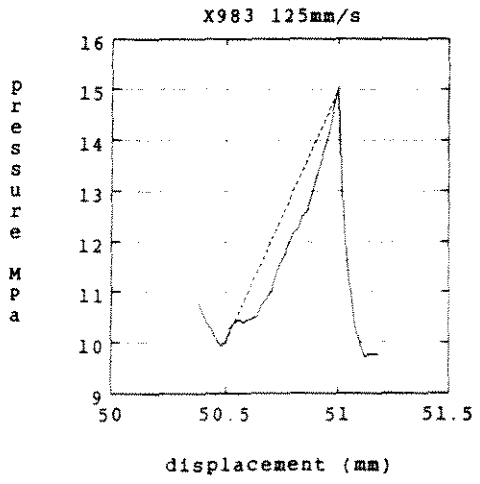

Figure 26: *Approximation of slope of a single sawtooth*

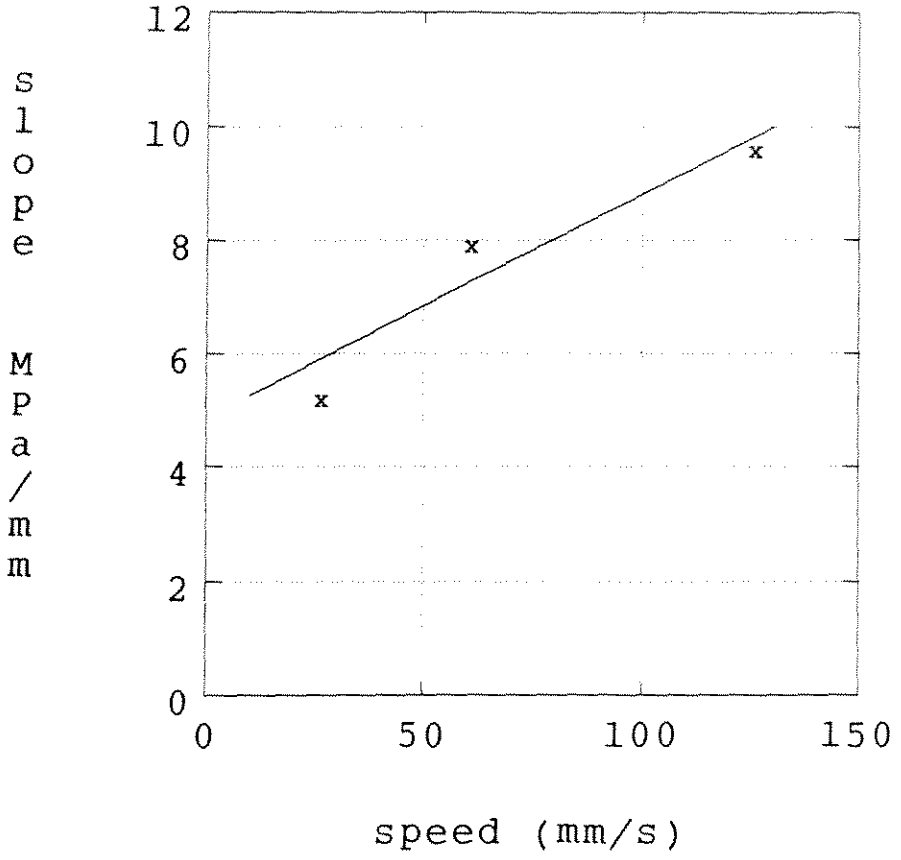

Figure 27: *Mean slope of individual sawteeth as a function of test speed*

4.5 Instrumentation Aspects

This section discusses some aspects of the instrumentation as it impacts on the collected data. The main questions are related to the dynamic response of the test frame and the control system. There have been comments that perhaps the cyclic nature of the interaction pressure during the high-pressure stage of extrusion is caused by some dynamic or resonant characteristic of the test system. Similar cyclic interactions have been observed in at least three field tests (Pond Inlet on iceberg ice, Rae Point on multi-year ice, Hobson's Choice on shelf ice), on offshore structures (Molikpak) and other larger scale laboratory tests (Gulf crushed-ice extrusion, drop ball tests). Thus the cyclic nature is one of fairly wide generality. All of these systems have their own set of dynamic characteristics and resonant modes over a fairly wide range of frequencies, and it is useful to look at the principal dynamic particulars of the current test frame.

In the strength testing of ice it is known that the stiffness of the test frame has an effect on the observed failure strength of the ice. This is mainly due to the energy stored in the test frame not being negligible relative to the energy stored in the test sample. In the design of the test system a stiff frame was an important design consideration. To this end a compact frame was designed, but after that stiffness in essence is dependent upon the amount of steel in the frame, and is in turn proportional to the cost of the frame. One can show that the following simple expression relates the energy stored in the frame compared with the energy stored in the sample:

$$\frac{W_f}{W_s} = \frac{AE}{kL} \tag{21}$$

where
W_f = Energy stored in the frame
W_s = Energy stored in the sample
A = Area of sample
E = Young's Modulus of sample
k = Stiffness of frame
L = Length of sample

From measurements provided in Appendix 1 of Volume 1 the stiffness of the frame was 7.14 GN/m and the area of the sample $0.387m^2$. The other variables, sample thickness and and modulus, vary during the test and representative values near the end of a test shall be used. Taking L to be

0.02 m and E to be 1.10 GPa gives the ratio of W_f/W_s a value of 2.71. In other words much more energy is stored in the frame than in the sample, and that in this application the frame is not "stiff". Note that this figure of merit gets worse as the ice pressure gets greater.

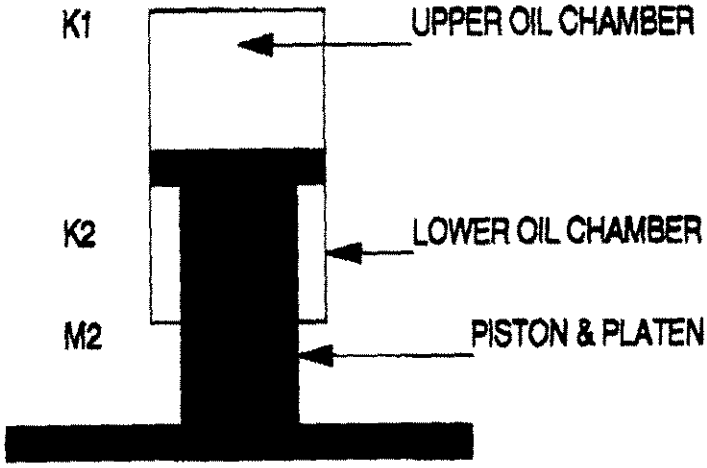

Figure 28: *Instrumented platen and actuator*

Apart from the steel of the test frame, another source of elasticity is the oil in the actuators. The situation is illustrated in Figure 28 in which there are oil chambers on each side of the piston. Each of these chambers can be treated as a spring. Assuming that the walls of the actuator are rigid then the following expression describes the stiffness of the oil spring:

$$k = \frac{k_s A_1}{l_1} + \frac{k_s A_2}{l_2} \tag{22}$$

where k = Overall stiffness
k_s = Oil bulk modulus
$A_{1,2}$ = Cross-sectional area of column 1 or 2
$l_{1,2}$ = length of column 1 or 2

Calculations based on the deflection of thick walled cylinders indicate that the assumption of rigid actuator walls is valid. The stiffness from this source is about 10 GPa. As can be seen from Equation 22, the oil column stiffness is a function of the position of the piston within the actuator and thus a function of the ice layer thickness. Putting in typical values of the parameters in Equation 22 gives a minimum stiffness of about 3 GN/m. Thus the oil column provides a stiffness less than the frame. The stiffness can be re-expressed in terms of displacement for a 1 MPa mean plate pressure change. For the oil system this translates to a 0.12 mm per MPa change. A change of this order in layer thickness is expected if the pressure due to the ice extrusion changes instantaneously. Note that the finite response time of the control system will not allow for the correction of this change.

The resonant frequency of the oil spring platen mass system can be estimated using:

$$f = \frac{1}{2\pi}\sqrt{\frac{k}{m}} \tag{23}$$

where f is the frequency and m the mass of the system. Using the mass of the piston and the instrumented upper platen as about 800 kg, the resonant frequency is found to be about 300 Hz. The vibration is not free because of the interaction with the ice sample. This will have the effect of introducing damping and increasing the effective mass of the vibrator.

The resonant frequency of the test frame can also be estimated using Equation 23. The mode of oscillation is assumed to be a vertical one in which the frame vibrates symmetrically about its centre plane. In that case the resonant frequency is estimated to be about 350 Hz. Inspection of the displacement records of, for example, test X979 indicate some vibrations at about 200 and 400 Hz. Inspection of the mean plate pressure record for the same test indicates a vibration at about 375 Hz. It seems reasonable to assume that these vibrations are associated with the motion of the instrumented platen on the spring of the oil actuator. Although these high frequencies were found, it should be noted that the dominant frequency for this test is considerably lower, about 32 Hz. As noted above, the stiffness of

that spring depends on the actual piston location within the actuator and can be easily be greater than indicated. This means that the mode frequency previously estimated is a lower limit.

The amplitude of the displacement excursion is up to 2-3 mm from the equilibrium location. The relatively large amplitude excursions can be understood by considering the vibrator as a forced single degree of freedom oscillator with damping. Detailed calculations of the response have not been performed but for a step input loading, the dynamic response can be up to twice the static response. If the loading has a sinusoidal component then the response can be amplified if the excitation frequency is close to the resonant frequency of the oscillator.

4.5.1 Displacement Control

The performance of the control system has an effect on the stability of the displacement profile. An analysis of the whole control system and the dynamic response of the test frame is a large task. Some of the elementary aspects will be discussed here.

The flow of oil into the actuator is controlled by a three stage servo-control valve physically mounted on the actuator. The control signal for the motion is a ramp voltage synchronized with the data acquisition. The feedback signal for the control system is the output of the displacement potentiometers mounted directly across the upper and lower platens. In this arrangement the stretch in the test frame and the oil column will not introduce an error for slow changes. For rapid changes the response time and the accuracy of the control system becomes important. The bandwidth of the control system depends on a number of factors, for example the oil supply pressure. For these tests the small amplitude bandwidth was about 50 Hz. If the perturbations are much faster than that then the servo cannot correct for them. An additional factor comes into play as the platen velocity approaches the "slew rate" of the actuator. This slew rate is the maximum velocity which the actuator will experience when the control valve is fully open. At the slew rate, while there is still a control system it is not providing any control. The slew rate was 160 mm/s for these tests. At the velocity of 125 mm/s the control system does not have much room to counteract the effect of perturbations. This can be understood by noting that if the perturbation requires a correction of more than the slew rate, obviously this cannot be

acheived and a displacement error will result. An additional factor is that at low platen velocity the control valve position is very close to the neutral position and small changes in its setting result in large changes in the relative oil flow. At larger velocities the valve position is further away from neutral, and to obtain the same relative change in oil flow requires a larger physical change in the position of the valve. Once the valve has started moving, it takes longer to move a large distance than a small distance, effectively resulting in a smaller bandwidth for large amplitude signals.

During the test phase it was realized that the overall accuracy of the displacement control would rapidly degrade at the higher speeds. Inspection of the displacement traces as a function of platen speed will reveal this aspect. The decision to conduct tests at 125 mm/s was based on a desire by the project team and clients to operate the test frame at the highest speed practical. The dominant frequency of the ice response in the Authors' opinion is not caused by the testing machine; nevertheless the response of the machine is likely to affect some details of the crushed ice behaviour.

5 Interpretation and Discussion

5.1 General

From previous laboratory and in situ crushing tests, it was felt that the extrusion of the crushed ice layer took place on the upward slope of each crushing event, and was a continuous process within each cycle. The development of a sawtooth pattern within the extrusion test itself indicates that extrusion may occur in a continuous, regular fashion with cyclic bursts superimposed between crushing events, and that two processes may in fact occur. Initially, as the platens move together the ice is continuously extruded and the layer thins. Flow is probably granular in nature, as indicated by the spiked "friction hill" pressure distributions usually observed in early test stages. As higher pressures develop the sawtooth pattern emerges and pressure distributions "flatten out".

During this high pressure stage of extrusion a cycle of solidification and recrushing may occur. At some locations within the crushed layer groups of particles may stick and sinter together under higher pressures, momentarily forming a semi-fused mass of crushed ice. During this time the pressure-time trace will begin to rise rapidly to a peak and little or no extrusion from the center region will occur. The recrushing of the mass into individual, possibly smaller, particles induces a sudden burst of extrusion and a drop in the pressure-time trace. Friction melting due to the sliding of ice particles over one another can also contribute to the formation of temporary groups. The water created will re-freeze once local motion is discontinued. Evidence of the presence of water in the crushed layer is the formation of a solid mass of fused ice in the center of the platens after the test is stopped.

Viscous theory predicts that the higher speed tests should meet with higher resistance instead of less as indicated by Figure 23. Considering the crushed layer on a microstructural basis, it is possible that the higher velocity between particles produces a greater degree of friction melting and subsequent lubricating water. Another explanation is that the momentum imparted to the crushed ice is greater at higher speeds and may explain why lower final thicknesses are achieved. Examination of the individual slopes

of the high-pressure fluctuations, however, indicates that extrusion is more difficult at higher speeds. If the individual peaks are to be modelled, a viscoplastic contribution can be included in the formulation to account for the increased resistance to motion at higher velocities.

5.2 Application of Mohr-Coulomb Model

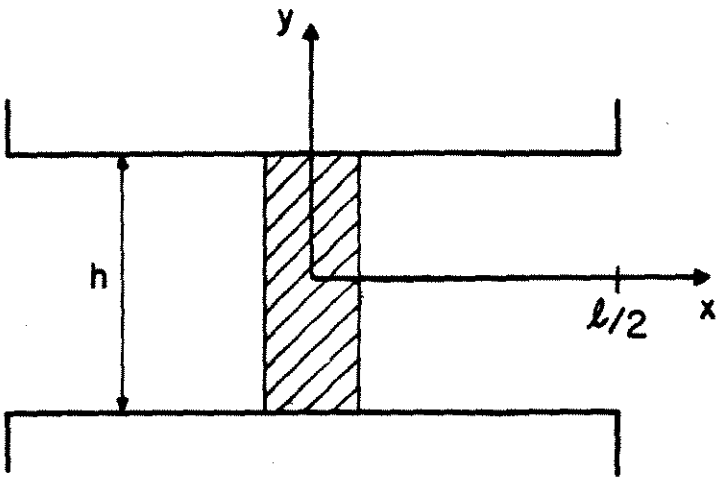

Figure 29: *"Triaxial" portion of crushed layer*

The crushed ice material may initially behave as a Mohr-Coulomb material. Figure 29 shows the central portion of the crushed material as a triaxial specimen, with effective shear and hydrostatic confining pressure developed by channels 8 and 9 such that

$$shear, \tau = \frac{Ch8 - Ch9}{2} \tag{24}$$

and

$$hydrostatic\ pressure, \sigma = \frac{Ch8 + Ch9}{2} \tag{25}$$

Mohr's envelope can be drawn for the central portion as the Channel 8 and 9 pressures (and consequently the hydrostatic pressure) increase to determine

the angle of internal friction, ϕ, and the cohesion, c. A plot of this envelope for X984 is shown in Figure 30. It can clearly be seen that the crushed material behaves as a granular material for the low pressure stage of extrusion. From a series of these plots for different speeds the angle of internal friction,ϕ, was found to be in the range of $31° - 39°$. For test X987 (2.5 mm/s) ϕ was found to lower from the Mohr envelope, approximately $11°$. The decline in ϕ may be due to an effect similar to damage-enhanced creep.

The y-intercept of this plot represents the material cohesion, c, which was found to be very small at low pressures, from 1 to 20 kPa. From these values of ϕ and c, the angle of wall friction, δ, was found to be between $1.2°$ and $2.5°$.

The Mohr-Coulomb model was best applied during the early stages of extrusion, or over the outer portion of the platen at higher pressures. A series of fits are given in Appendix 1 with the corresponding values of ϕ and δ used. Two fits are included here. The values typically used were in the range of $30° - 40°$, as predicted by the Mohr envelopes discussed above. Fits for X987 (2.5 mm/s), however, were obtained only by using a much higher value of ϕ than predicted by Mohr's envelope, approximately $40°$. Values of the friction angle between the material and the platen, δ, were slightly higher than predicted by the Mohr envelopes, from $1.5°$ to $3.0°$.

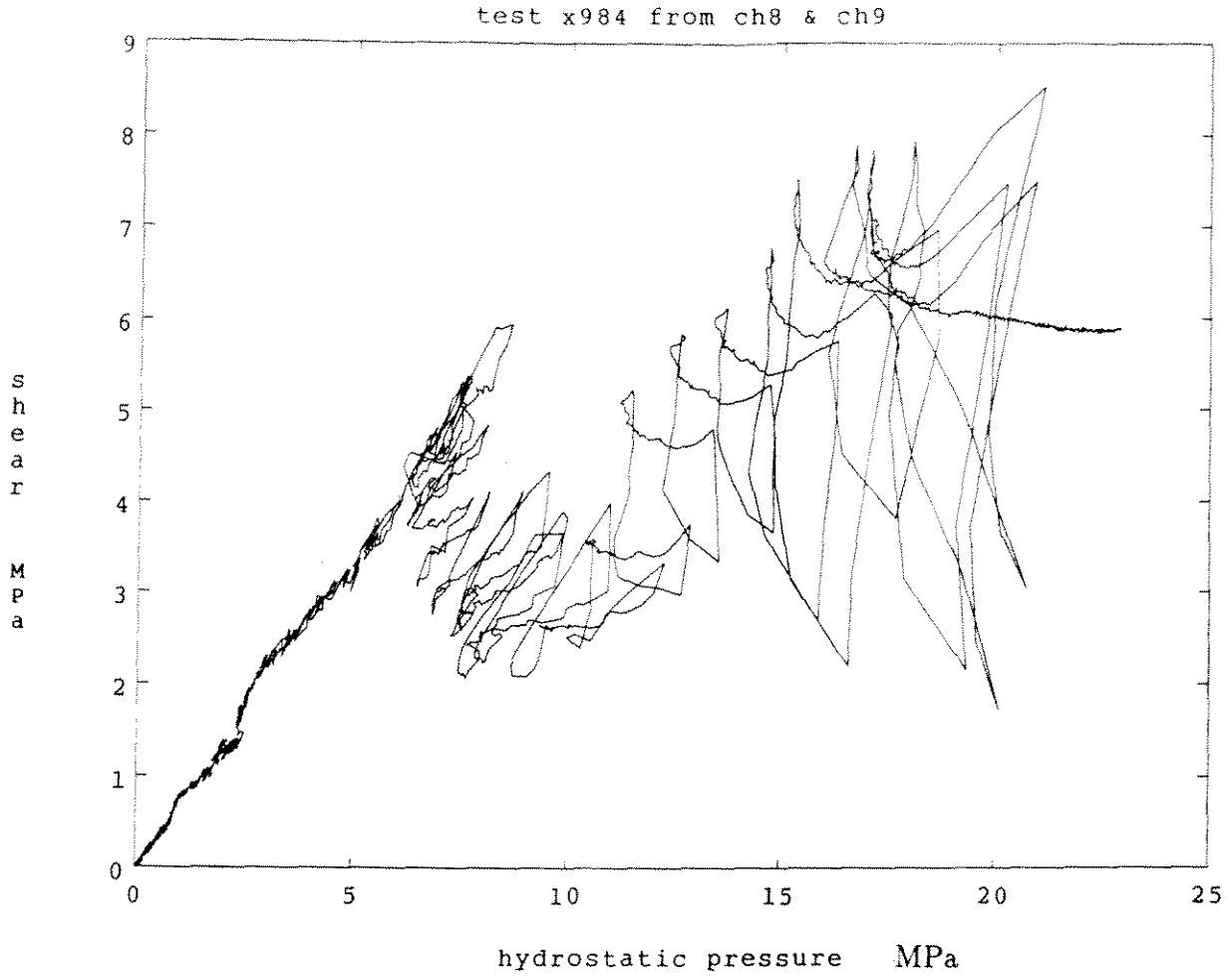

Figure 30: *Shear stress as a function of hydrostatic pressure for X984 (60 mm/s), showing linear behaviour for early portion of test*

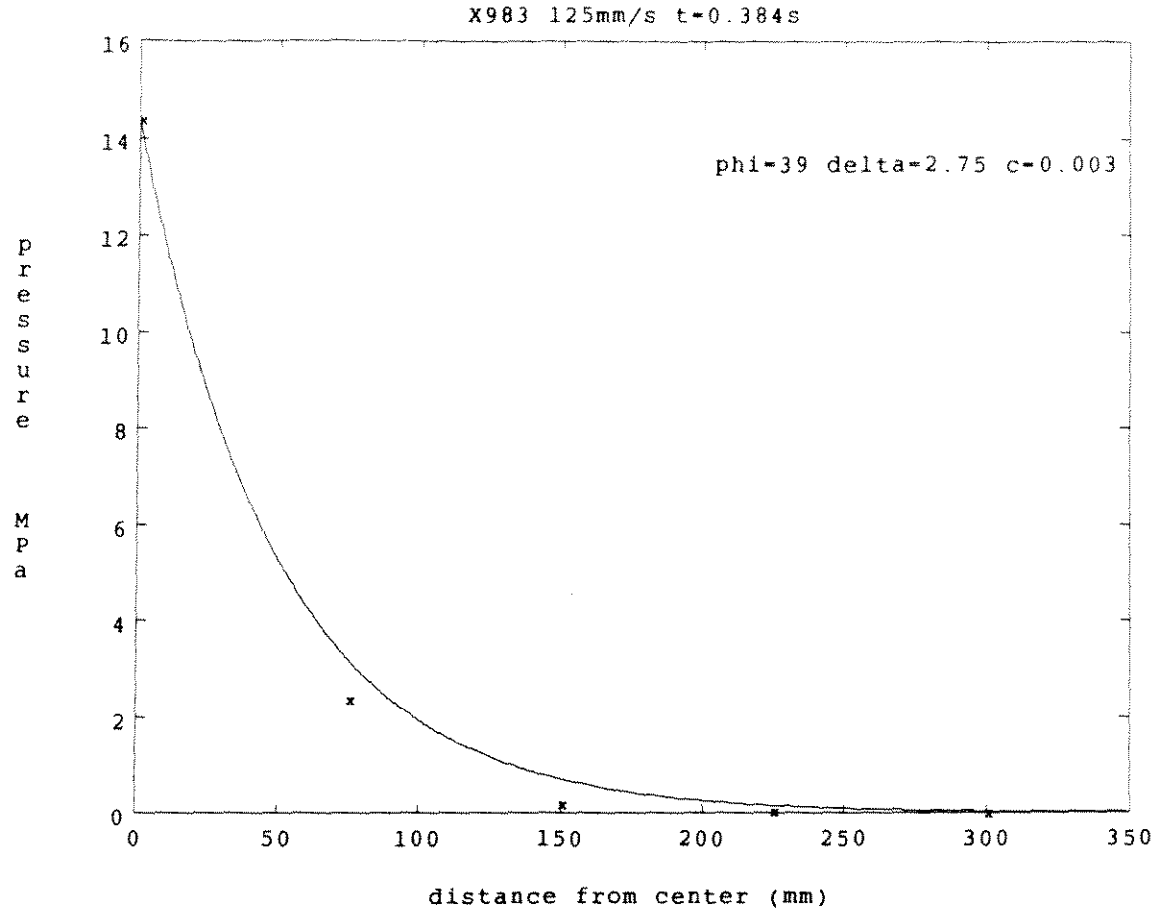

Figure 31: *Fit of Mohr-Coulomb model to early-stage pressure distribution*

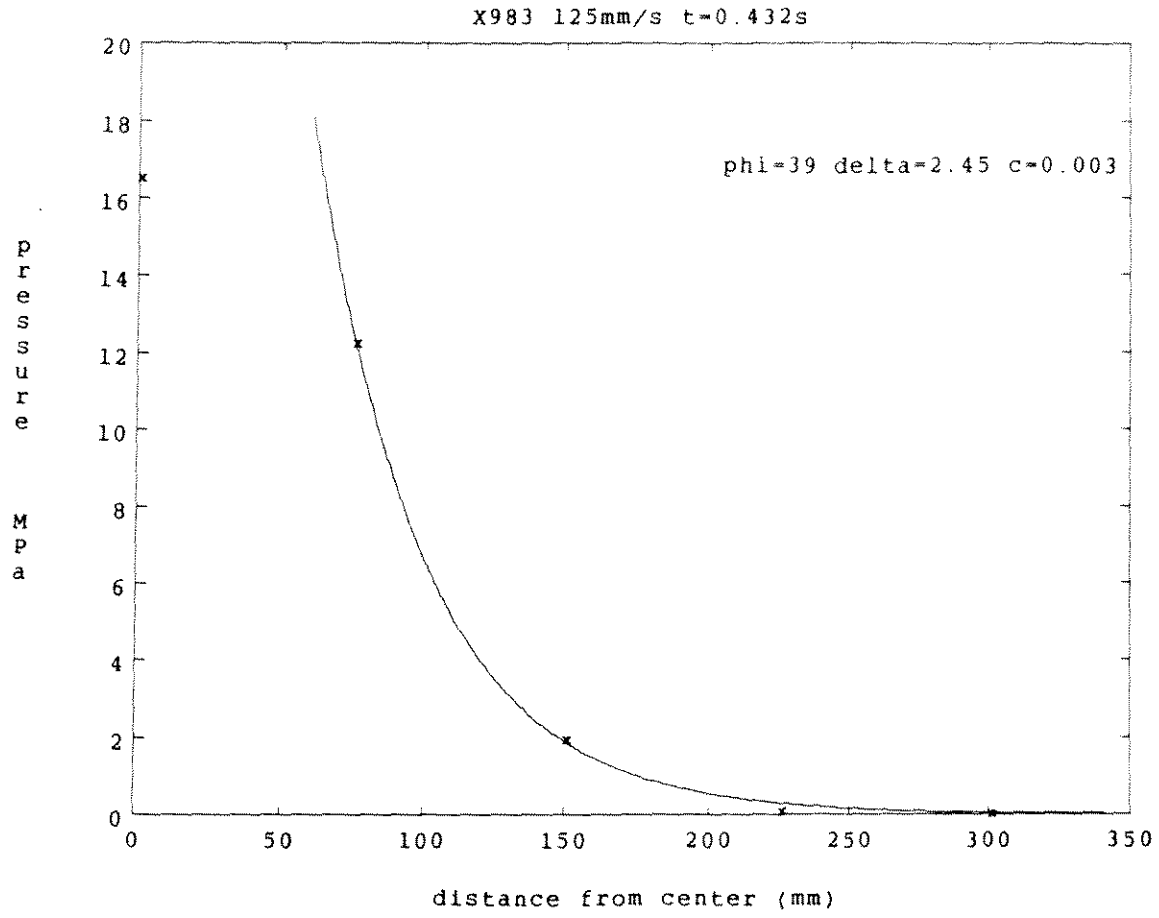

Figure 32: *Fit of Mohr-Coulomb model to outer portion of pressure distribution*

5.3 Application of Viscous Models

Examination of a number of pressure distributions reveals that the majority of the entire platen load is carried by the inner half of the platen. As discussed previously, this central portion of the distribution transforms from a Mohr-Coulomb spike to a flatter parabolic shape as the layer thins and pressures increase. The central portion of most pressure distributions can be modelled with a Newtonian or Bingham model. The material constants chosen to provide this fit were in keeping with accepted values. The best fits were made when the width of the "zone of influence" was used as the half-length of the extrusion channel in the particular model being applied. The appropriate "zone of influence" width was chosen by examining the pressure distribution at known test values of layer thickness, h, and platen velocity, v. Almost the entire load was carried over this central portion of the platen, and the pressures outside this zone were generally negligible.

5.3.1 Newtonian Fluid Model

The viscosity, μ, of the crushed layer was calculated using the pressure-density relationship defined in Equation 20 and assuming it was a Newtonian fluid. It was found to be rate-dependent, varying considerably from test to test. In addition, the viscosity was usually found to vary considerably from start to finish of a single test. Mean values ranged from 1.1 MPa-s for X987 (2.5 mm/s) to 0.0009 MPa-s for X996 (160 mm/s). The calculated value of μ fluctuated with the individual sawteeth, but a mean value was used in the Newtonian model to provide a fit to the central portion of the high-pressure stage pressure distribution. A typical fit is shown in Figure 33.

Values of μ used for fits were typically from 0.003 to 0.02 MPa-s for 125 mm/s tests, 0.03 to 0.15 MPa-s for 25 mm/s tests, and 0.2 to 1.1 MPa-s for 2.5 and 5 mm/s tests. The slopes of the individual rises (fluctuations in the overall curve) indicate an opposite rate dependence: the difficulty of extrusion increases with rate. It may perhaps be more appropriate to fit material parameters to these individual slopes.

5.3.2 Bingham Plastic Model

When applying the Bingham model, the viscosity of the crushed layer was assumed to be approximately the same as that of a Newtonian fluid, and

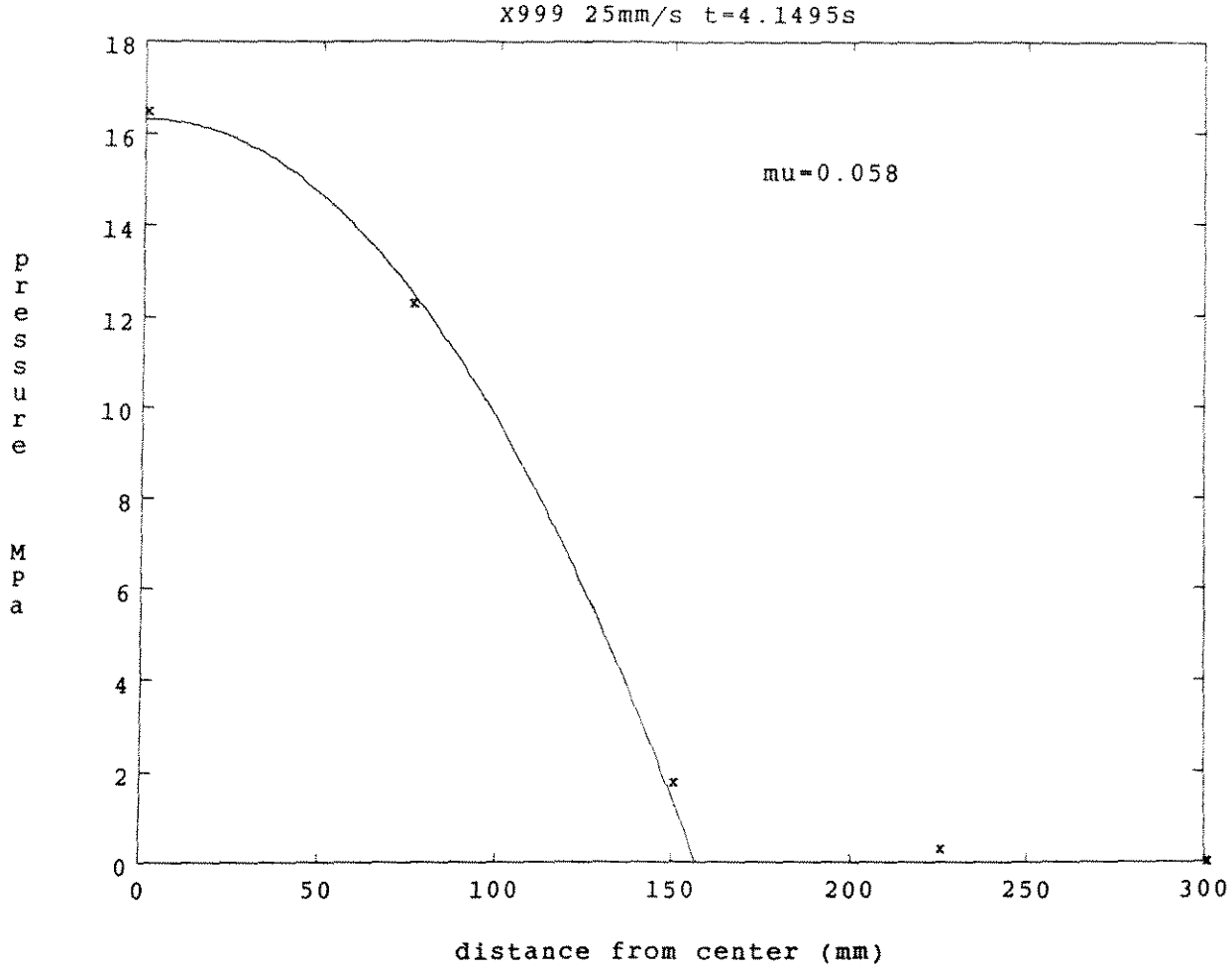

Figure 33: *Fit of Newtonian Model to central portion of pressure distribution*

a small fluid shear strength, τ_y, was included in the model. A typical fit, similar to that of the Newtonian model is shown in Figure 34. Typical values of viscosity used were in the same range as those of the Newtonian model for flatter parabolic pressure distributions. The value of material shear strength, τ_y, varied from 0.001 to 0.03 kPa for these cases.

When τ_y was increased by one or two orders of magnitude and μ decreased slightly, the fit was forced to flatten out. In this way a close approximation to a peaked pressure distribution could be made, as seen in Figure 35. Values of τ_y were between 0.1 and 0.3 MPa, while μ varied from 0.001 to 0.003 MPa-s.

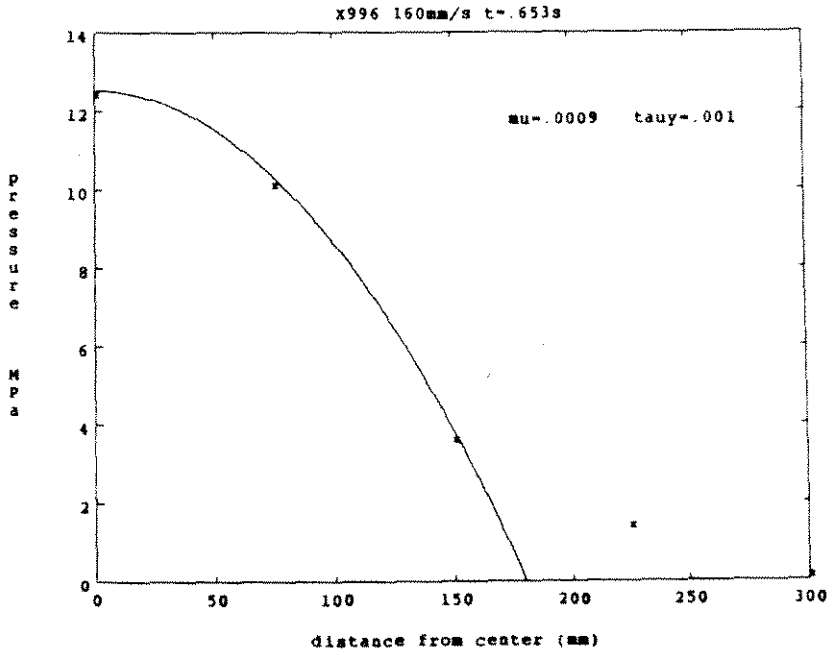

Figure 34: *Fit of Bingham model to pressure distribution*

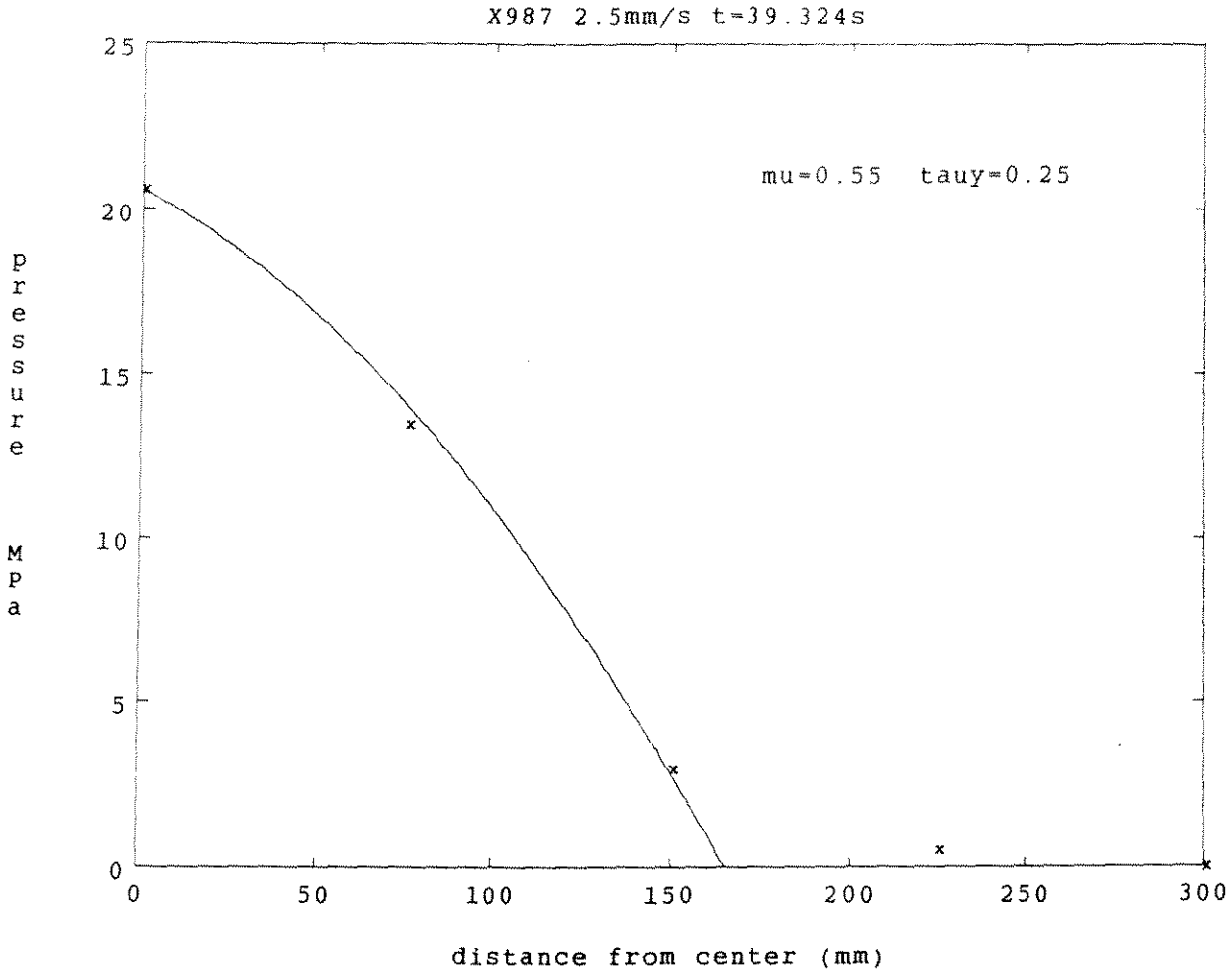

Figure 35: *Fit of Bingham model to peaked pressure distribution*

6 Analysis of Crushing-Extrusion Tests

Seven tests, Y001 to Y007, were performed on cylindrical samples of solid and pre-crushed ice (Y001 only) in a chamber of diameter 127 mm. Slots were cut at the bottom of the chamber sides to allow extrusion of the crushed ice. The load applied to the plunger, the local pressure at the chamber centre, and the plunger displacement were measured.

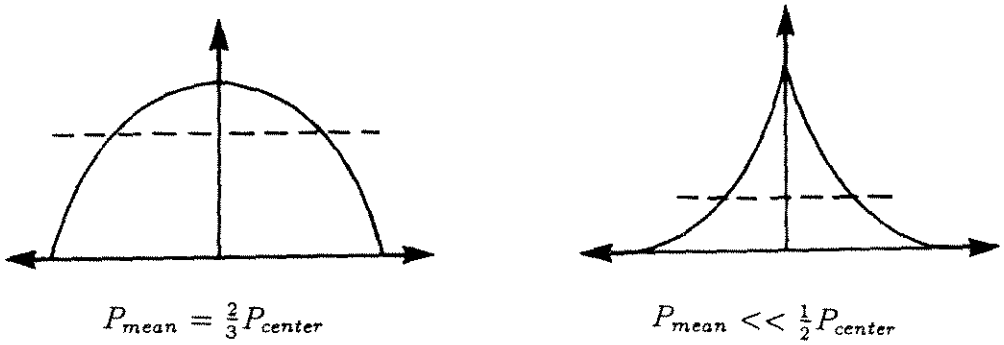

Figure 36: *Mean pressure for different pressure distributions*

For a viscous pressure distribution the average pressure is approximately two-thirds the maximum central pressure. For a Mohr-Coulomb type pressure distribution, the average pressure is much less than one half the central pressure (see Figure 36). A comparison of the centre pressure with the mean pressure for the crushing tests Y002-Y007 may indicate which type of pressure distribution is favoured. Test Y001 was performed on a cylindrical mass of crushed ice, and will also be included in this analysis for reference.

The centre pressure and mean pressure were sampled for a number of points in each test. If the area supporting the total load is reduced to take spalling into account, the mean pressure will increase. The mean spall for all tests was taken as an ellipse of 26 by 13 mm, based on sieve analysis of

spalled ice pieces from the tests (Volume 1). The average ratio of corrected mean pressure to centre pressure for each test is given in Table 1.

Test	*Speed (mm/s)*	P_{mean}/P_{center}
Y001	4	0.59
Y002	4	0.49
Y003	2	0.49
Y005	25	0.44
Y006	15	0.71
Y007	125	0.78

Most of these values of P_{mean}/P_{centre} correspond to a pressure distribution of parabolic shape, i.e. flattening out near the centre rather than increasing exponentially. If the extrusion load is carried predominantly by the inner half of the intact ice sample (as for the extrusion tests), the mean pressure for that region will be even greater.

Spectral analysis was performed on tests exhibiting cyclic behaviour (Y002, Y003 and Y006). A plot of these frequencies as a function of test speed is shown in Figure 37. A linear fit has been superimposed.

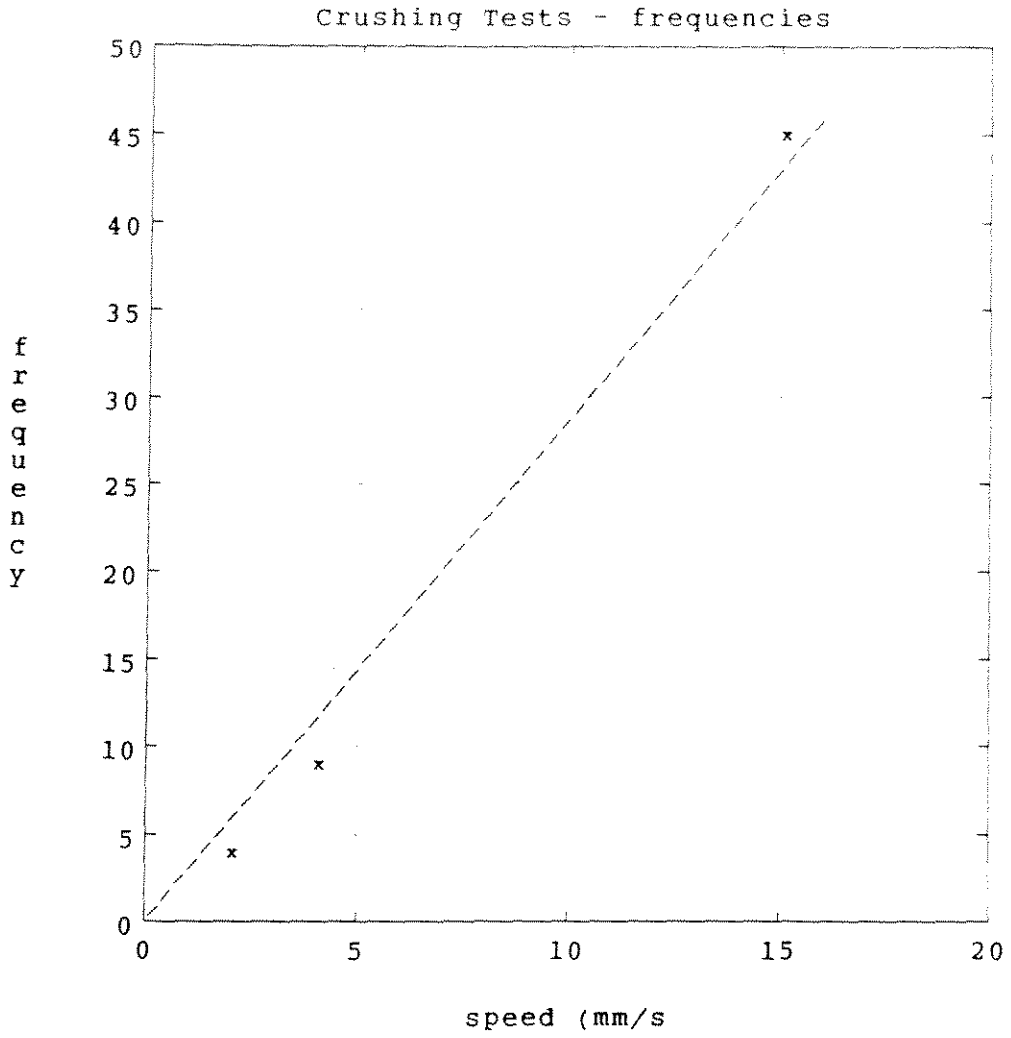

Figure 37: *Frequency as function of test speed for crushing-extrusion tests Y002, Y003 and Y006.*

7 Conclusions and Recommendations

The test program provided an interesting set of results which gave new insights into the extrusion process of ice. In particular, the observation of fluctuations of load within a thin layer was not expected and shows that the nature of the process changes at a certain pressure (approximately 5-10 MPa) to include this fluctuation. The following conclusions can be drawn:

(1) At lower pressures (below approximately 7 MPa), the flow of crushed ice is similar to that of granular materials, with wedge-shaped failure planes. This has been supported by visual observation, and the Mohr-Coulomb theory provides a reasonable model of this phase of the process. Typical values of the parameters are:

$$\phi \text{ , internal friction angle} \rightarrow 31^{o} - 39^{o}$$
$$\delta \text{ , platen/material friction angle} \rightarrow 1.5^{o} - 3.0^{o}$$
$$c \text{ , material cohesion} \rightarrow 0.001 - 0.03 MPa$$

(2) An important aspect that permits conclusions to be drawn relating to the constitutive models of crushed ice is the shape of the pressure distribution. The data at lower pressures agrees well with that given by Mohr-Coulomb theory. At pressures of about 5-10 MPa fluctuations in load commenced and at the same time, the pressure distribution flattened out, indicating a departure from Mohr-Coulomb theory. These zones of local high pressure are likely to dominate the situation in the field.

(3) After completion of the tests, the central zone in the crushed ice was observed to be fused together, indicating a change in the process: possibly sintering and "reverse damage" processes are in evidence.

(4) Modelling of the general trend of the results, i.e. ignoring the details of the load fluctuations, yields values of viscosity that range from 1.05 MPa-s at 2.5 mm/s to 0.0009 MPa-s at 160 mm/s.

(5) It might be argued that the individual rises in load during the fluctuations of value should be modelled. The slopes of these rises were studied. The increasing slope with velocity is evidence of a rate-dependent effect in the individual rises, and suggests that fitting material parameters to these individual slopes may be more appropriate than modelling the overall curve. Values of these slopes ranged from about 5 MPa/mm at 25 mm/s to about 10 MPa/mm at 125 mm/s at the center of the platen.

(6) An approximately linear relationship exists between test velocity and the frequency of fluctuations in the higher pressures near the platen centre.

(7) Examination of the crushing tests indicates that the pressure distribution during these tests was generally not pointed, but of a parabolic nature. The frequency of individual fluctuations in these tests also displayed a linear increase with speed.

References

Cottrell, A.H.,1964, *The Mechanical Properties of Matter*, John Wiley and Sons Inc., New York.

Evans, D.C.B., Nye, J.F., and Cheeseman, K.J., 1976, "The Kinetic Friction of Ice", *Proc. Royal Society of London, Series A*, Vol.347, pp.493-512.

Hallam, S.D., and Pickering, J.G., 1988, "Modelling of Dynamic Ice Loading of Offshore Arctic Structures", *POLARTECH 88 - Proc. for Int. Conf. on Tech. for Polar Areas*, Vol.1, Trondheim, pp.235-248.

Jeffries, M.G., and Wright, W.H., 1988, "Dynamic Response of Molikpaq to Ice-Structure Interaction", *Proc. of 7th Int. O.M.A.E. Conference*, Vol.4, Houston, pp.201-220.

Jordaan, I.J. and Timco, G.W., 1988, "Dynamics of the Ice Crushing Process", *Journal of Glaciology*, Vol.34, No.118, pp.318-325.

GEOTECH and M.U.N., 1988, "Flow of Crushed Ice: Physical and Mechanical Properties and Behaviour - Proposal", proposal submitted by GEOTECHnical resources ltd. and Ocean Engineering Research Centre, Memorial University of Newfoundland.

GEOTECH, 1989, "Flow of Crushed Ice: Physical and Mechanical Properties and Behaviour - Volume 1", report submitted by GEOTECHnical resources ltd.

Kurdyumov, V.A., and Kheisin, D.E., 1976, "Hydrodynamic model of the impact of a solid on ice", *Prikladnaya Mekhanika*, Vol.12, No.10, pp.103-109.

Massey, B.S., 1982, *Mechanics of Fluids (5th ed.)*, Van Nostrand Reinhold (U.K.).

Nordell, B., 1989, "Pressure Melting of Ice", *POAC 89*, pp.249-258.

Oksanen, P., 1982, "The Mechanism of Friction of Ice", *Wear*, Vol.78, pp.315-324.

Paul, B., 1968, "Macroscopic Criteria for Plastic Flow and Brittle Fracture", in *Fracture - An Advanced Treatise*, (H.Liebowitz, ed.), Vol.2, Academic Press, New York, pp.315-496.

Savage, S.B., 1989, "Analysis of two-dimensional extrusion of granular ice between curved plates", Report for N.R.C., Contract No. 988-44174R, Ottawa.

Singh, S., 1989, Ph.D. thesis in preparation, Memorial University of Newfoundland.

Spencer, A.J., 1964, "A Theory of the Kinematics of Ideal Soils Under Plane Strain Conditions", *Jour. of Mech. and Phys. of Solids*, Vol.12, pp.337-351.

Tabor, D., 1981, "Friction - The Present State of our Understanding", *Jour. of Lubrication Tech.*, Vol.103, pp.169-179.

Appendix 1 : Mohr-Coulomb Fits

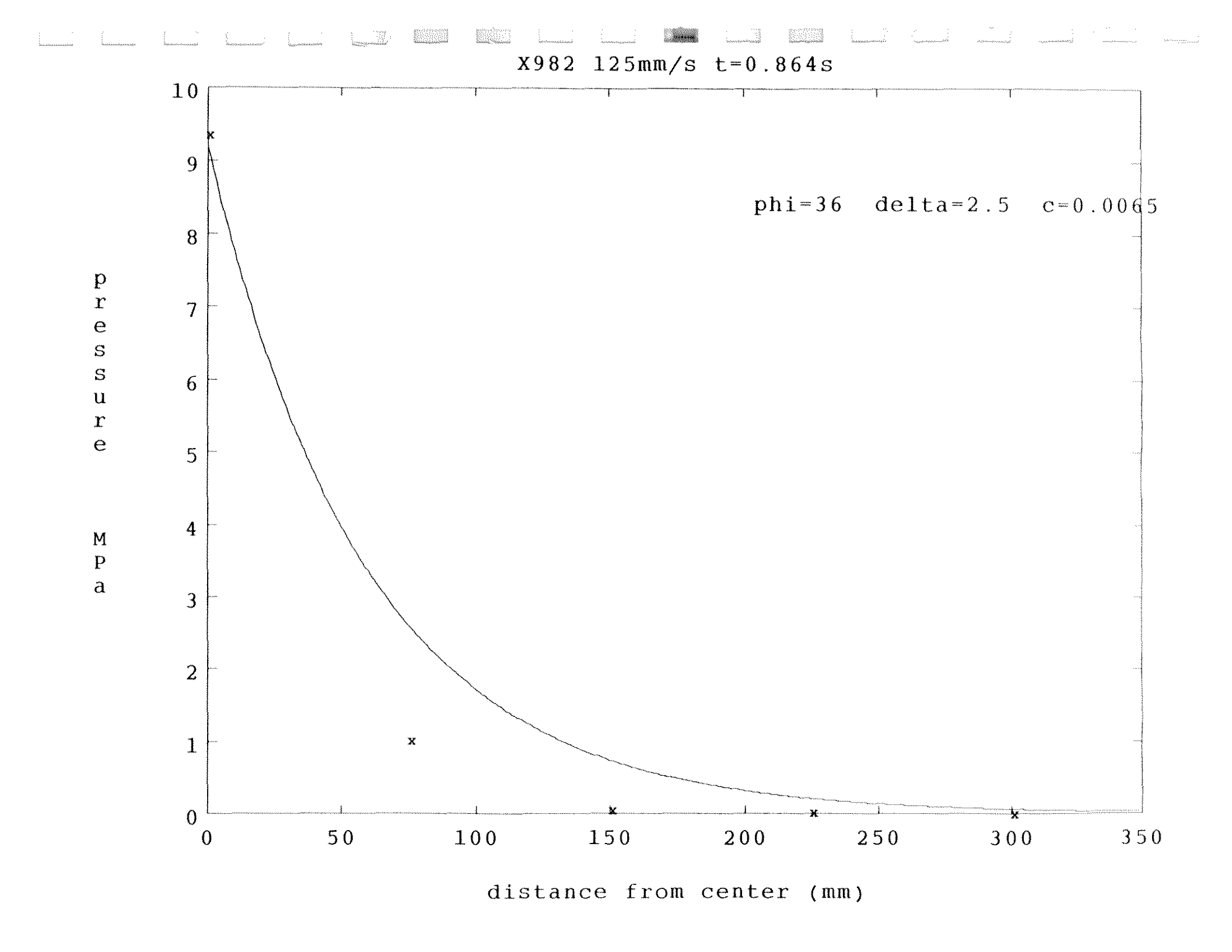
X982 125mm/s t=0.864s
phi=36 delta=2.5 c=0.0065
pressure MPa
distance from center (mm)
0
1
2
3
4
5
6
7
8
9
10
0
50
100
150
200
250
300
350

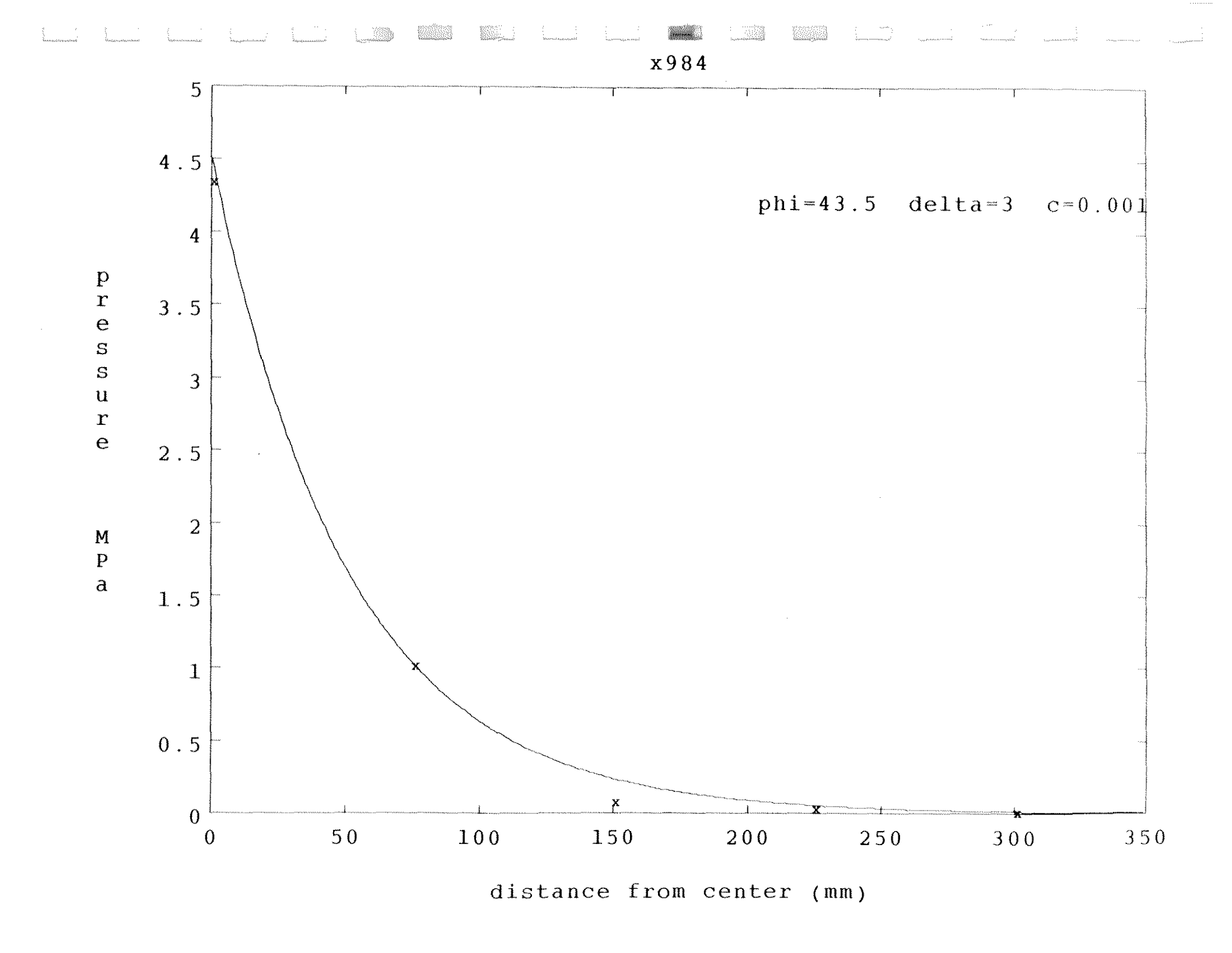
x984
phi=43.5 delta=3 c=0.001
pressure MPa
distance from center (mm)
0
0.5
1
1.5
2
2.5
3
3.5
4
4.5
5
0
50
100
150
200
250
300
350

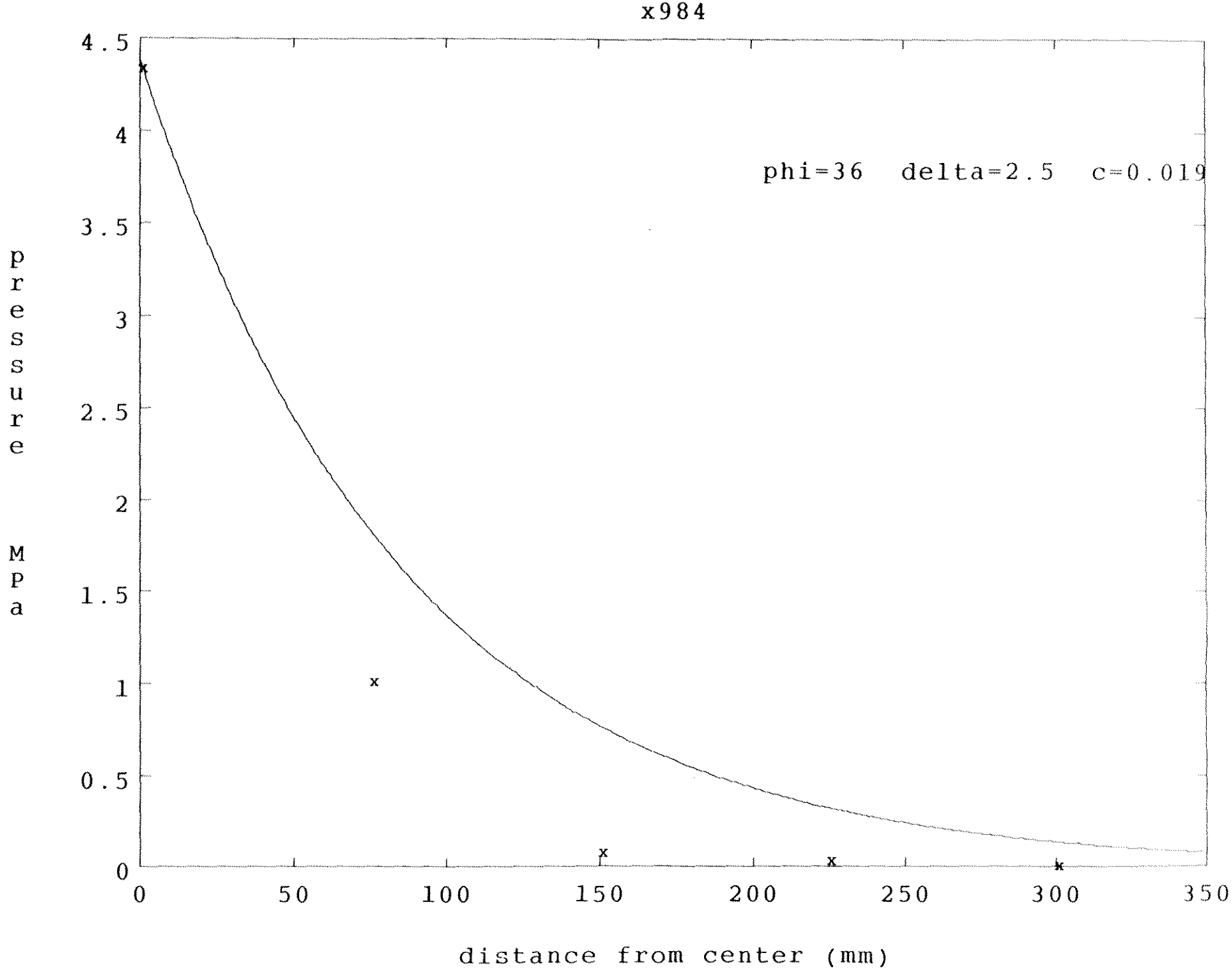
x984
phi=36 delta=2.5 c=0.019
pressure MPa
distance from center (mm)
0
0.5
1
1.5
2
2.5
3
3.5
4
4.5
0
50
100
150
200
250
300
350

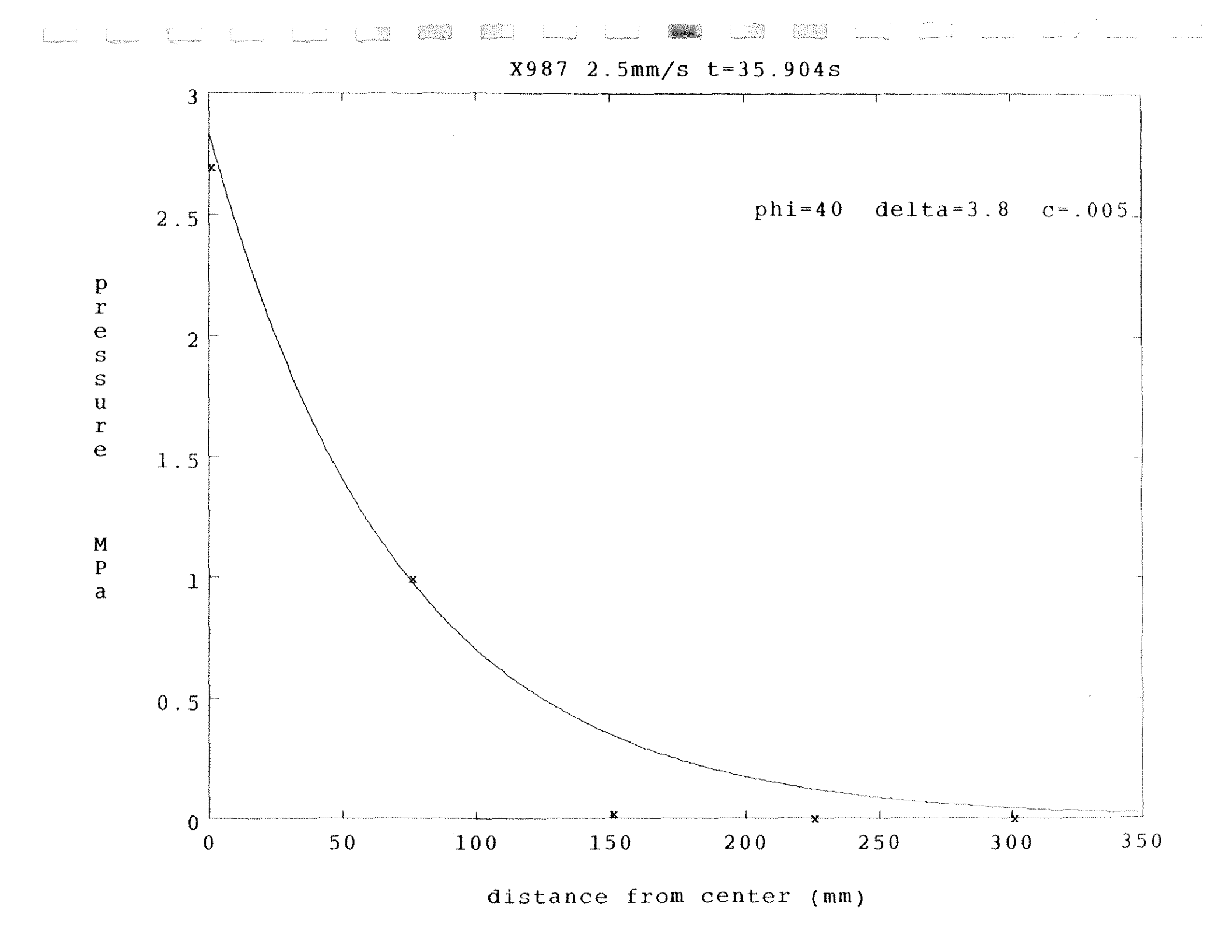
X987 2.5mm/s t=35.904s
phi=40 delta=3.8 c=.005
pressure MPa
distance from center (mm)
0
0.5
1
1.5
2
2.5
3
0
50
100
150
200
250
300
350

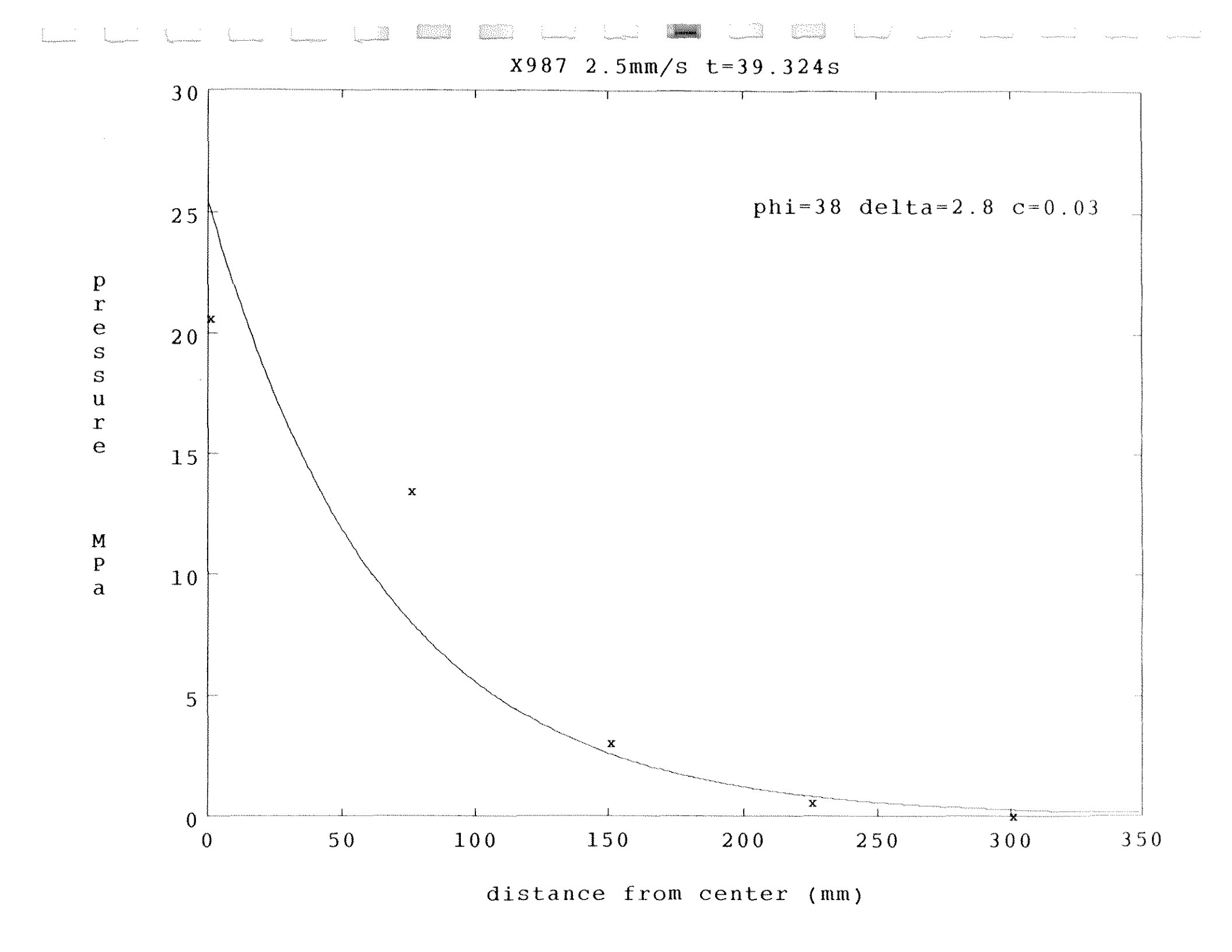
X987 2.5mm/s t=39.324s
phi=38 delta=2.8 c=0.03
pressure MPa
distance from center (mm)
0
5
10
15
20
25
30
0
50
100
150
200
250
300
350

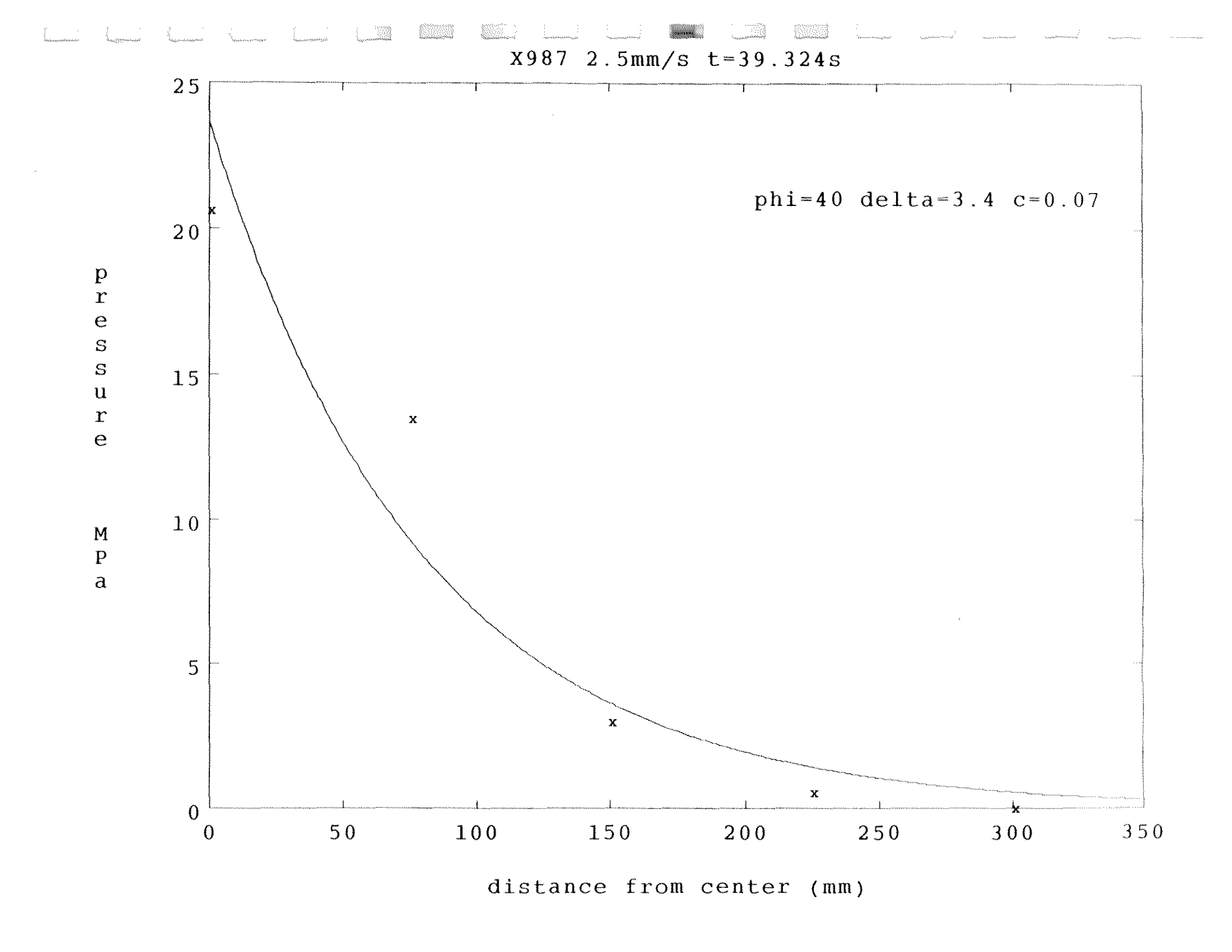
X987 2.5mm/s t=39.324s
phi=40 delta=3.4 c=0.07
pressure MPa
distance from center (mm)
0
5
10
15
20
25
0
50
100
150
200
250
300
350

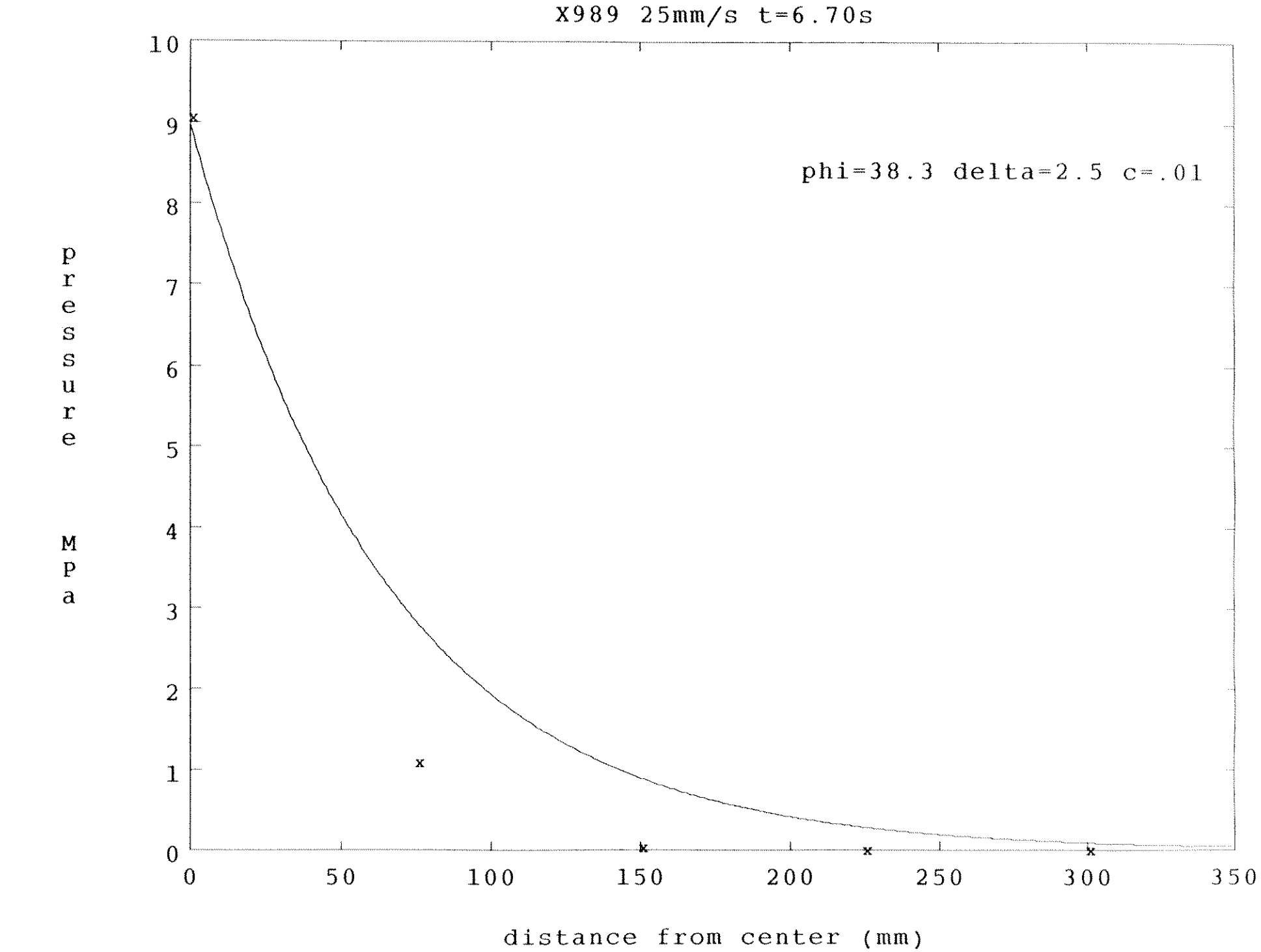
X989 25mm/s t=6.70s
phi=38.3 delta=2.5 c=.01
pressure MPa
distance from center (mm)
0
1
2
3
4
5
6
7
8
9
10
0
50
100
150
200
250
300
350

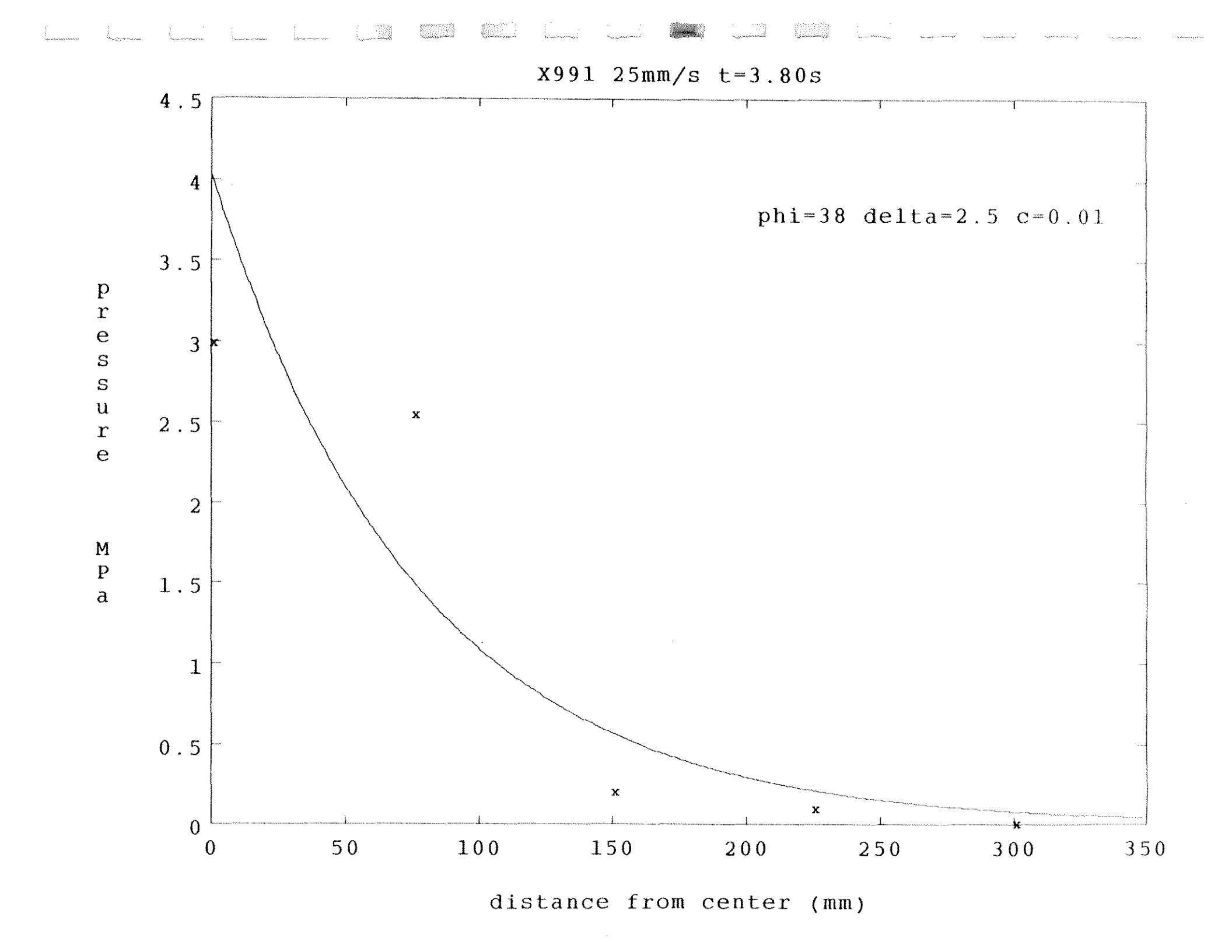
X991 25mm/s t=3.80s
phi=38 delta=2.5 c=0.01
pressure MPa
4.5
4
3.5
3
2.5
2
1.5
1
0.5
0
0
50
100
150
200
250
300
350
distance from center (mm)

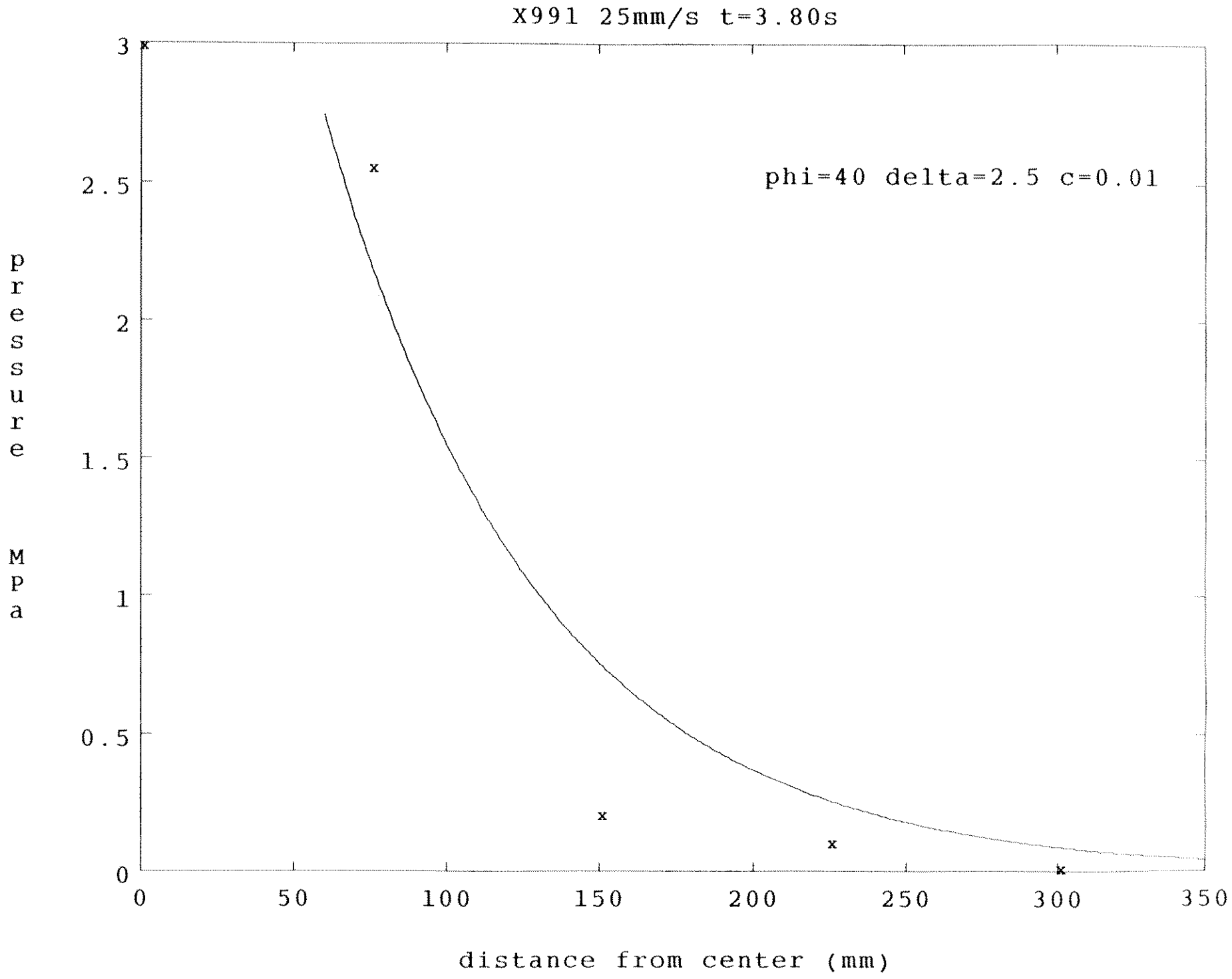
X991 25mm/s t=3.80s
phi=40 delta=2.5 c=0.01
pressure MPa
distance from center (mm)
0
0.5
1
1.5
2
2.5
3
0
50
100
150
200
250
300
350

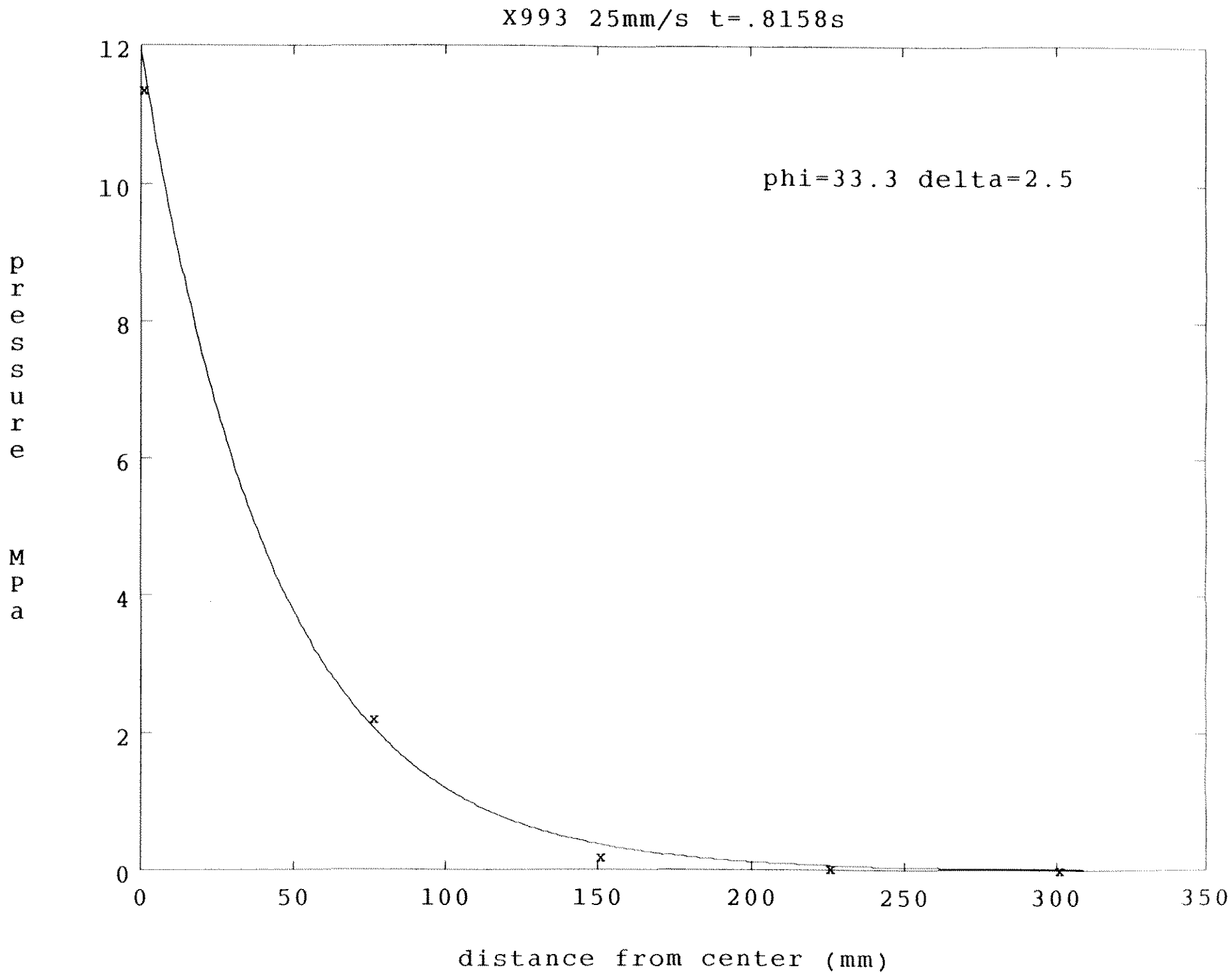
X993 25mm/s t=.8158s
phi=33.3 delta=2.5
pressure MPa
distance from center (mm)
0
2
4
6
8
10
12
0
50
100
150
200
250
300
350

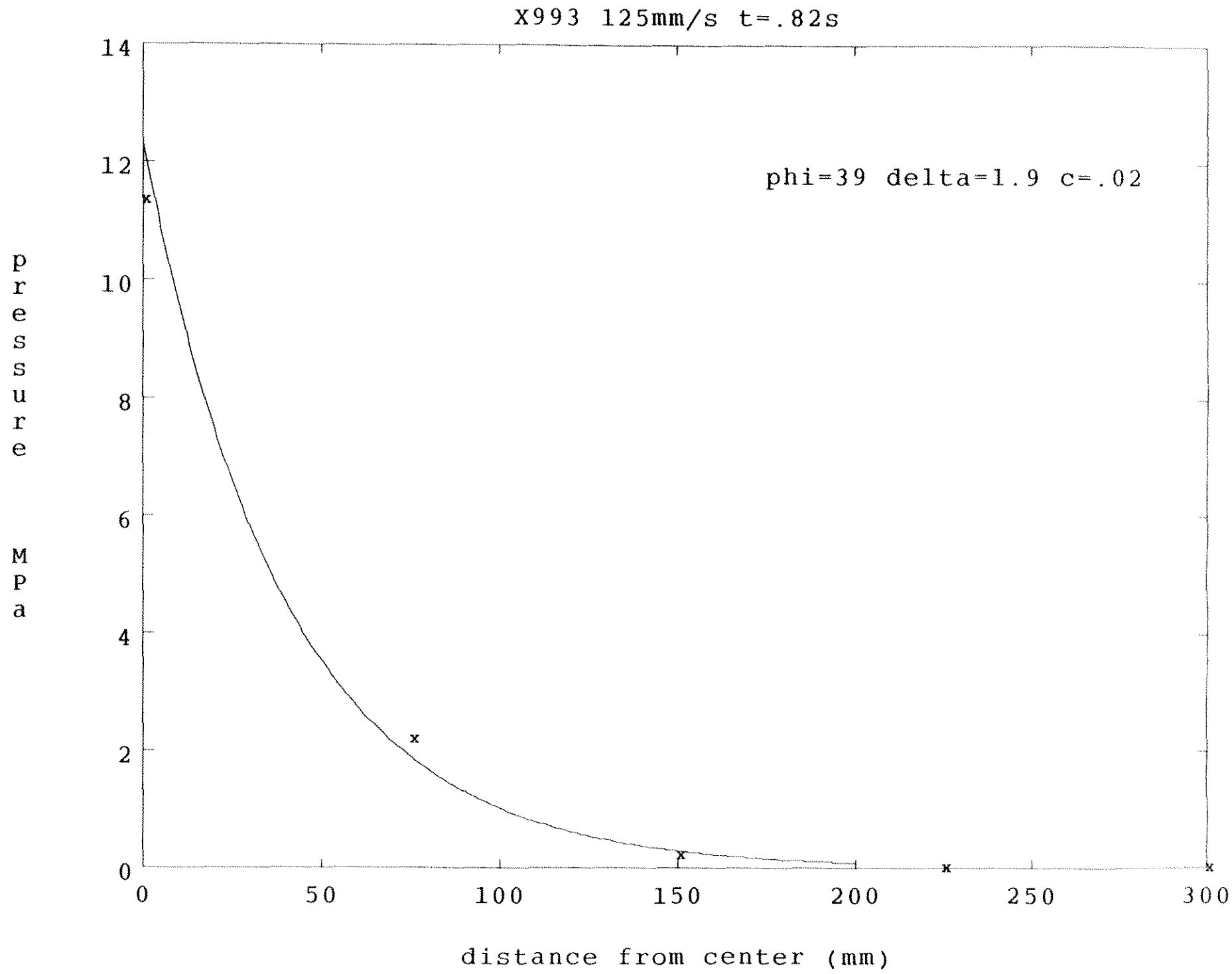
X993 125mm/s t=.82s
phi=39 delta=1.9 c=.02
pressure MPa
0
2
4
6
8
10
12
14
0
50
100
150
200
250
300
distance from center (mm)

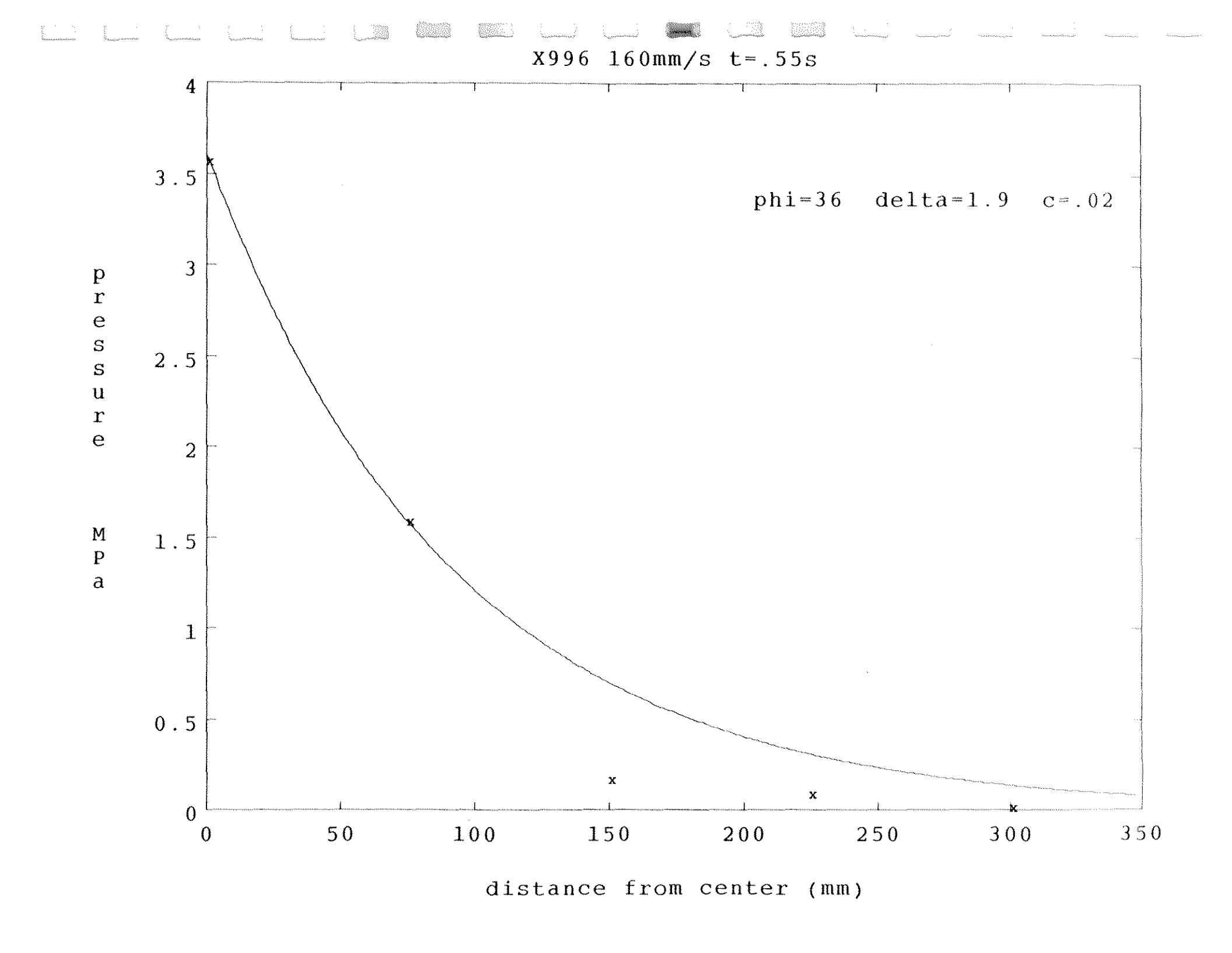
X996 160mm/s t=.55s
phi=36 delta=1.9 c=.02
pressure MPa
distance from center (mm)
0
0.5
1
1.5
2
2.5
3
3.5
4
0
50
100
150
200
250
300
350

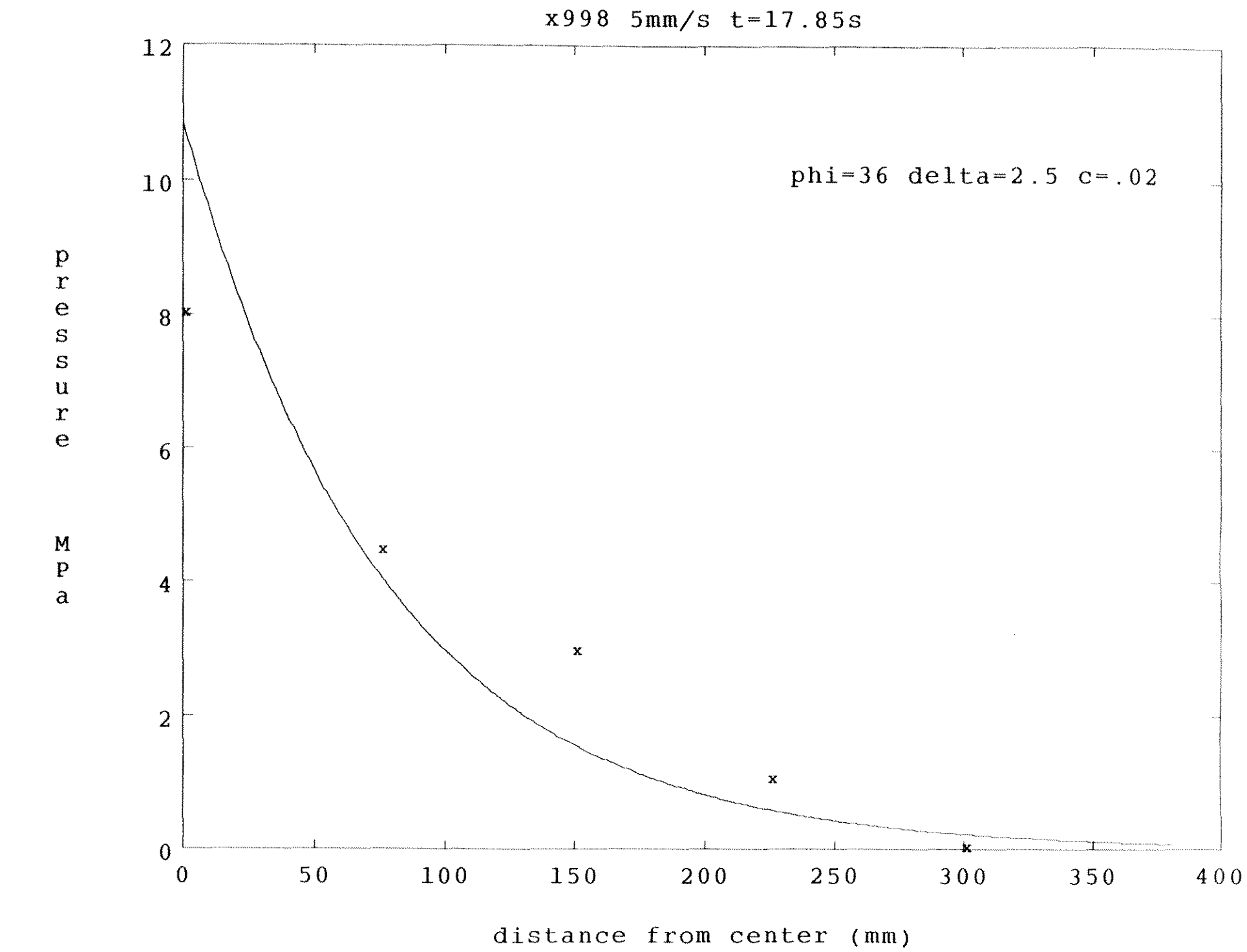
x998 5mm/s t=17.85s
phi=36 delta=2.5 c=.02
pressure
MPa
distance from center (mm)
0
2
4
6
8
10
12
0
50
100
150
200
250
300
350
400

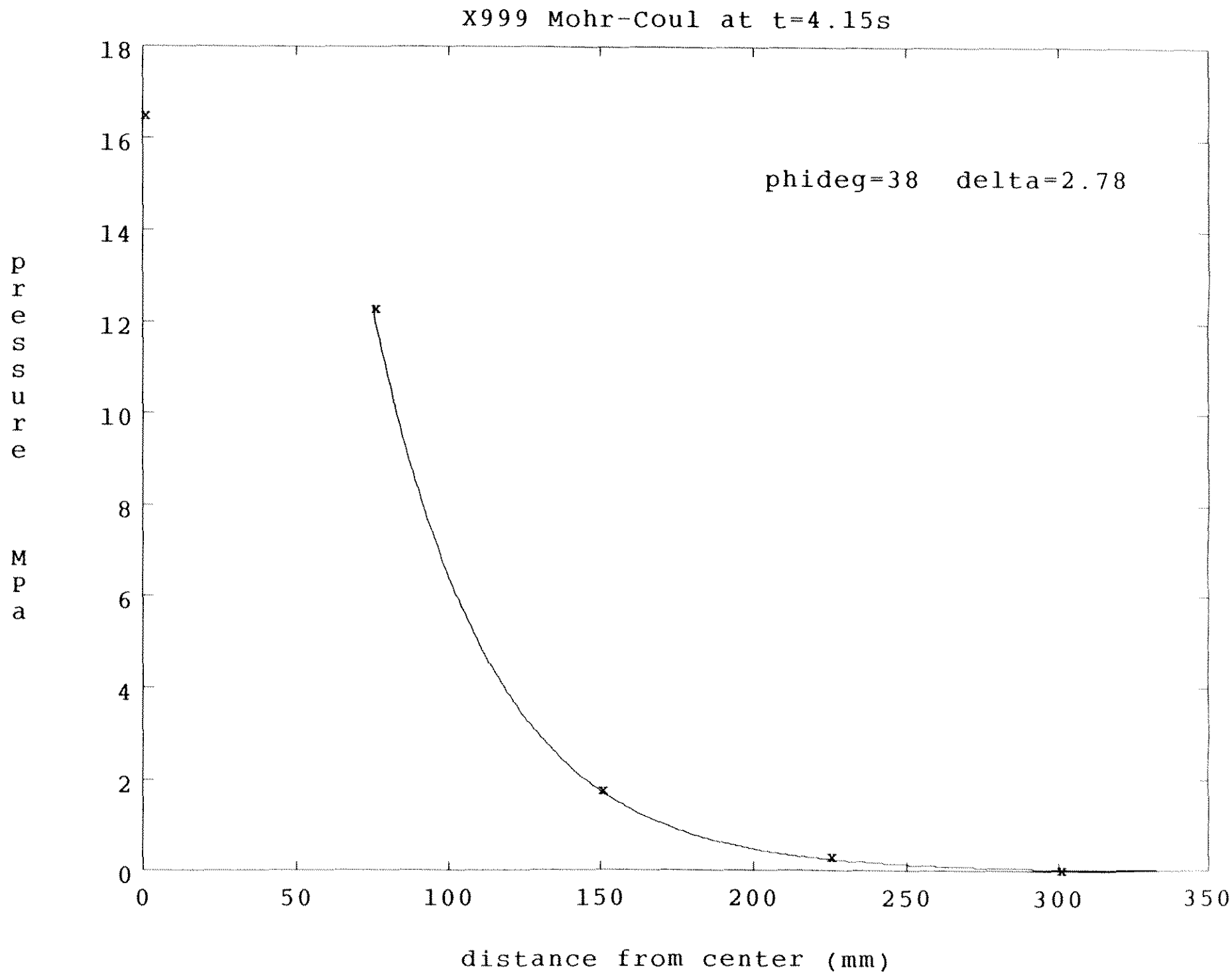
X999 Mohr-Coul at t=4.15s
phideg=38 delta=2.78
pressure MPa
distance from center (mm)
0
2
4
6
8
10
12
14
16
18
0
50
100
150
200
250
300
350

Appendix 2 : Newtonian Fits

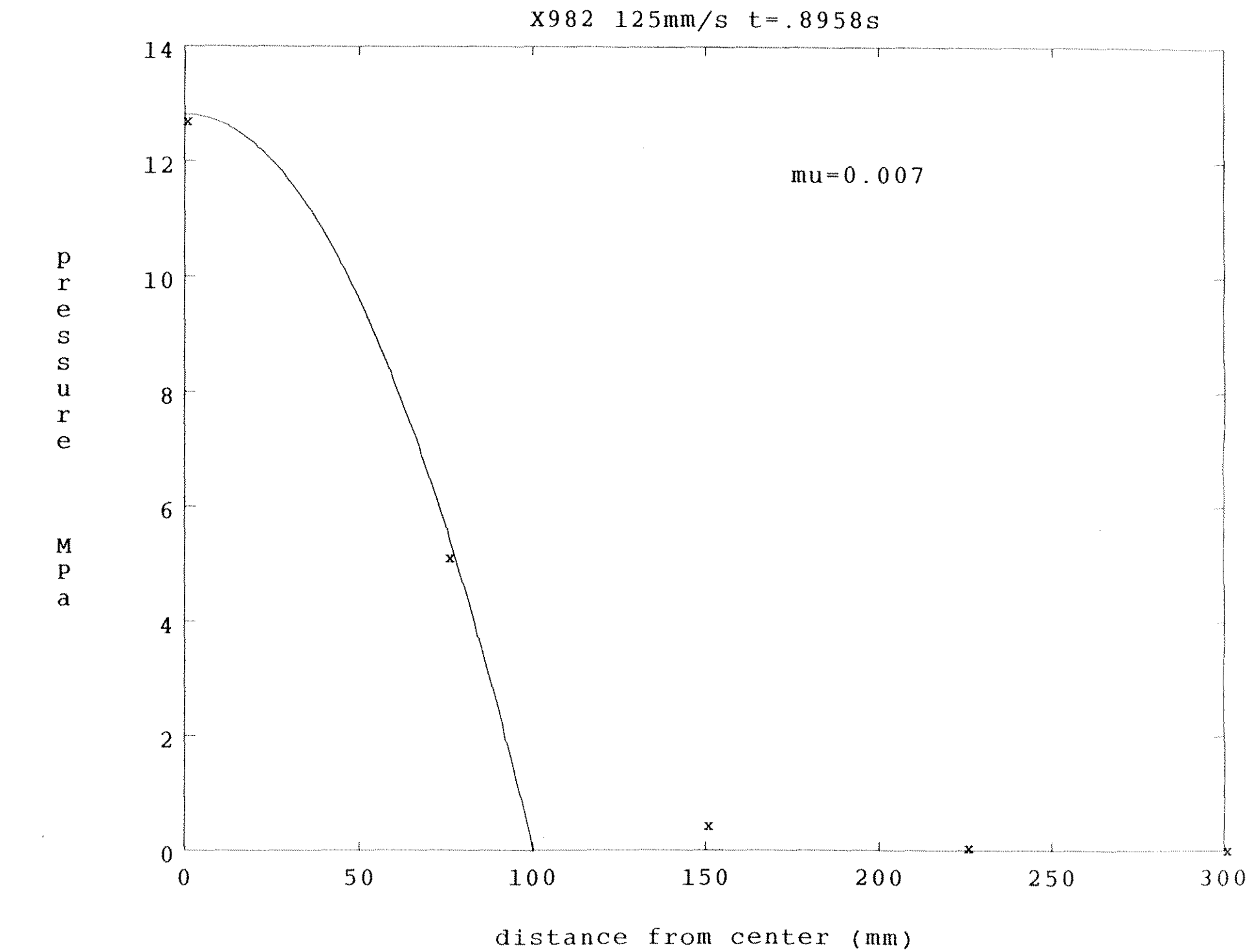
X982 125mm/s t=.8958s
mu=0.007
pressure MPa
distance from center (mm)
0
2
4
6
8
10
12
14
0
50
100
150
200
250
300

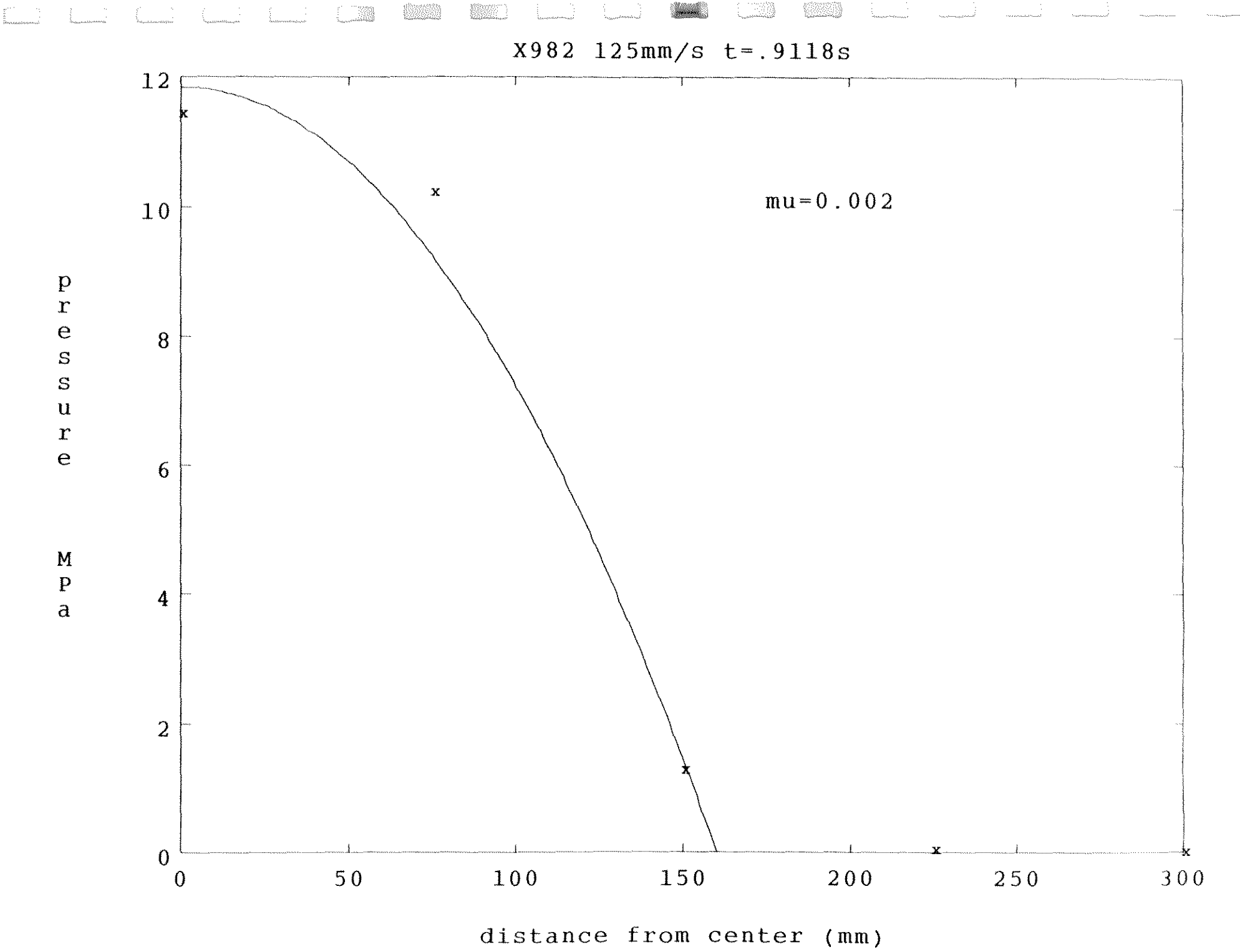
X982 125mm/s t=.9118s
mu=0.002
pressure MPa
distance from center (mm)
0
2
4
6
8
10
12
0
50
100
150
200
250
300

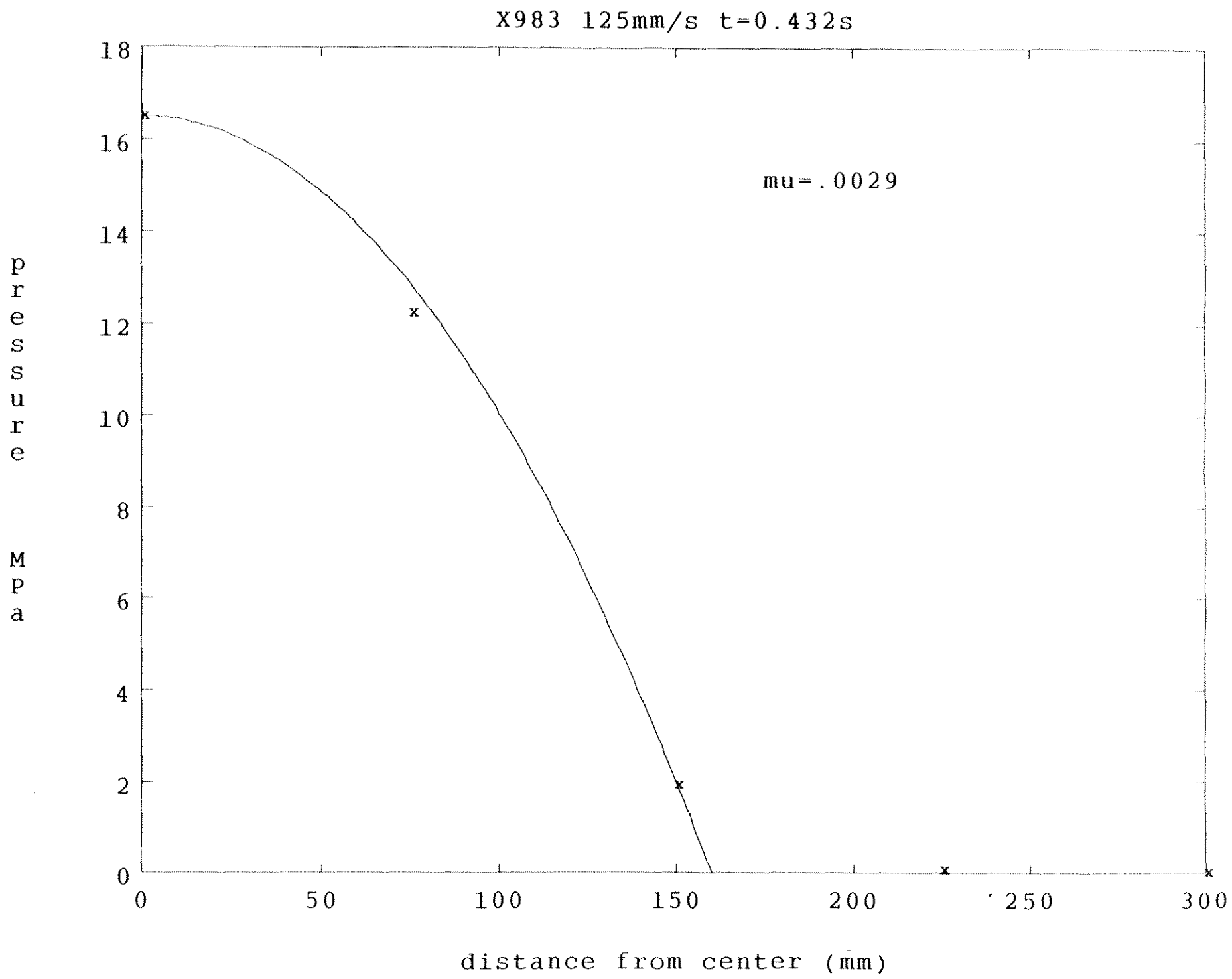
X983 125mm/s t=0.432s
mu=.0029
pressure MPa
distance from center (mm)
0
2
4
6
8
10
12
14
16
18
0
50
100
150
200
250
300

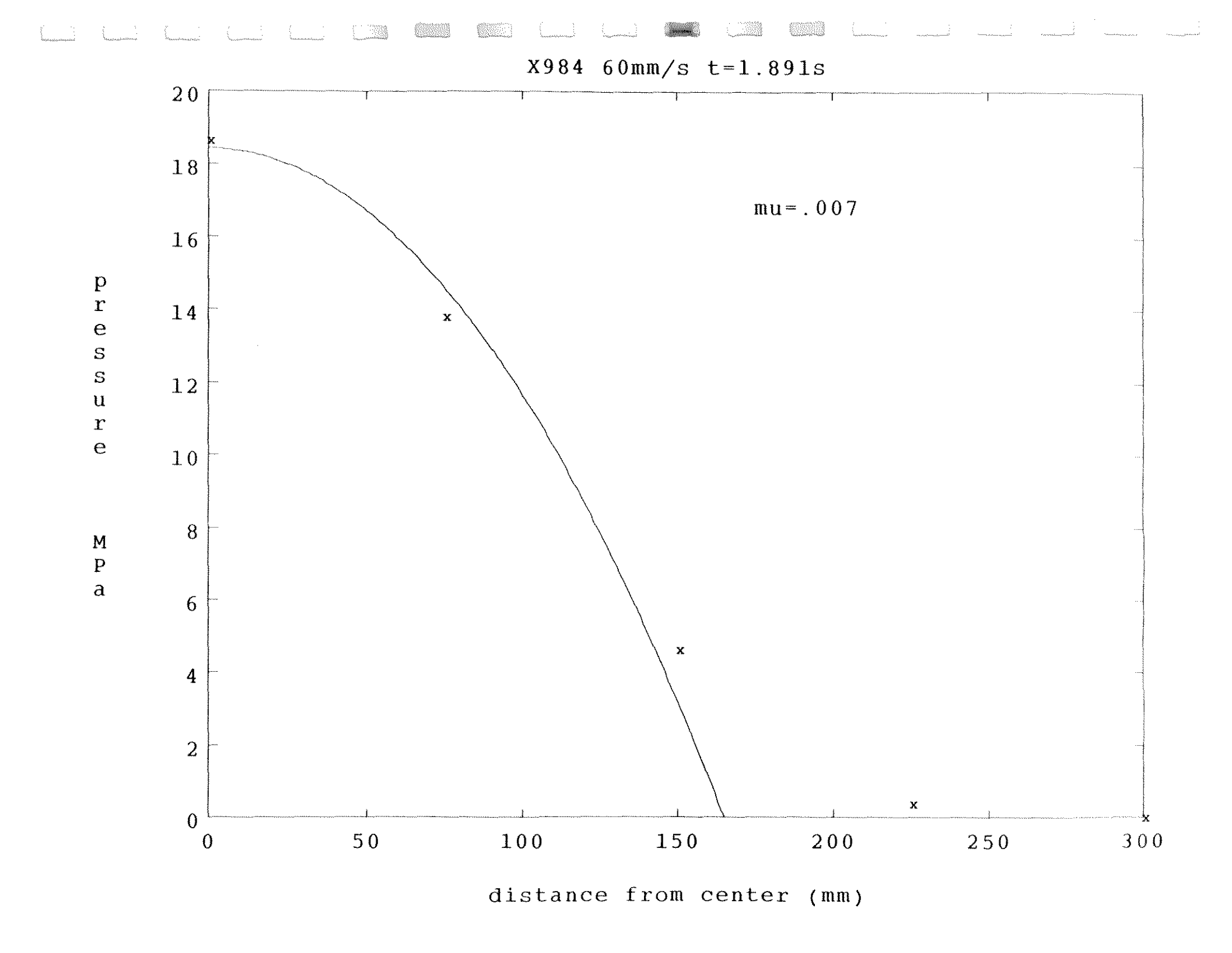
X984 60mm/s t=1.891s
mu=.007
pressure MPa
distance from center (mm)
0
2
4
6
8
10
12
14
16
18
20
0
50
100
150
200
250
300

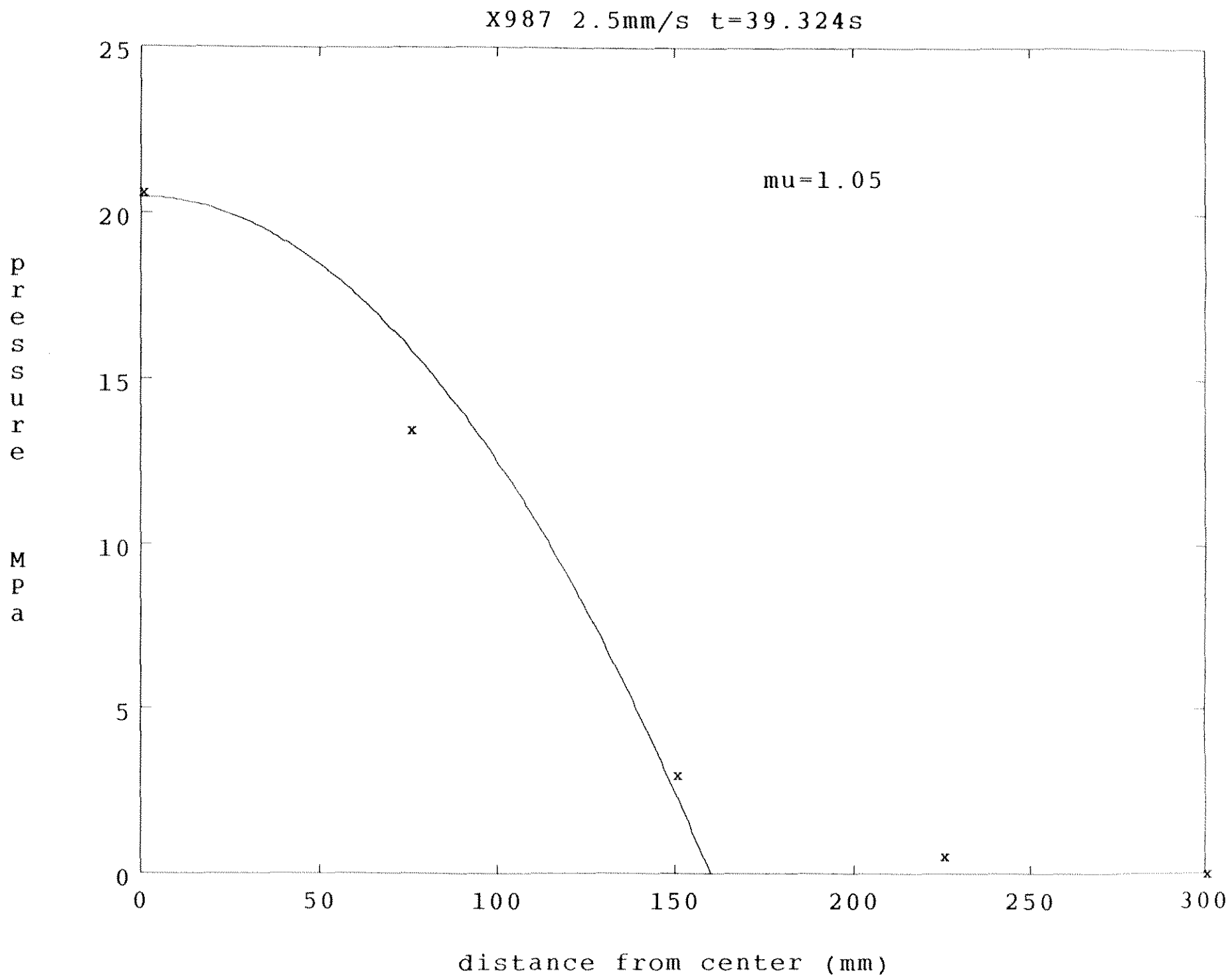
X987 2.5mm/s t=39.324s
mu=1.05
pressure MPa
distance from center (mm)
0
5
10
15
20
25
0
50
100
150
200
250
300

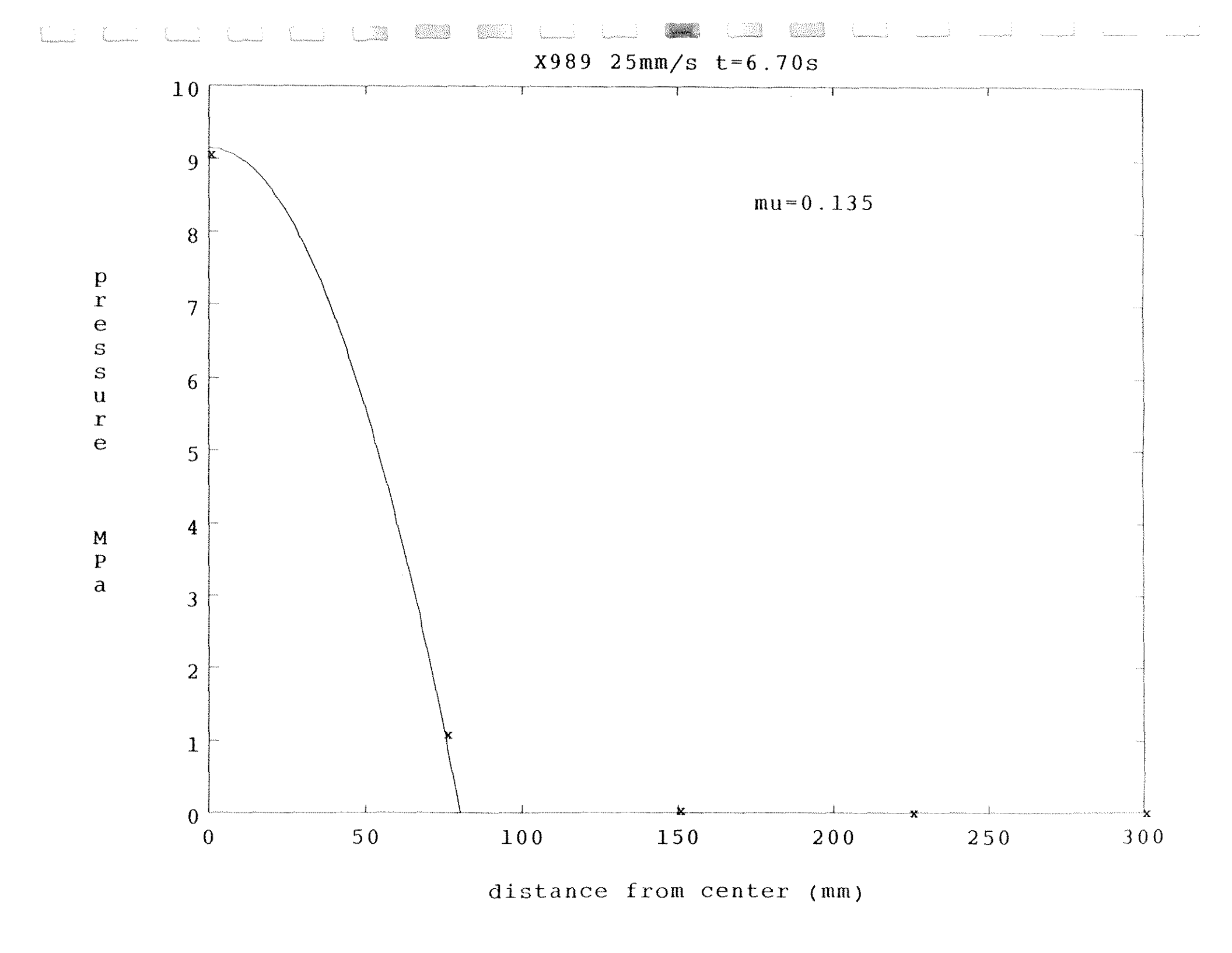
X989 25mm/s t=6.70s
mu=0.135
pressure MPa
distance from center (mm)
0
1
2
3
4
5
6
7
8
9
10
0
50
100
150
200
250
300

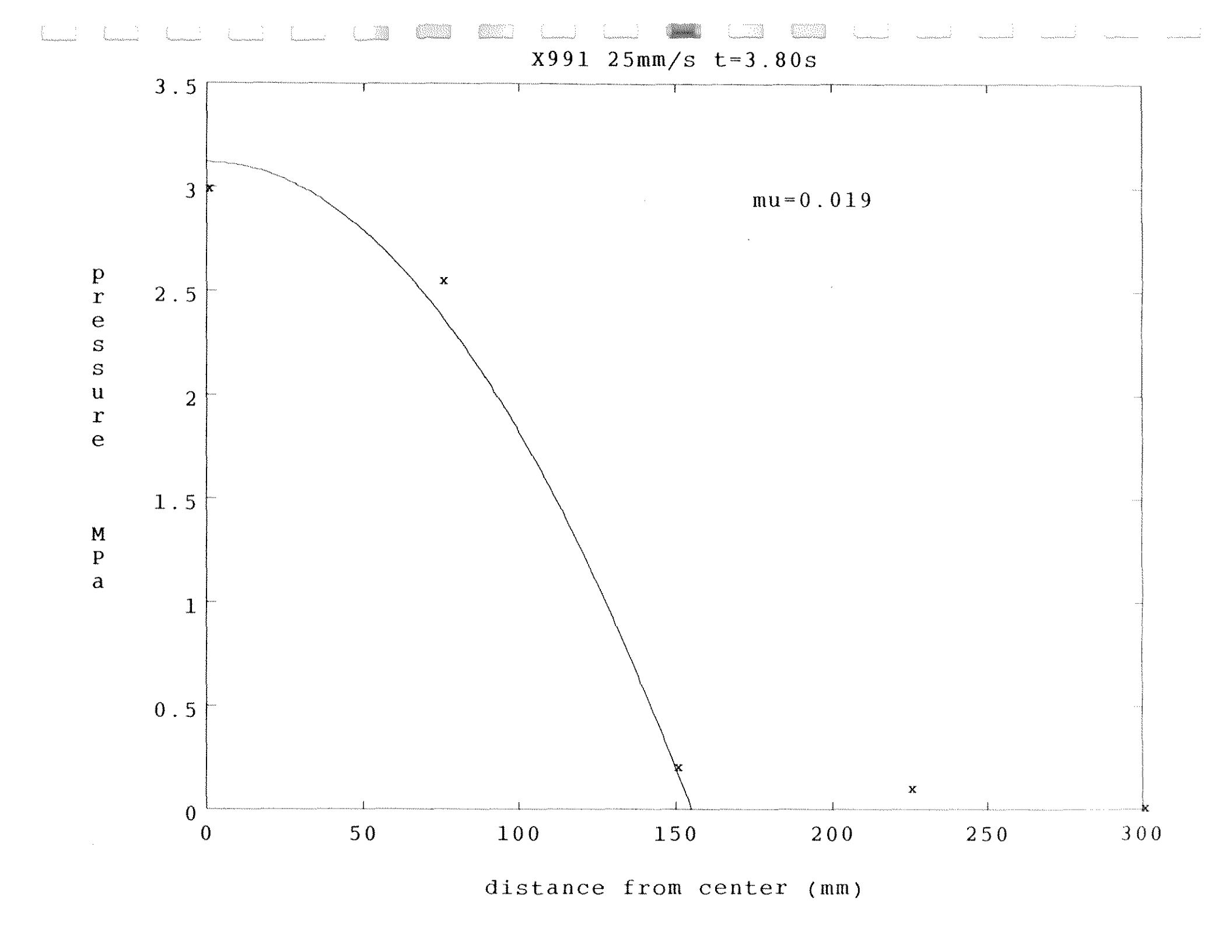
X991 25mm/s t=3.80s
mu=0.019
pressure MPa
distance from center (mm)
3.5
3
2.5
2
1.5
1
0.5
0
0
50
100
150
200
250
300

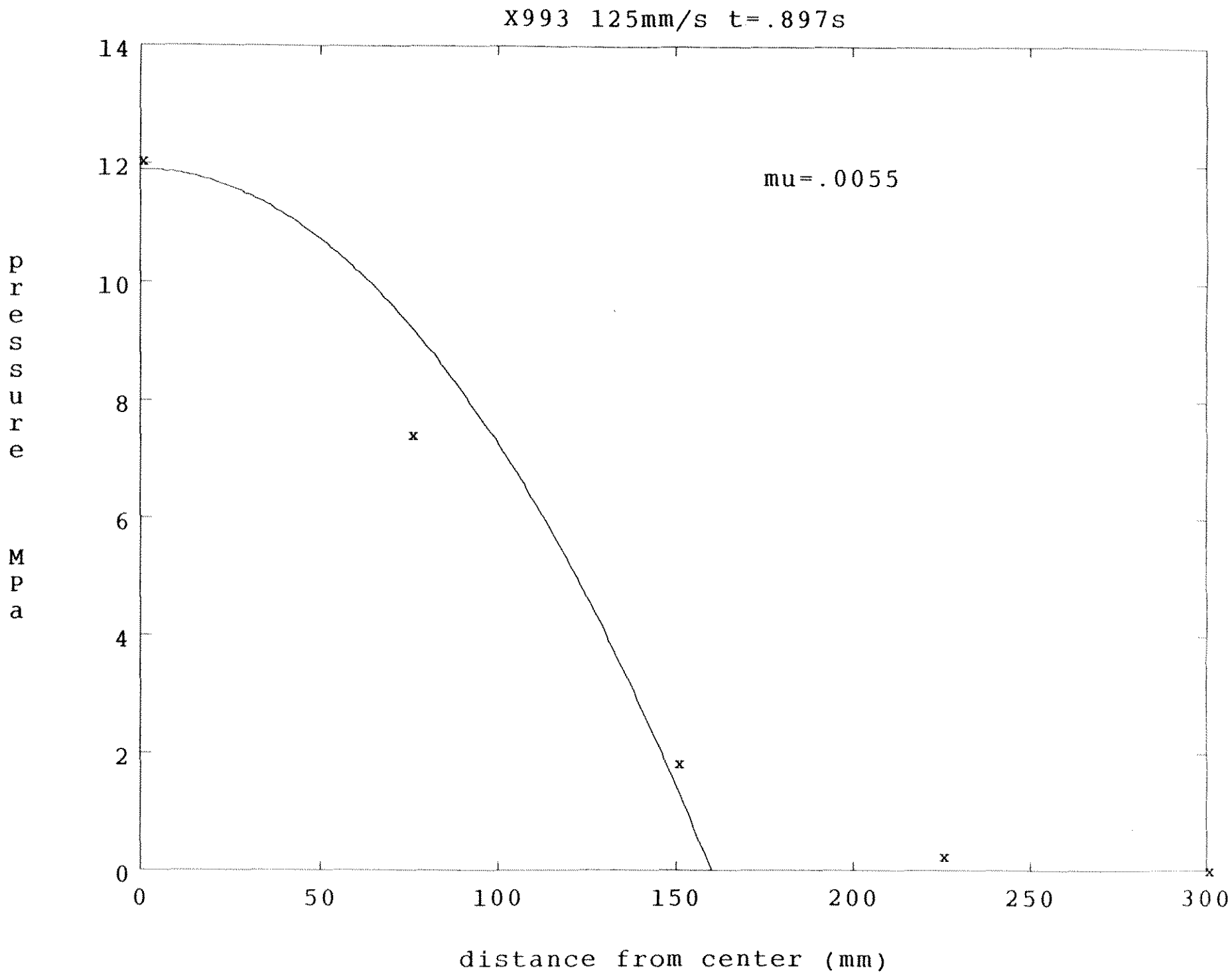
X993 125mm/s t=.897s
mu=.0055
pressure MPa
distance from center (mm)
0
2
4
6
8
10
12
14
0
50
100
150
200
250
300

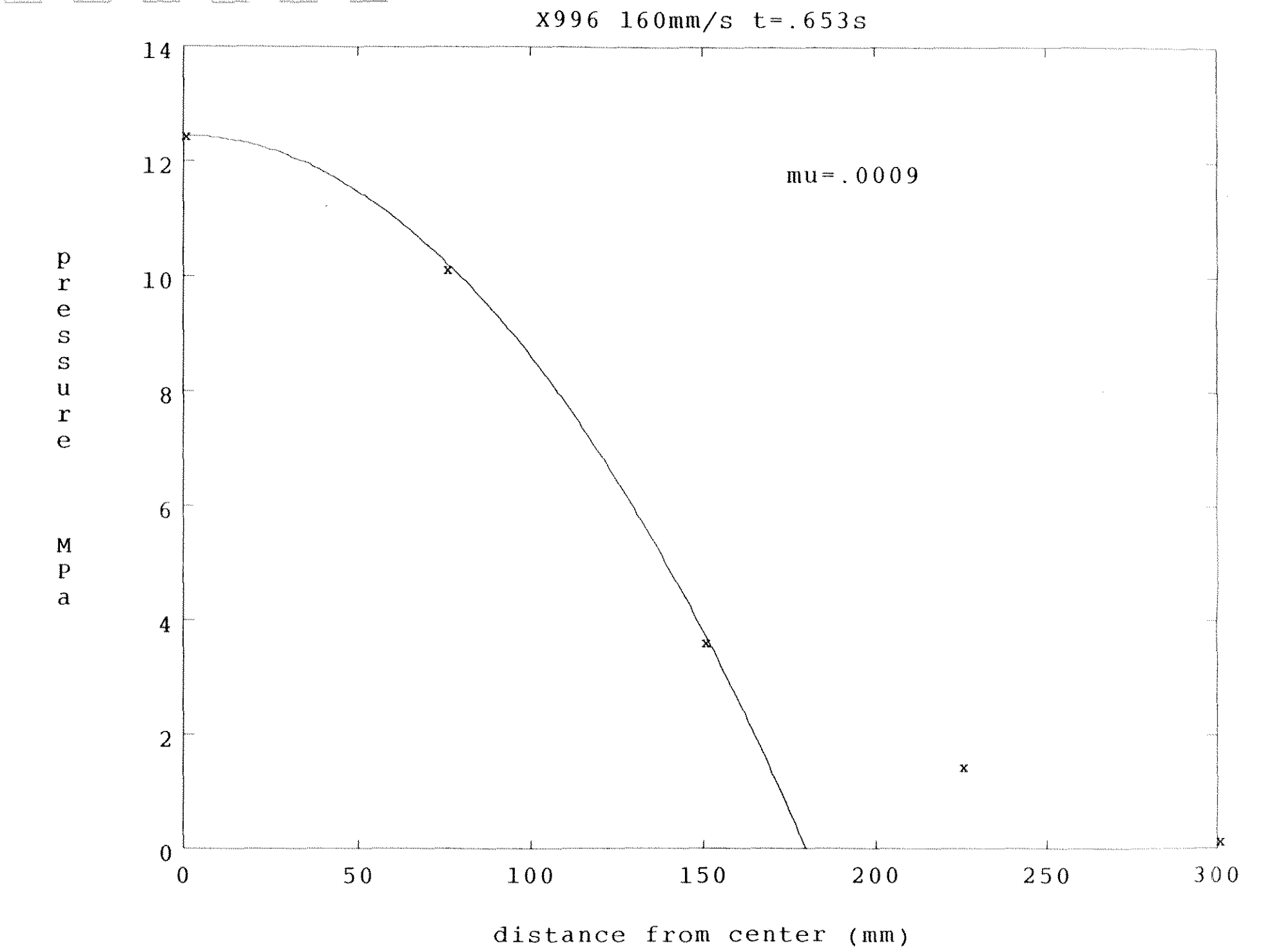
X996 160mm/s t=.653s
mu=.0009
pressure MPa
distance from center (mm)
0
2
4
6
8
10
12
14
0
50
100
150
200
250
300

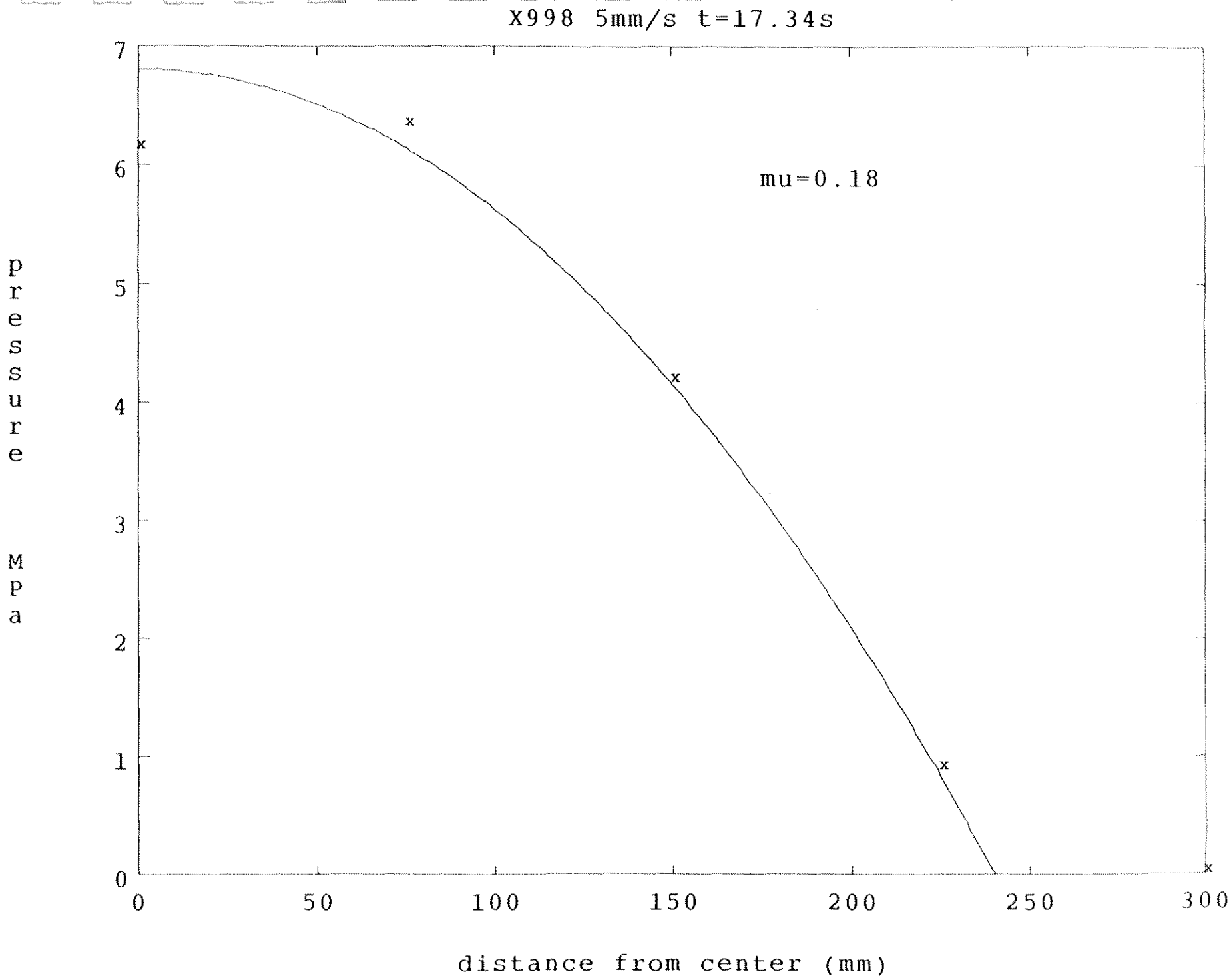
X998 5mm/s t=17.34s
mu=0.18
pressure Mpa
distance from center (mm)
0
1
2
3
4
5
6
7
0
50
100
150
200
250
300

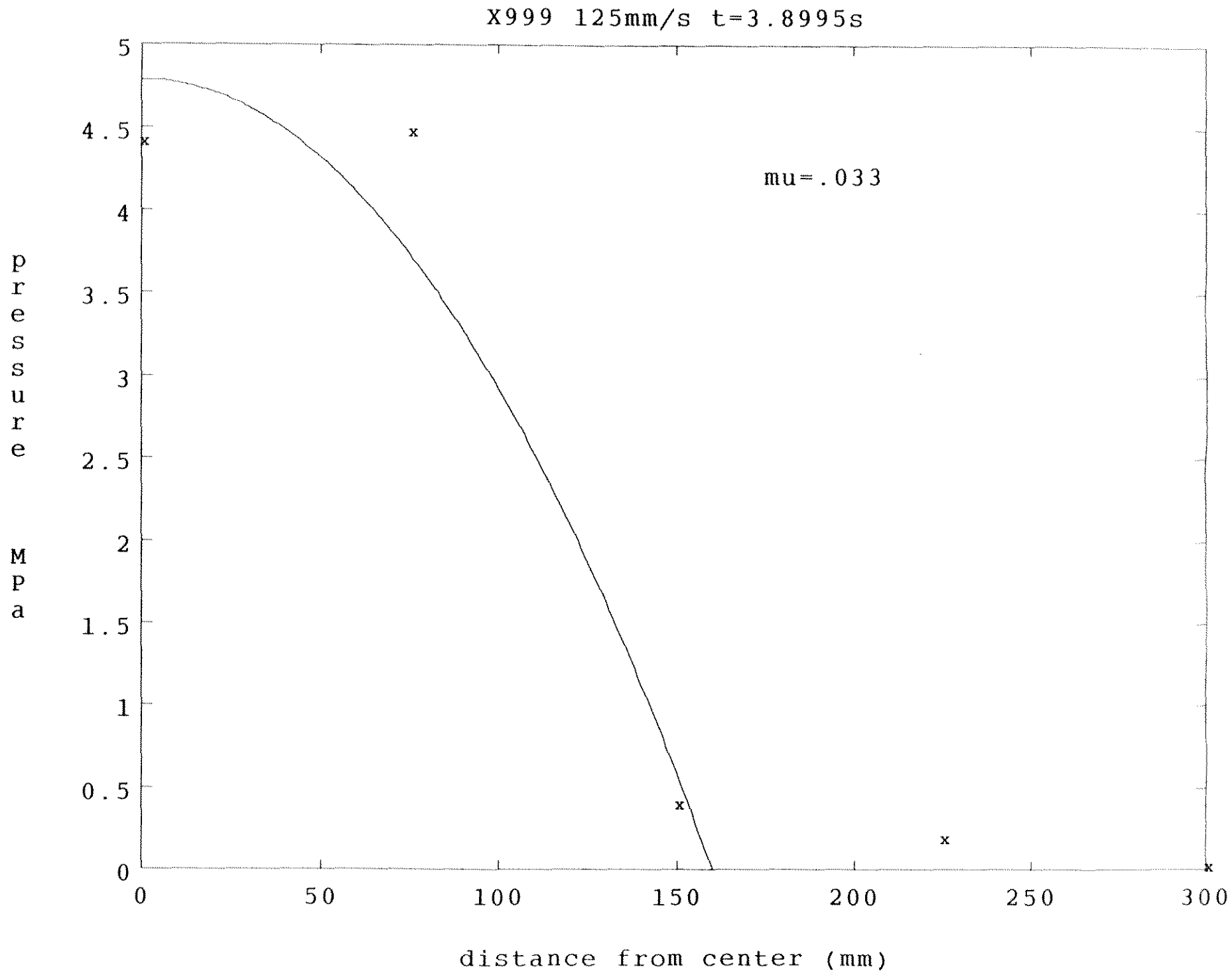
X999 125mm/s t=3.8995s
mu=.033
pressure
Mpa
distance from center (mm)
0
0.5
1
1.5
2
2.5
3
3.5
4
4.5
5
0
50
100
150
200
250
300

Appendix 3 : Bingham Fits

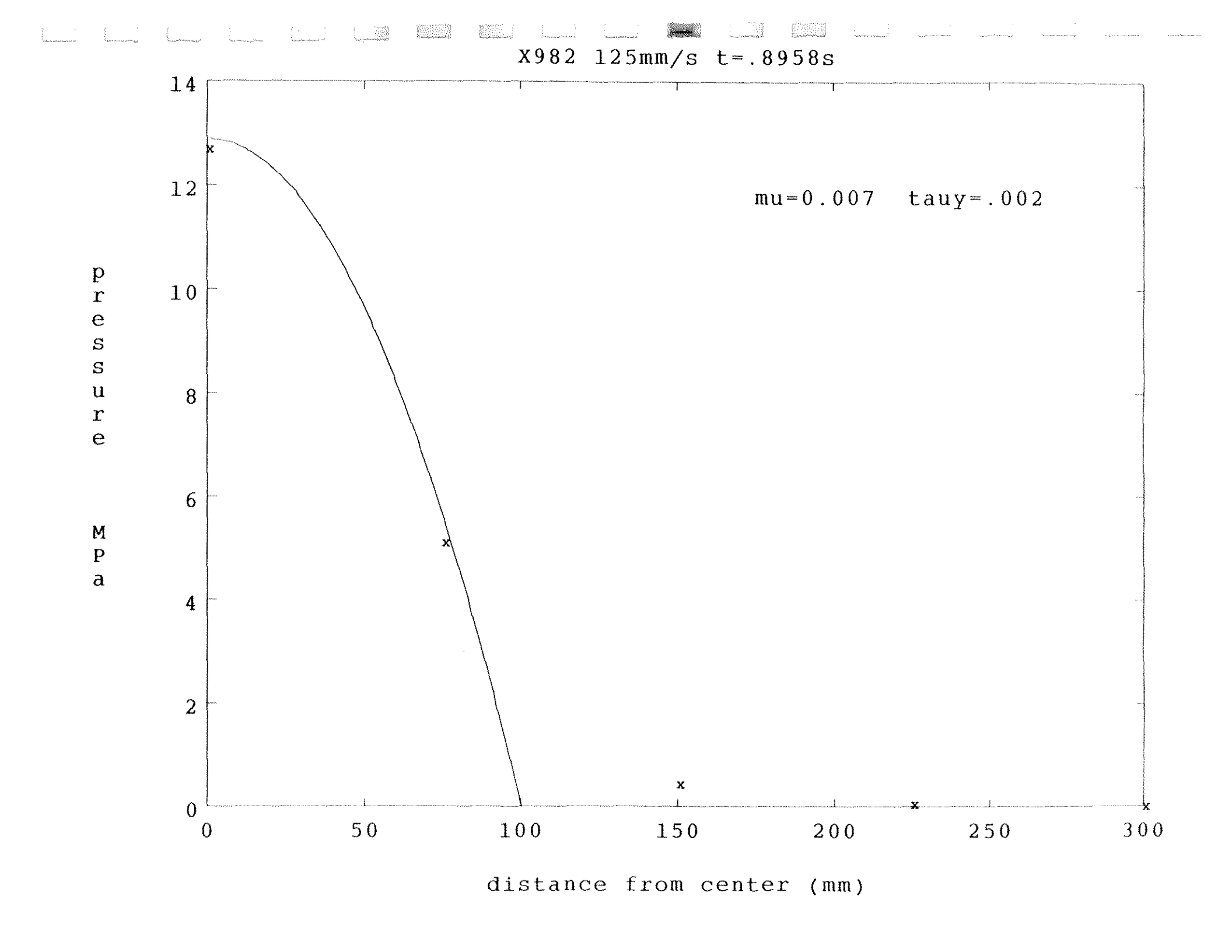
X982 125mm/s t=.8958s
mu=0.007 tauy=.002
pressure MPa
distance from center (mm)
0
2
4
6
8
10
12
14
0
50
100
150
200
250
300

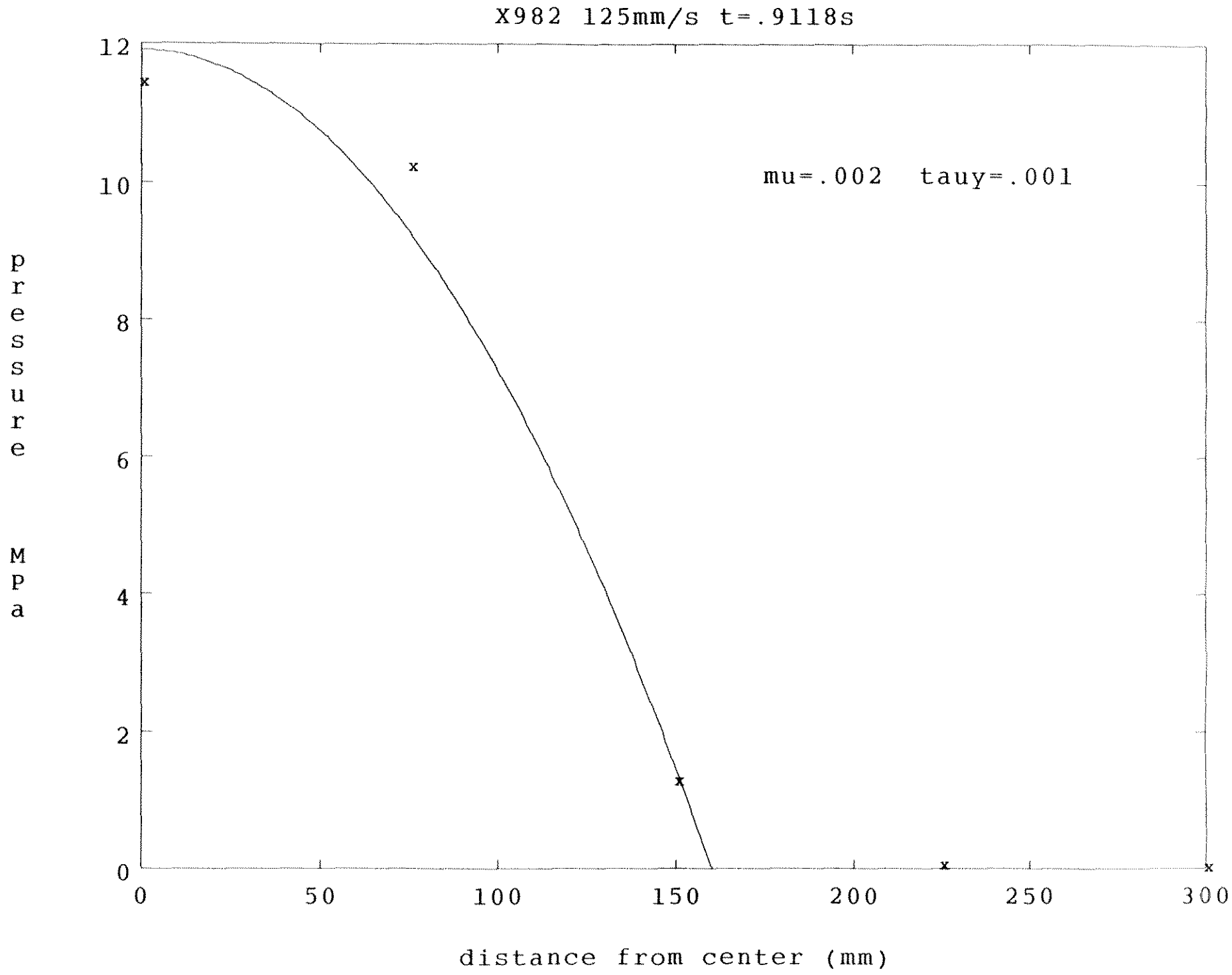
X982 125mm/s t=.9118s
mu=.002 tauy=.001
pressure MPa
distance from center (mm)
0
2
4
6
8
10
12
0
50
100
150
200
250
300

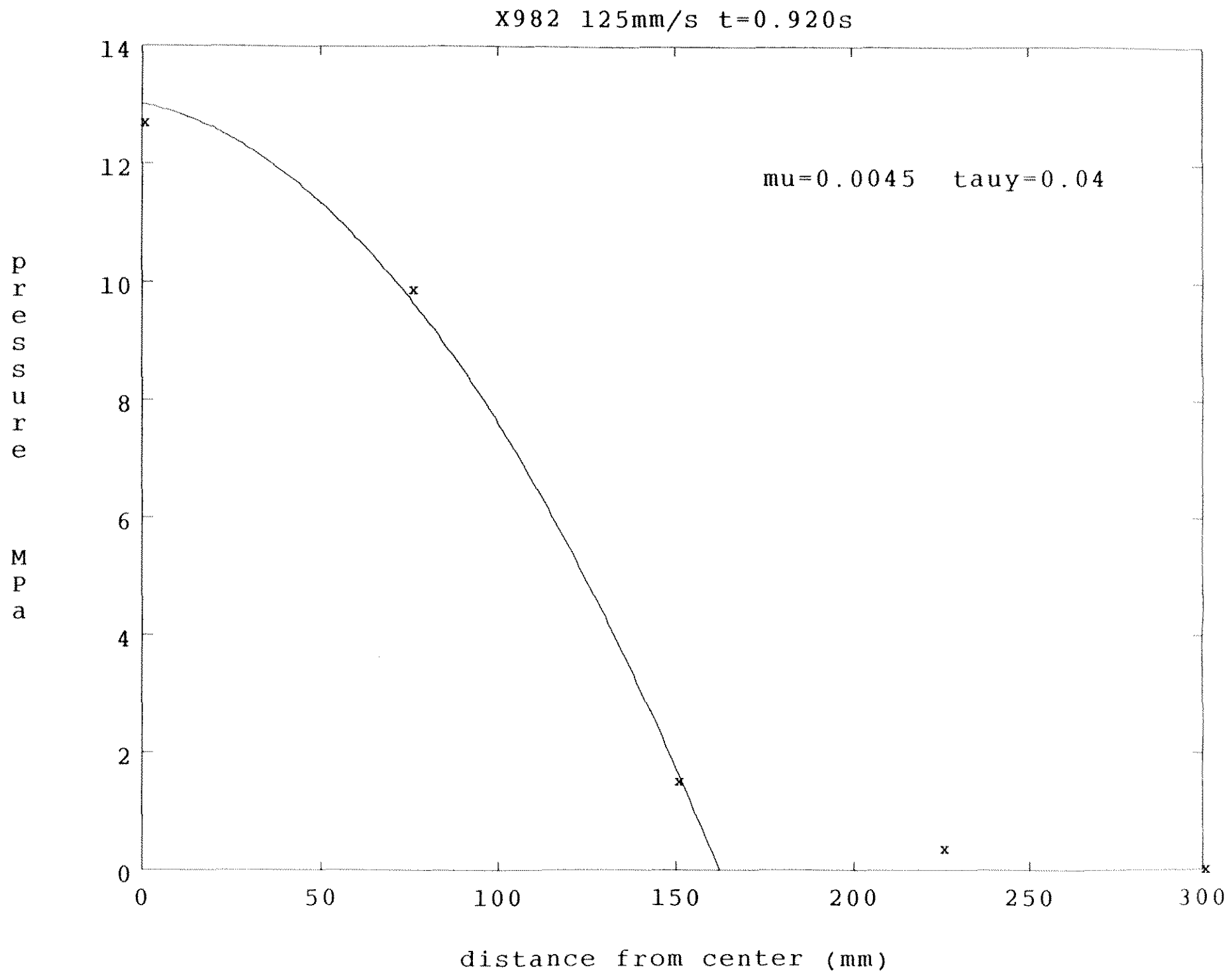
X982 125mm/s t=0.920s
mu=0.0045 tauy=0.04
pressure MPa
distance from center (mm)
0
2
4
6
8
10
12
14
0
50
100
150
200
250
300

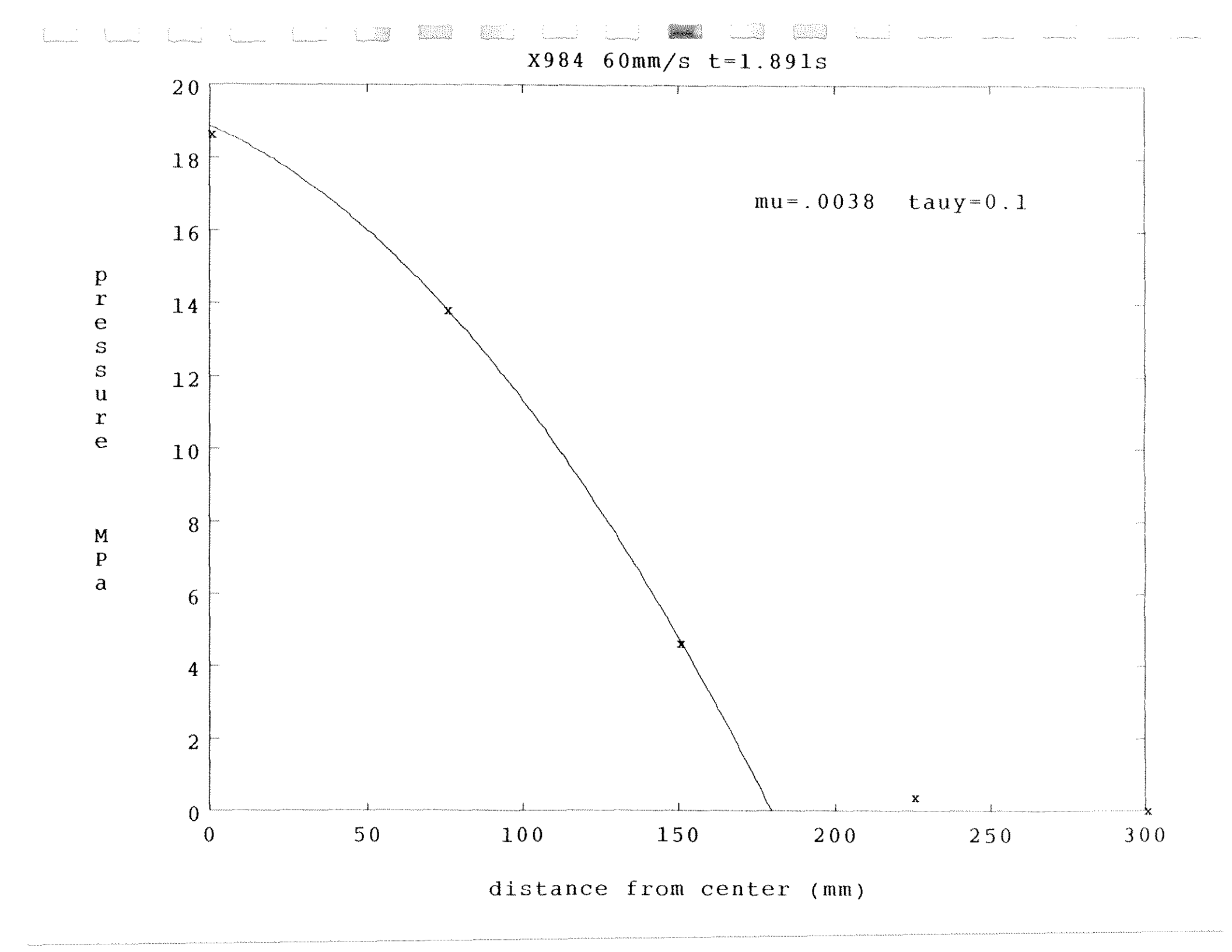
X984 60mm/s t=1.891s
mu=.0038 tauy=0.1
pressure MPa
distance from center (mm)
0
2
4
6
8
10
12
14
16
18
20
0
50
100
150
200
250
300

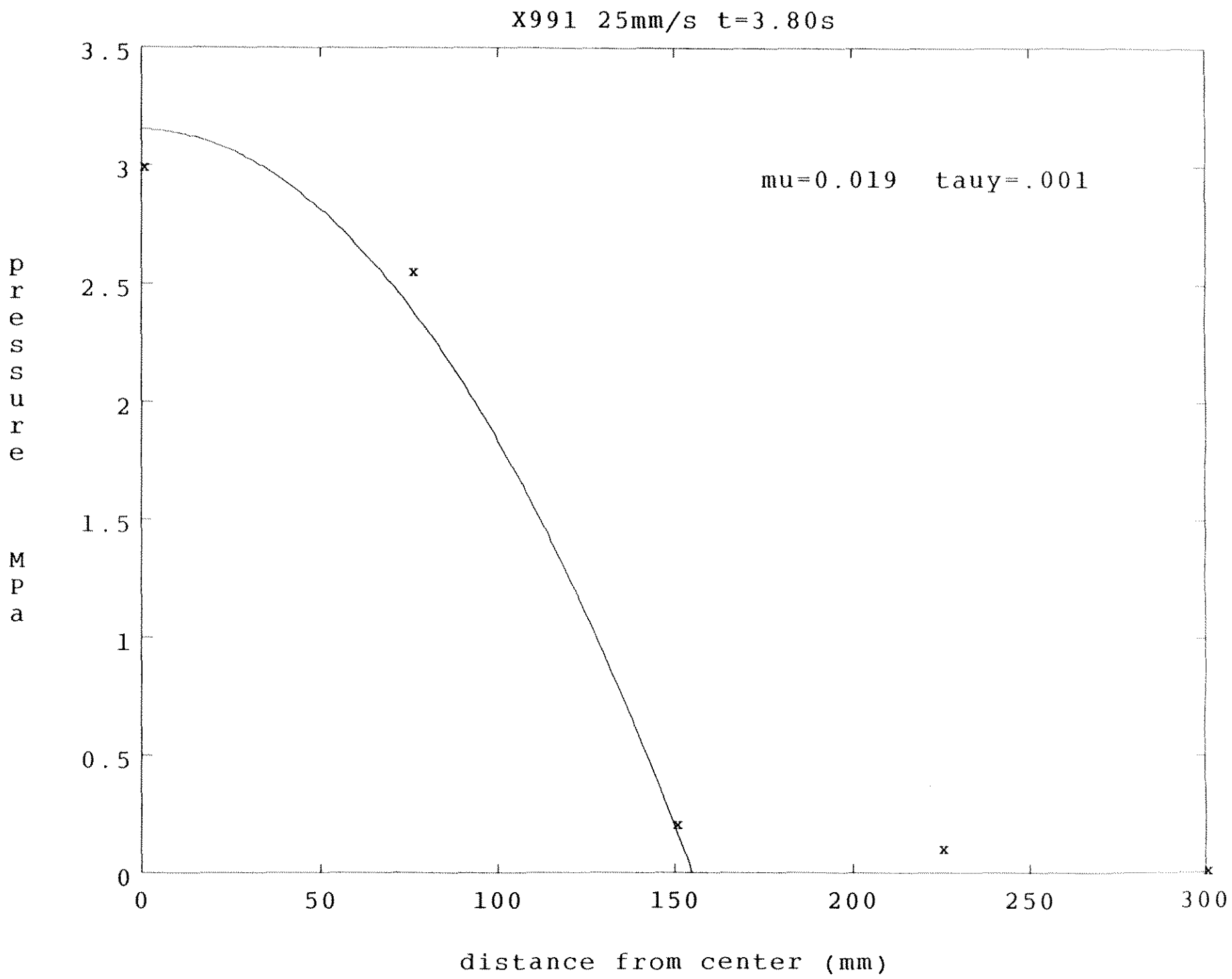
X991 25mm/s t=3.80s
mu=0.019 tauy=.001
pressure MPa
distance from center (mm)
0
0.5
1
1.5
2
2.5
3
3.5
0
50
100
150
200
250
300

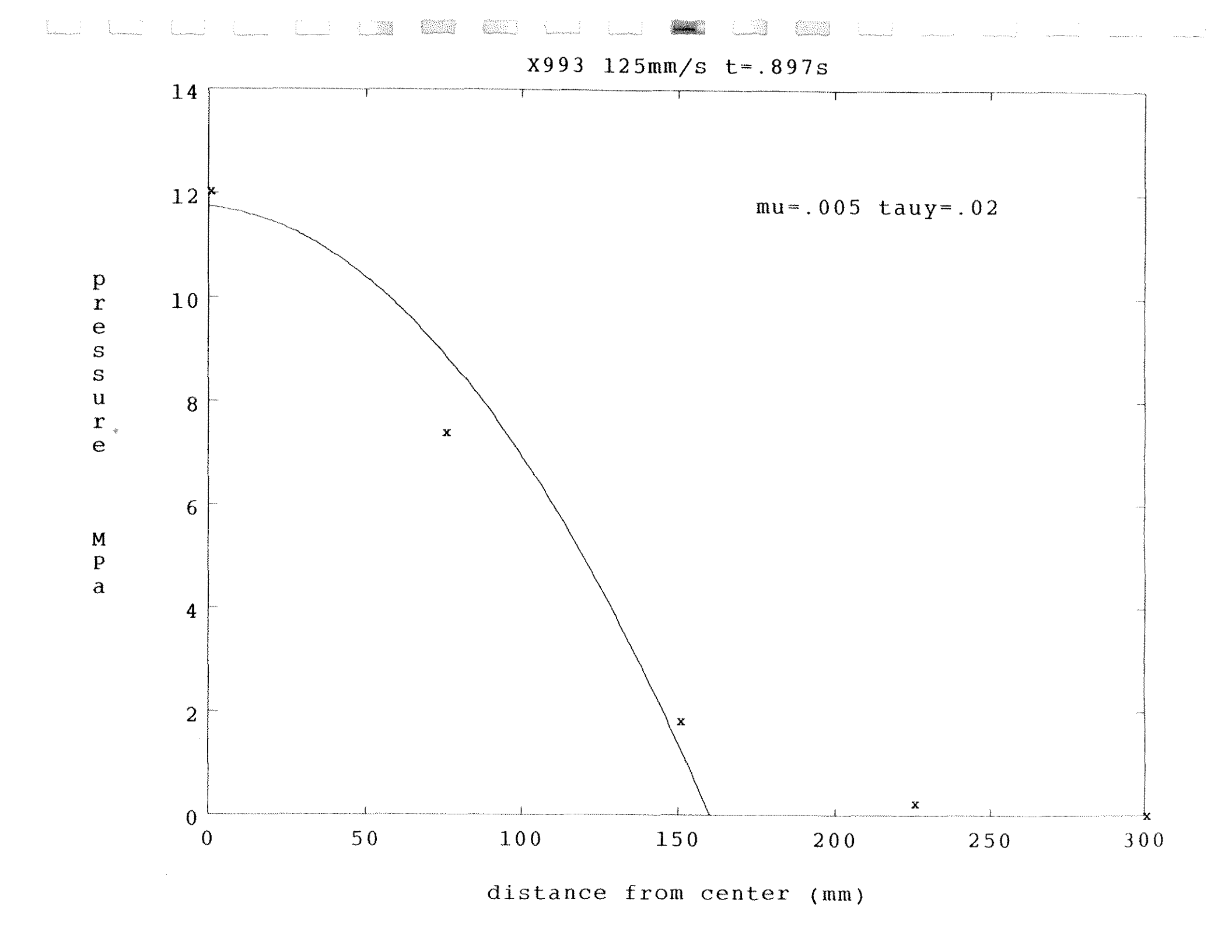
X993 125mm/s t=.897s
mu=.005 tauy=.02
pressure MPa
distance from center (mm)
0
2
4
6
8
10
12
14
0
50
100
150
200
250
300

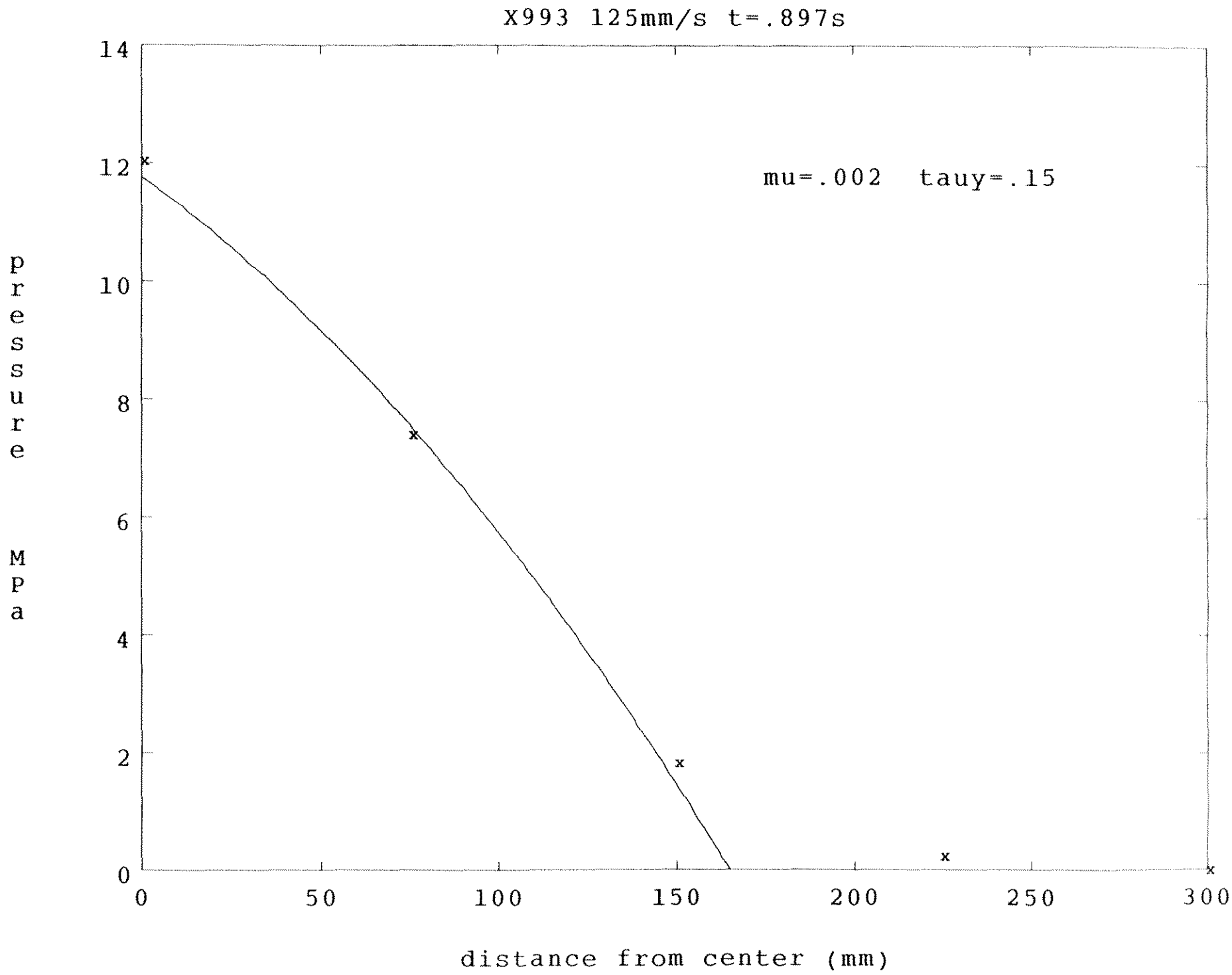
X993 125mm/s t=.897s
mu=.002 tauy=.15
pressure MPa
distance from center (mm)
0
2
4
6
8
10
12
14
0
50
100
150
200
250
300

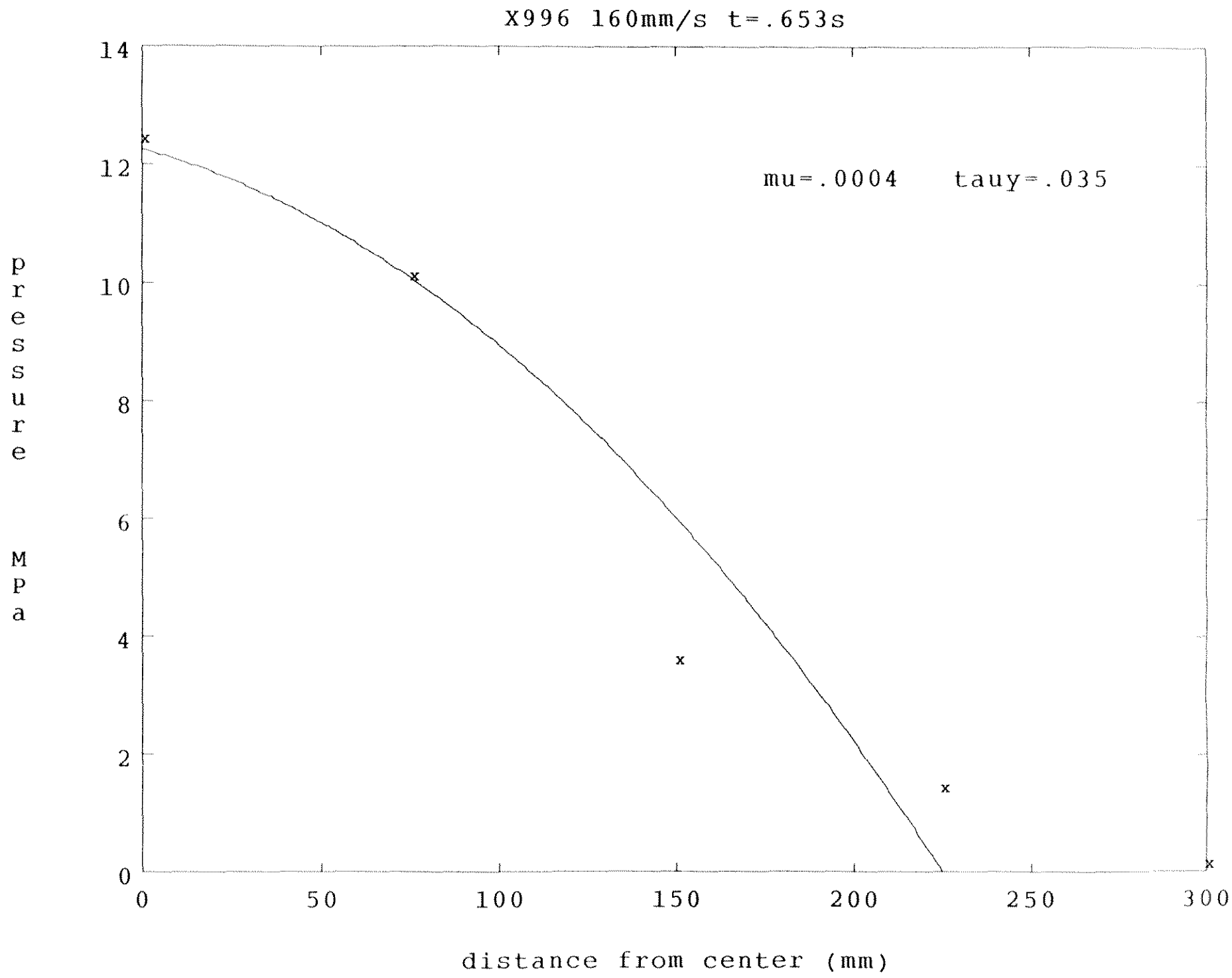
X996 160mm/s t=.653s
mu=.0004 tauy=.035
pressure MPa
distance from center (mm)
0
2
4
6
8
10
12
14
0
50
100
150
200
250
300

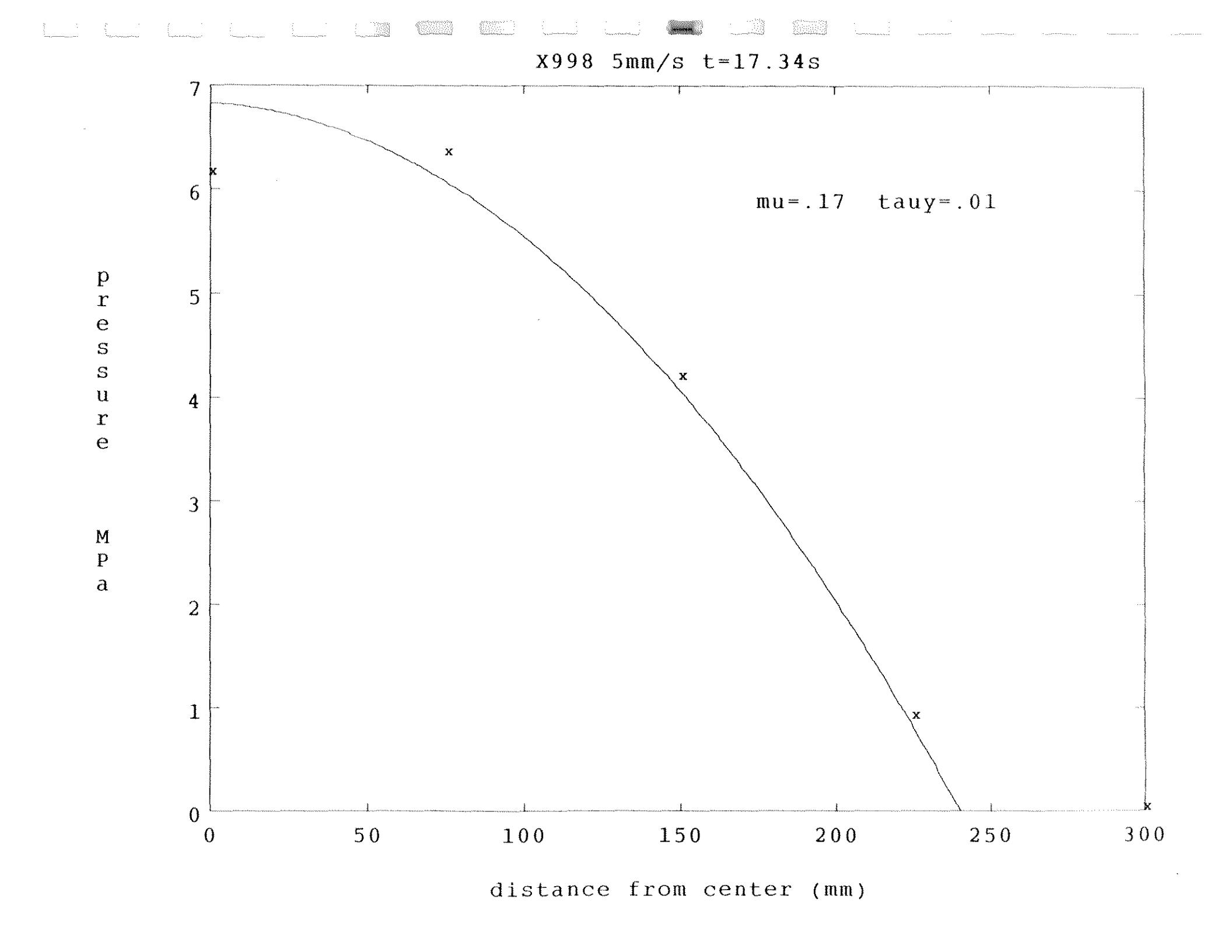
X998 5mm/s t=17.34s
mu=.17 tauy=.01
pressure MPa
distance from center (mm)
0
1
2
3
4
5
6
7
0
50
100
150
200
250
300

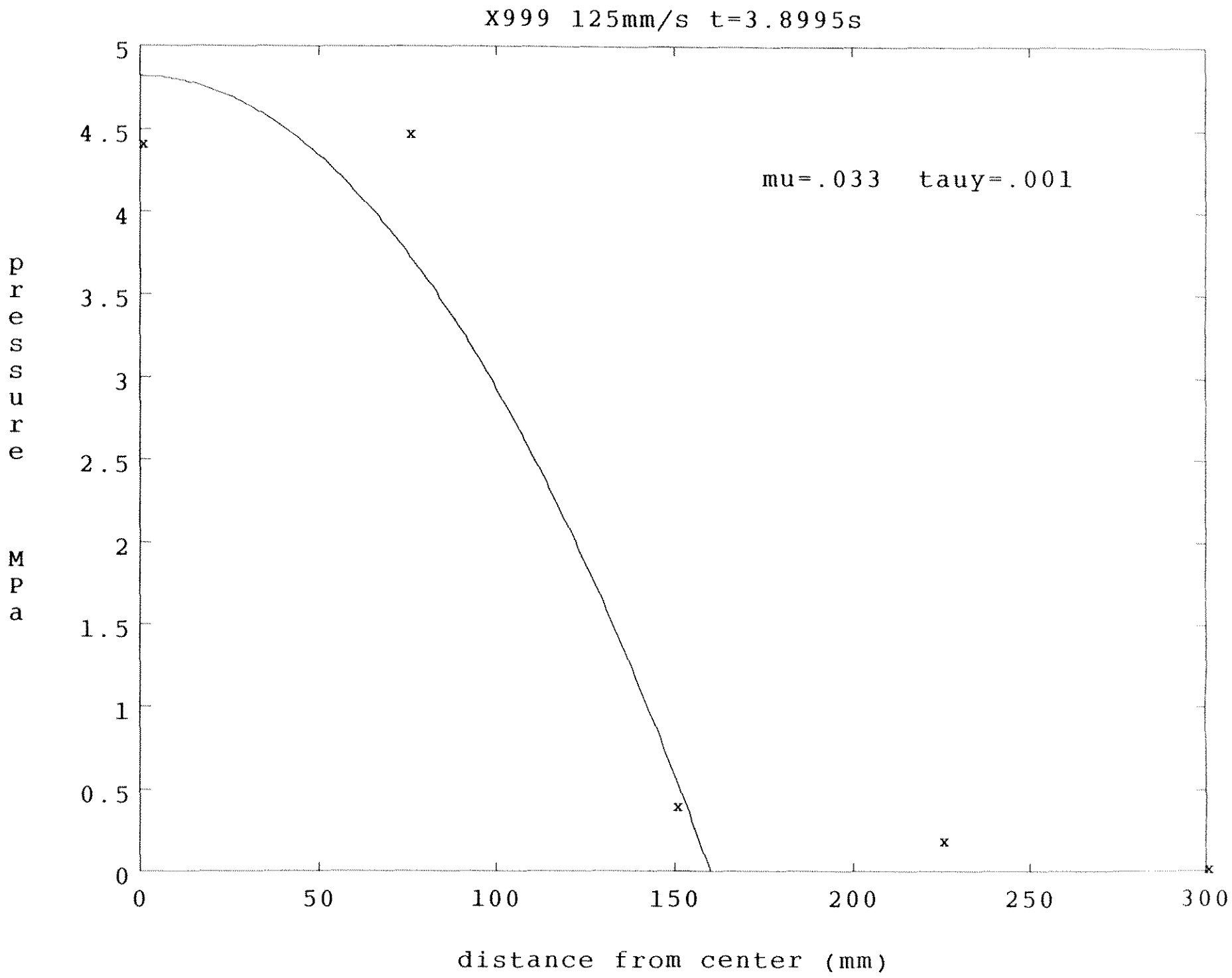
X999 125mm/s t=3.8995s
mu=.033 tauy=.001
pressure MPa
distance from center (mm)
0
0.5
1
1.5
2
2.5
3
3.5
4
4.5
5
0
50
100
150
200
250
300

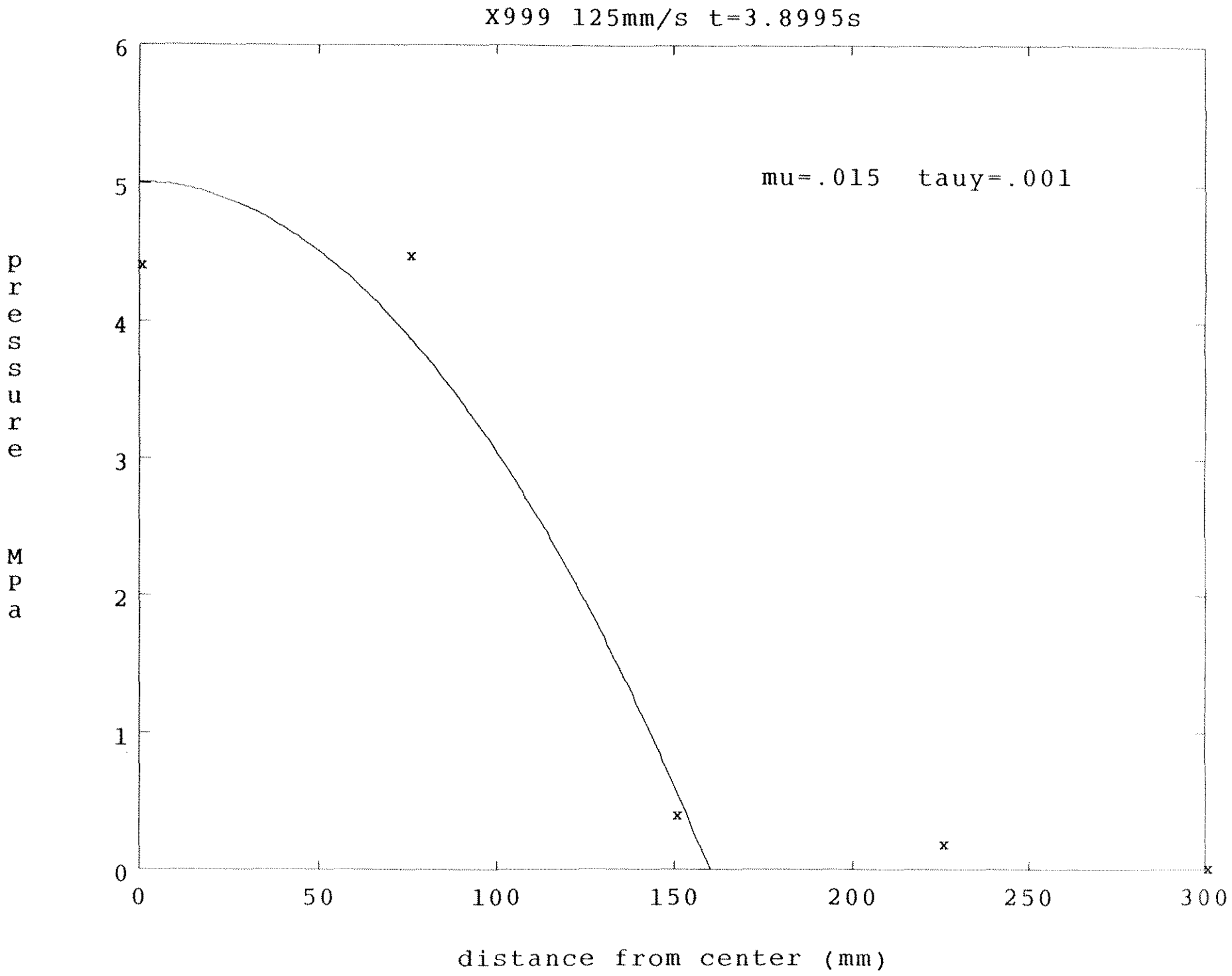
X999 125mm/s t=3.8995s
mu=.015 tauy=.001
pressure MPa
distance from center (mm)
0
1
2
3
4
5
6
0
50
100
150
200
250
300

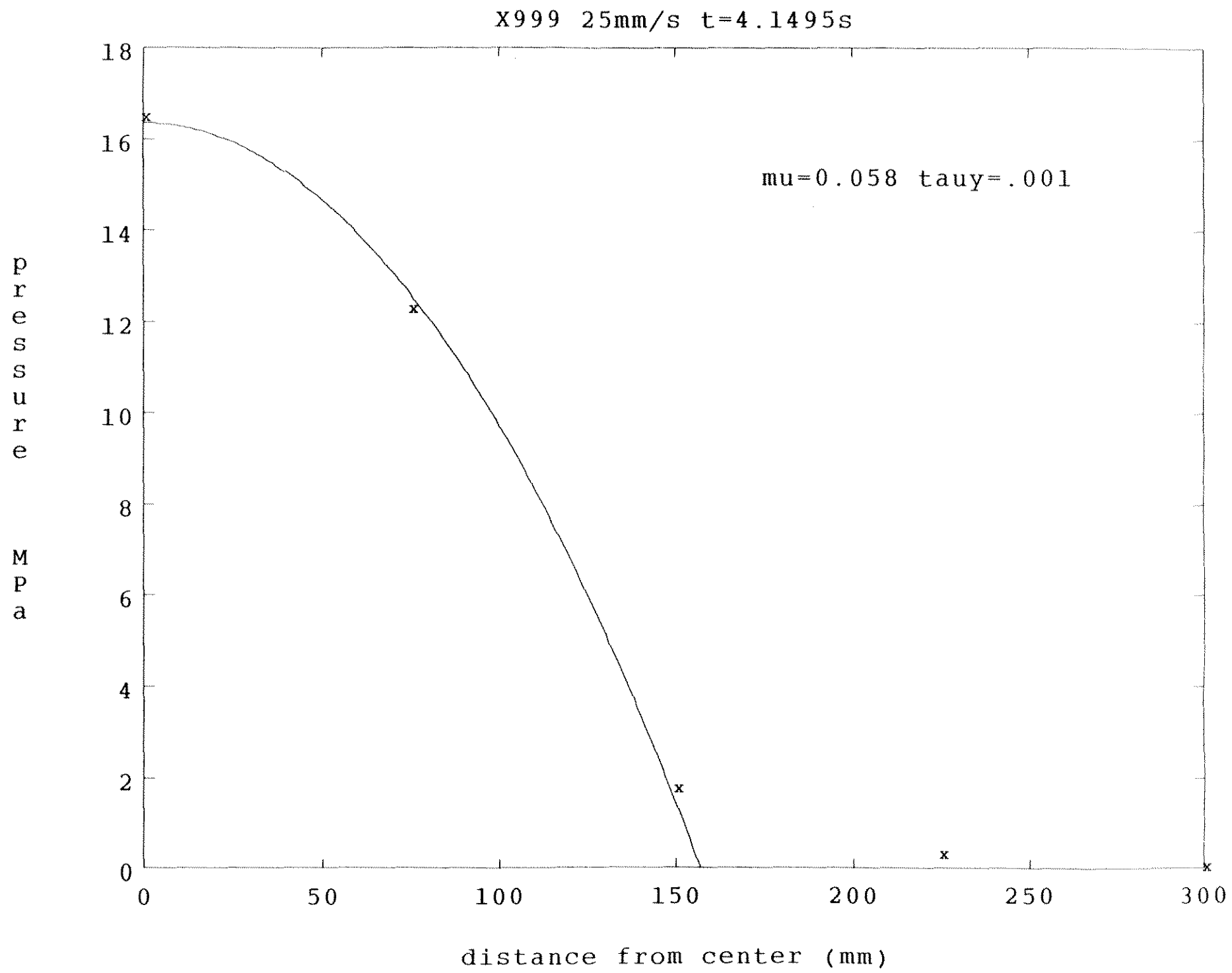
X999 25mm/s t=4.1495s
mu=0.058 tauy=.001
pressure MPa
distance from center (mm)
0
2
4
6
8
10
12
14
16
18
0
50
100
150
200
250
300